Charge Mobility in π-Conjugated Polymer Systems



Laszlo Berencei

Balliol College

University of Oxford

A thesis submitted for the degree of

Doctor of Philosophy

Michaelmas 2021

Abstract

Conjugated polymers represent a class of materials which exhibit excellent potential as versatile and cheap semiconductors in microelectronic devices. Their use in OLED displays is already wide-spread, and increasingly efficient solar cells are reported continuously. A key theoretical challenge in π-conjugated polymer systems is the incomplete understanding of charge transport mechanisms, and how competing microscopic and macroscopic effects influence it. In this thesis, charge transport and charge mobility are modelled at various length scales and varying levels of computational accuracy to better understand these processes. The models are based on phenyl-containing polymeric systems, but are generic in their implementation and would be adaptable to a range of comparable systems.

A novel atomistic model of charge mobility in bulk poly(*p*-phenylene-vinylene) (PPV) is presented. The incorporated structural and energetic disorder results in Anderson localised and quasi-extended donor and acceptor states. Charge migration through the system is facilitated by a kinetic Monte Carlo algorithm, aided by transition rates of separate inter- and intra-chain events defined within the framework of Marcus theory. The effects of disorder, temperature, field strength bias are studied. The $\log \mu \propto \sqrt{F}$ field dependence of mobility, which has already been widely reported in literature, naturally emerges at high electric field values. Crucially, the relative importance of inter-chain and intra-chain is highlighted by this model – at low fields, charge transport occurs almost entirely intermolecularly, between highly localised states, while at high fields, intramolecular transitions with the aid of quasi-extended states become most important.

The nature of intramolecular charge dynamics is further examined using a mixed quantum-classical model of charge-polaron transport. The dynamics of the charge follows the time-dependent Schrödinger equation, while the rotational motion of monomers is modelled via the Langevin equation, encapsulating the effect of Brownian fluctuations in rotational displacements. The two are coupled using the Ehrenfest equations of motion. The emergence of two distinct temperature regimes are observed. At the lowest temperatures, the polaron 'crawls' along the polymer chain stochastically, while remaining fully localised and in the lowest quasidiabatic state. As the temperature increases, an activated, Landau-Zener type of dynamics is observed, leading to hopping transport between diabatic states. This additional pathway provides a link to the bulk charge transport mechanism.

Statement of Originality

I confirm that this thesis and the work presented are of my own efforts. All ideas, data, figures, and works of others (whether published or unpublished) are fully identified as such within the thesis. This thesis has not been submitted in whole or in part for another academic degree at this or any other university.

Laszlo Berencei
February 2022

Acknowledgements

As my DPhil journey is drawing to a conclusion, I would like to take the time to reflect on my time in Oxford, and the people who helped me get to this point. First and foremost, I would like to thank my supervisor, William Barford, for his guidance, encouragement, and patience. From the moment he agreed to take me on as a student, through an irregular journey that none of could have quite expected at the beginning, I feel fortunate and honoured to have had such a brilliant and caring mentor to guide me through the process.

I am also grateful for the financial support I received from the EPRSC Centre for Doctoral Training, Theory and Modelling in Chemical Sciences, as well as from Balliol College – without them, I would not have been able to undertake this work.

I am also indebted to the members of the Theory Wing. I'd like to thank Isabel, Darren, David, Tim, Matt, Tom, John, Allison, and all the others I've met over the years, for all the fun and laughs, whether at tea and in the pub, or more recently, mostly online and over lengthy walks around Oxford. I cannot conclude this section without a mention of Jonathan Milward, whose kindness and friendship will always be remembered and sorely missed.

While I spent a lot of my time in the department, of equal significance are the friendships I've made at Balliol. Whether being on the river at ungodly hours, or enjoying a dinner (boat club or otherwise) in college, a cycle around Oxfordshire, or anywhere in-between, I am beyond grateful to have met these people, including Jonny, Will, Ed, Ben, Johan, Charlotte, Leah, and many others. A special thanks goes to Adam for being the best co-warden anyone could have wished for, even though neither of us signed up to the idea of supervising a global pandemic. As most of them now moved on from Oxford, I can only hope that these friendships will stand up to the challenge of distance and time.

Of course, there are the people I knew long before I came to Oxford, and to whom I will be close for long after I'm done here. My dearest friends from back home, Peti, Lilla, Lőrinc and all the others, your support has been instrumental to keeping me going. Your understanding and the ease at which we pick up conversation even after lengthy breaks show the strength of the friendships we've built.

To my family, I cannot put into words how much I owe to you. I know that it was a great sacrifice for you to see me move across the continent as soon as I reached adulthood, and yet you never once stopped supporting me chasing my dreams. I'm grateful for everything you've ever taught me, and for making me into the person I am today. Even as we were further isolated from each other by

the pandemic, your constant encouragement gave me strength when I needed it most. At the same time, I would like to issue a small apology to you specifically, Zsolti. Moving abroad when you were so young meant that I haven't been as present in your childhood as I should have been. This doesn't stop me being proud of the brilliant young man you're growing up to be, and I hope that we can find a way to live closer to each other in the future.

And finally, but most importantly, Rachel, my gratitude to you is endless. Throughout the entirety of the pandemic, you have been my single biggest supporter and my ever present company. From the lockdown walks in the early days, through the Oxford holiday staycations, to finally moving into our first place together, I am proud of the relationship that we have built every single day. You encouraged me daily when the thesis writing was at its bleakest points, and your patience has been extraordinary. I cannot wait for all the adventures we have to look forward to!

Publications

The work presented in this thesis has led to the following publications:

Chapter 4:

- L. Berencei, A. Grout-Smith, J. E. Poole, W. Barford, "Realistic model of charge mobility in π-conjugated polymer systems", *J. Chem. Phys.* **2019**, *151*, 64120

Chapter 5:

- L. Berencei, W. Barford, S. R. Clark, "Thermally driven polaron transport in conjugated polymers", *Phys. Rev. B* **2022**, *105*, 14303

Contents

List of Abbreviations **ix**

1 Introduction **1**

1.1 Conjugated Polymers 2

1.2 Applications 4

1.2.1 OLED Devices 4

1.2.2 Photovoltaic Devices 5

1.3 Charge Transfer 7

1.3.1 Experimental Background 8

1.3.2 Computational and Theoretical Overview 11

1.4 Thesis Structure 16

2 Theoretical Background **18**

2.1 Quasi-1D Quantum Systems 19

2.1.1 Hückel Model 19

2.1.2 Coarse-grained Systems 20

2.1.3 Holstein Hamiltonian 21

2.1.4 Disorder and Localised States 24

2.2 Theory of Charge Transfer 28

2.2.1 Landau-Zener Theory 28

2.2.2 Marcus Theory 33

2.3 Ehrenfest Dynamics 38

2.4 Langevin Dynamics 42

3 Computational Methods **46**

3.1 Kinetic Monte Carlo 47

3.2 Matrix Product States and Time-Evolving Block Decimation 48

3.2.1 Matrix Product States 48

3.2.2 Time-Evolving Block Decimation 52

3.2.3 Periodic Boundary Conditions 54

3.3 Langevin Algorithm 57

4 Realistic Model of Bulk Charge Mobility **59**
4.1 Model Hamiltonian 60
4.2 Donor and Acceptor States 60
4.2.1 Role of Polaronic Effects 60
4.2.2 Role of Disorder 61
4.3 Marcus Theory of Transition Rates 61
4.3.1 Bimolecular (inter-chain) transfer 62
4.3.2 Unimolecular (intra-chain) Transfer 64
4.4 Realistic Polymer Conformations 65
4.5 Kinetic Monte Carlo 66
4.6 Mobility with LGS-only Hopping 69
4.6.1 Electric Field Dependence 69
4.6.2 Temperature Dependence 75
4.7 Exploring the Role of QES States 80
4.8 Comparison to MD Polymer Conformations 84
4.9 Summary 85

5 Charge Dynamics Induced by Torsional Fluctuations **91**
5.1 Introduction 91
5.1.1 Model Hamiltonian 93
5.1.2 Landau Polarons 94
5.1.3 Ehrenfest and Langevin Dynamics 96
5.1.4 Relaxation 97
5.1.5 Simulation Parameters 99
5.1.6 Boundary Effects 101
5.2 Polaron Dynamics Results 102
5.2.1 Low Temperature Polaronic Crawling 102
5.2.2 Intermediate Temperature Polaronic Hopping 109
5.2.3 Corrections from Quantised Rotons 117
5.3 Discussion and Conclusions 121

6 Conclusions and Future Work **126**

Appendices

A Quantised Rotons in TEBD-Ehrenfest Scheme **132**

B Benchmarking Periodic Boundary Conditions in TNT **136**

References **145**

List of Abbreviations

1D . . . . . One-dimensional

PPV . . . . . Poly(*p*-phenylene-vinylene)

MEH-PPV . . Poly(2-methoxy-5-(2'-ethylhexyloxy)-*p*-phenylene vinylene)

PPP . . . . . Poly(*p*-phenylene)

P3HT . . . . . Poly(3-hexylthiophene-2,5-diyl)

TNT . . . . . Tensor network theory

MPS . . . . . Matrix product state

TEBD . . . . . Time-evolving block decimation

OBC . . . . . Open boundary conditions

PBC . . . . . Periodic boundary conditions

SVD . . . . . Singular value decomposition

LGS . . . . . Localised ground state

QES . . . . . Quasi-extended state

kMC . . . . . Kinetic Monte Carlo

LUMO . . . . Lowest unoccupied molecular orbitals

HOMO . . . . Highest occupied molecular orbitals

SVP . . . . . Signed-value parameter

DOS . . . . . Density of states

FWHM . . . . Full width at half maximum

MD . . . . . Molecular dynamics

GDM . . . . . Gaussian disorder model

FGR . . . . . Fermi Golden Rule

TDSE . . . . . Time-dependent Schrödinger equation

1 Introduction

Organic materials with semiconducting capabilities have a long history, dating back to the mid-19$^{\text{th}}$ century when polyanaline was first synthesised.[3] The group of materials which are the subject of this thesis, conjugated polymers, started gathering particular interest from the research community after multiple breakthrough results in the 1970s.[4] Following the first reports of the successful synthesis of polyacetylene thin-films,[5] derivative compounds exhibiting conductive capabilities were soon reported,[6–9] sparking research interest. The discovery[10] of light-emitting polymers in 1990 added a further practical and direct application to these materials in the form of displays in microelectronic devices. Their use as alternatives to silicon based semiconductors in photovoltaic devices has also been actively researched for decades.[11] The relevance and potential of the field of conductive polymer systems has been highlighted by the recognition of pioneers Heeger, MacDiarmid and Shirakawa with the 2000 Nobel Prize for chemistry.[12–14]

In the following, an introduction to the general features governing conjugated polymer systems will be presented, as well as an overview of how this thesis aims to answer some of the questions about the mechanism and limitations of charge transport in these systems.

1.1 Conjugated Polymers

π-conjugated polymers are defined by their shared chemical structure: the backbone of the polymer chain is made up of an unbroken sequence of sp or sp^2 hybridised carbon atoms, which means that each of these atoms contribute a p-orbital to an π-orbital that spans the length of polymer chain. This extended electronic structure gives rise to the special properties of conjugated polymers. The chemical structures of a few notable example systems are shown in Fig. 1.1. These polymers are characterised by a number of special features that set them apart from their inorganic counterparts. The covalently bonded molecular chains result in long-ranging, strong interactions within each molecule. The intermolecular van der Waals forces are significantly weaker, and therefore quantum mechanical coherence rarely extends beyond a single chain. The combined effect of this, along with the length and therefore system size of polymers, leads to these systems following quasi-one-dimensional physics of extended systems,[4] including excited states being described in terms of quasi-particles, such as polarons. Finally, polymer systems are characterised by widespread disorder, both in terms of structural defects and environmental effects (e.g., electrostatic fluctuations in solvent environment). As described in more detail in later chapters, this necessarily leads to localisation of the electronic wavefunction in quasi-1D systems (which takes place along a single polymer chain), which has significant consequences for the nature of charge transport. Finally, this electronic structure leads to most π-conjugated polymers having band gaps in the visible light region of the electromagnetic spectrum, which allows applications both as light-emitting devices and as organic solar cells.

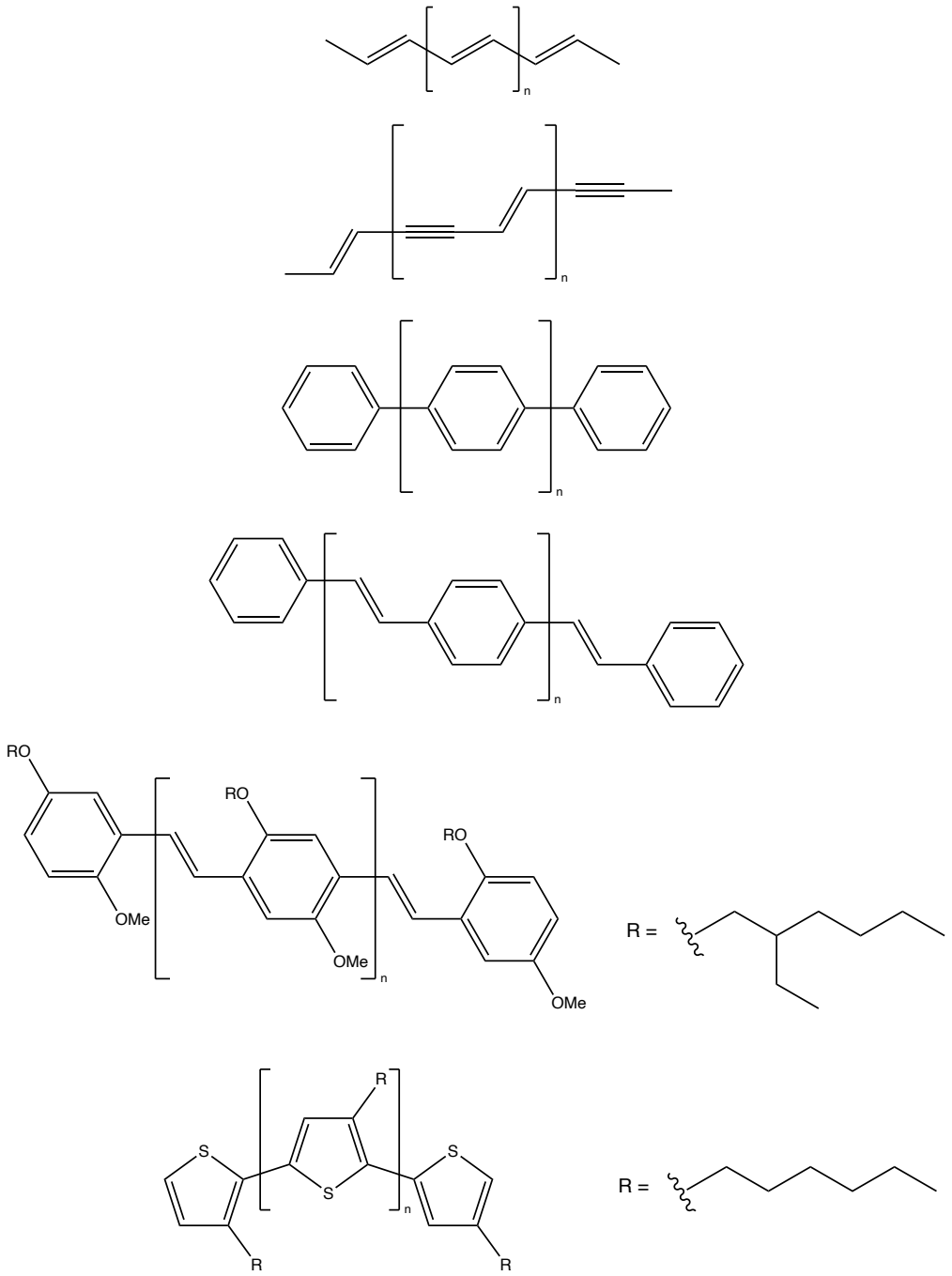


Figure 1.1: Examples of π-conjugated polymer structures. From top to bottom, these are: *trans*-polyacetylene (PA), polydiacetylene (PDA), poly(*p*-phenylene) (PPP), poly(*p*-phenylene-vinylene) (PPV), and poly(2-methoxy-5-(2'-ethylhexyloxy)-*p*-phenylene vinylene) (MEH-PPV), poly(3-hexylthiophene-2,5-diyl) (P3HT).

1.2 Applications

The two applications concerned in this discussion will be those of light emitting devices based on polymeric systems, and photovoltaic devices, specifically, as they are implemented in organic solar cells. The light emitting devices convert an electric voltage difference into (visible) light emission at the active material centre, which is some type of organic material in an organic light emitting diode (OLED) device. A photovoltaic device converts energy absorbed in the form of photoexcitation into electric current. In their current state, organic semiconductors are more suitable for the first use case than the latter.

1.2.1 OLED Devices

Active development of OLEDs was started after Tang and VanSlyke's discovery of efficient electroluminescent diodes in 1987, using two layers of organic active material, 8-hydroxyquinoline aluminium and an aromatic diamine compound.[15] Their discovery was followed by the first report of an OLED device based on polymers in 1990, by Burroughes and co-workers.[10] Both of these devices produced electroluminescence in the blue region of the visible light spectrum. Shortly after, the first white OLED device was reported using multiple layers of active organic materials, each emitting photons at different wavelength values.[16] The basic working principles of an OLED device are shown in Fig. 1.2. At their core, the devices rely on electrons and holes injected at the cathode and anode, respectively, to efficiently recombine in the organic emissive layer.[17]

The development of OLED devices based on both polymers and small organic molecules has seen outstanding interest in recent years. Polymer based approaches

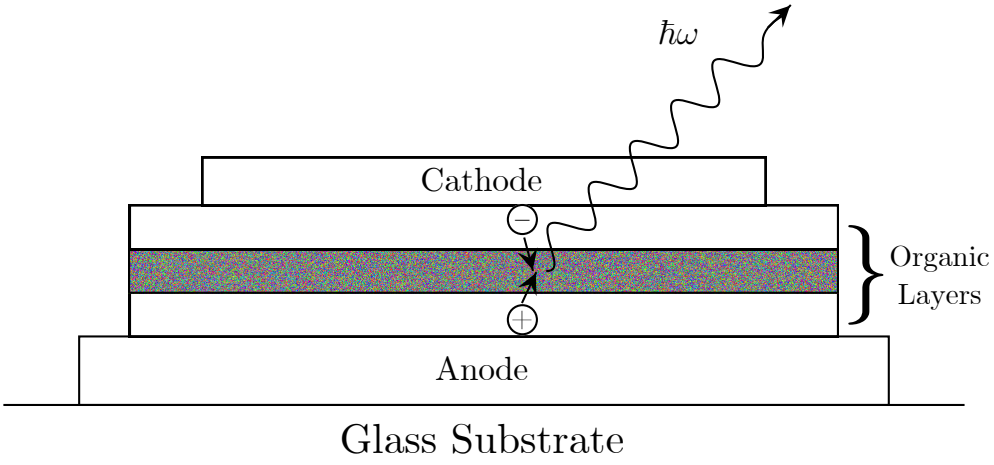


Figure 1.2: The basic operational mechanism of an organic light emitting diode system. The electron and hole generated at the cathode and anode, respectively, recombine within the organic material, producing an excitation. The relaxation of this excitation results in the emission of light. Illustration adapted from Ref. [17].

could be preferred from a manufacturing standpoint, allowing for device manufacturing through straightforward solution deposition techniques and even 3D printing,[18] but fall behind in emission efficiency and overall operating lifetime.[19–21] Regardless, the technology for OLED device manufacturing has reached sufficient maturity for widespread application. The enormous growth of the OLED industry is evidenced by its estimated market volume of 34.3 billion USD in 2020, which is projected to grow rapidly in the years to come.[21]

1.2.2 Photovoltaic Devices

The following discussion focuses on the most common type of photovoltaic devices, solar cells, which convert photon energy from sunlight into electric current. The history of organic solar cells[22] dates back to the middle of the 20^{th} century,[23] when photovoltaic effects in anthracene crystals were first reported. The first polymer based cell was reported in 1982, using trans-polyacetylene. Shortly after, Tang[24] achieved a breakthrough (at the time) 1% power conversion efficiency,

based on a two-layer organic photovoltaic cell, paving the way to heterojunction photovoltaic devices. The underlying working principle in such devices is that charge separation occurs between the different types of active layers, rather than at the interface of the active material and the electrode. The basic mechanism[25] of a heterojunction solar cell is illustrated in Fig. 1.3. In 1995, Yu and co-workers reported[11] a heterojunction solar cell based on a conjugated polymer (MEH-PPV) and fullerene donor-acceptor pair, respectively. This general setup is the basis for the highest efficiency organic solar cells to this day. Over the last two decades, significant improvements have been made,[26] and reported cell efficiencies now exceed 18%.[27]

In general, organic materials have significant benefits as well as disadvantages when compared to their inorganic counterparts. Devices based on organic active materials are easier and cheaper to produce, are easier to tune chemically, and can be implemented in thin and light devices such as wearable electronics, where the inorganic counterparts would be difficult to use.[28] However, challenges, both experimentally and theoretically, remain. Given that band gaps in organic materials such as conjugated polymers are around 2 eV[29] (much higher than the band gap of 1.12 eV of silicon[30]), it is only possible to absorb around 30% (compared to $\sim 77\%$ for silicon) of solar radiation, as the remainder of the photons would not have sufficient energy to induce excitation in the absorbing material.[28] Due to losses to radiative recombination processes, the theoretical limit of highest efficiency for extracted power, called the Shockley-Queisser limit, is considerably lower than this figure.[31] There are numerous approaches to overcome this limitation, such as using multiple different absorbing materials, or utilising singlet fission materials.[32] Further improving solar cells requires the theoretical understanding of the charge transfer processes involved, which is still incomplete despite decades of research into the topic. Outstanding challenges include better understanding exciton migration

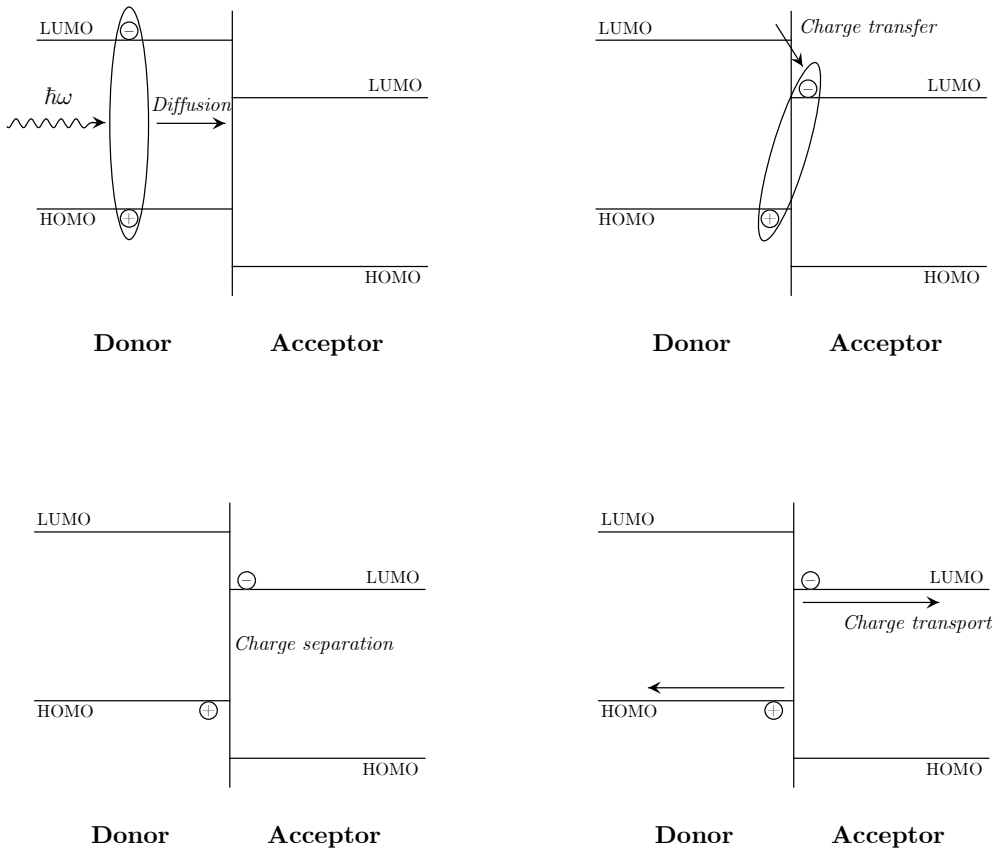


Figure 1.3: The basic operational mechanism of heterojunction organic solar cells. Photoexcitation of the organic absorbing material generates an electron-hole pair, which undergoes charge separation at the donor-acceptor interface. The separated charges are transported to the anode and cathode of the device, resulting in the generation of electric current. Illustration adapted from Ref. [25].

(to the donor-acceptor interface in a heterojunction solar cell) and improving on the low levels of charge mobility in organic materials, both of which limit the practical size of organic thin film layers.[28, 33]

1.3 Charge Transfer

As highlighted above, understanding charge transfer characteristics and underlying mechanisms is crucial to enabling wider use and applications of conjugated polymer systems. Over the past few decades, the scientific literature has seen a rapid growth in publications in the area of organic electronics. Studies of charge transfer

generally focus on two measurable quantities, charge mobility and the diffusion constant, which relate to the charge migration process. These quantities describe the materials' suitability for applications in light emitting devices, field-effect transistors and photovoltaic devices alike. Charge mobility is an extrinsic physical property of a material, and is defined as

$$\mu = \frac{\langle v(F) \rangle}{qF}, \tag{1.1}$$

where $v(F)$ is the electric field dependent drift velocity of a charge moving through the system, q is the charge magnitude and F is the strength of the electric field applied. The diffusion constant, D, is linked to this quantity by the Einstein relation[34]

$$D = \mu k_B T, \tag{1.2}$$

where k_B and T denote the Boltzmann constant and temperature, as usual.

1.3.1 Experimental Background

Experimentally, the most commonly used technique to determine charge mobility is determined through time of flight (TOF) measurements, where a thin film is placed between two electrodes, and after the generation of electron-hole pairs near one electrode through photoexcitation, charge carrier transit time between the electrodes is measured. This method dates back to 1960 for the first measurements of mobility in organic materials.[35–37] It is suitable for measuring mobility on the 'bulk' scale, and is therefore affected by sample impurities and structural disorder.[37, 38] Alternative measurement techniques exist, such as pulse radiolysis time-resolved microwave conductivity (PR-TRMC), where the majority of charge carriers are first excited using high energy electrons, followed by the sample being subjected to microwave radiation. Its ability to reflect this radiation can be used to calculate

electron and hole mobilities. As this is a contact free technique, and because the spatial resolution is determined by the frequency of the microwave radiation, it can be used to measure mobility both on bulk and highly local (even single chain) scale.[37]

Measurements on π-conjugated systems show an exceptionally wide range of mobility values, ranging from as low as 10^{-9} $\mathrm{cm^2\,V^{-1}\,s^{-1}}$ in highly disordered polymer systems up to over 100 $\mathrm{cm^2\,V^{-1}\,s^{-1}}$ for single-chain experiments.[39, 40]. By comparison, inorganic, silicon-based semiconductors have intrinsic mobilities in the $\sim$ 1000 $\mathrm{cm^2\,V^{-1}\,s^{-1}}$ range at room temperature,[41, 42] while some of the highest mobilities have been measured in carbon nanotubes, which can exceed even these figures almost hundredfold.[43] The particularly low mobilities measured by Kryukov et al. in substituted PPV-derivatives[39] using TOF experimental setup is suggestive of disordered polymer structure, but other experimental studies also show overall low bulk mobility values for a range of polymeric systems, including PPV, PPP, P3HT and polycarbonate compounds.[44–58] The highest levels of mobility has been observed in experiments where intrachain charge migration was successfully isolated. Intrachain mobilities measured by Siebbeles and co-workers[40, 59, 60] using PR-TRMC indicate that charge mobility along an individual chain can rival that of inorganic semiconductors, with mobilities of up to 600 $\mathrm{cm^2\,V^{-1}\,s^{-1}}$ for ladder-type poly(p-phenylene)s (LPPPs). Mobility along the structurally more flexible PPV chains was recorded to be an order of magnitude lower, around 60 $\mathrm{cm^2\,V^{-1}\,s^{-1}}$. A rapid drop to $\sim$ 1 $\mathrm{cm^2\,V^{-1}\,s^{-1}}$ for mobility along a single coiled chain was observed, whereas the measured mobilities were significantly lower still, $\ll$ 1 $\mathrm{cm^2\,V^{-1}\,s^{-1}}$ when interchain interactions were included. These insights are particularly useful when comparing experimental data to simulations and theoretical models.

The changing trends in charge mobility based on temperature, the applied field bias and system disorder is a crucial consideration in experimental studies.

Generally, organic semiconductors exhibit a thermally activated transport behaviour, i.e., charge mobility increases with increasing temperature, all other parameters being equal. Looking at a wide range of experimental studies, the emerging trends for temperature dependence paint a confusing picture. While a simple Arrhenius-type dependence, $\mu \propto \exp(-1/T)$, is more commonly observed,[44, 49, 52, 54] some studies show that a different, $\mu \propto \exp(-1/T^2)$, dependence is more accurate.[55, 61] Some authors even argue that over the limited temperature range of experimental studies, either model provides a good enough fit,[47, 53, 62] even though the underlying mechanism to account for each would be drastically different. A notable exception to the thermally activated behaviour is seen in ultrapure molecular crystals, which show high levels of mobility, which decreases with temperature.[63–66] The inferred mechanisms of transport in each case are discussed in the next section.

A characteristic experimental observation arising in conjugated polymer systems is the emergence of the so-called Poole-Frenkel behaviour, which describes the field and temperature dependence of charge mobility as[67–70]

$$\log \mu(F,T) \propto \frac{\sqrt{F}}{T} \tag{1.3}$$

over a range of field strength values. This qualitative behaviour has been shown to be valid for poly(p-phenylenevinylene) (PPV),[49, 52, 57, 58] doped polycarbonate,[45, 46, 48, 71] and poly(3-hexylthiophene) (P3HT)[54] type polymer systems alike. Depending on the system under investigation, both positive[39, 52, 55, 57, 61, 68–70] and negative[54, 58] gradients have been observed with respect to the changing electric field, and some studies even showed changes from positive to negative dependence across the range of field strength values studied.[48, 72–74] The general understanding of this behaviour is linked to the reduced activation barrier of a charge carrier escaping from an energetically trapped state.

Finally, charge-carrier density also significantly affects overall charge mobility. Measured charge mobilities in the organic materials can often differ by several orders of magnitudes, depending on the type of application, e.g., in hole-only diode or field-effect transistors. Blom and co-workers demonstrated[75–77] that the large differences can be attributed to the change in charge-carrier density across these devices.

1.3.2 Computational and Theoretical Overview

Theoretical work on the topic of charge mobility in organic semiconductors has a long history, as understanding the mechanisms limiting charge transport in these materials can lead the way in further improving their viability and applicability.

Gaussian Disorder Model

The seminal work of Bässler and co-workers[78] on organic semiconductors describes charge transport from the standpoint of a non-adiabatic hopping mechanism between states (Anderson) localised by disorder. As this work is of crucial importance in the field of charge transport in organic semiconductors, having been cited over 3000 times since published, and since it provides a suitable starting point, as well as notable points of deviation for the work presented, Bässler's model will be discussed in some detail first.

The organic material is modelled as a lattice of sites, where the site-localised states are modelled to have a Gaussian distribution of on-site energies, linked to the absorption line shapes of such systems, with distribution width on the order of $\sigma \sim 0.1\,\mathrm{eV}$. Bässler's model stipulates a Gaussian distribution of charge transport states:

$$\rho(\epsilon) = \frac{1}{\sqrt{2\pi\sigma^2}} \exp\left(-\frac{\epsilon^2}{2\sigma^2}\right). \tag{1.4}$$

This proposition gives rise to the name Gaussian Disorder Model (GDM), the commonly used literature name for this model. Such disorder stems from local fluctuations of densities and consequently of the electrostatic environment. The original model assumes no correlation in the amount of disorder present in adjacent sites, which is justified through the short length scale of structural correlation in organic glasses, generally not more than a few intermolecular spacings. The model in this early work assumes a simple Miller-Abrahams (MA) transition rate, i.e., $k \propto \exp\left(-\Delta E/k_B T\right)$, between neighbouring lattice sites. The transition rate incorporates a distance-dependent overlap factor, which is used to reflect off-diagonal disorder in the system, and is also modelled as a Gaussian random variable. Since this model does not have an analytic solution, charge migration simulations using kinetic Monte Carlo methods were used to obtain numerical insights. The model, despite its simplicity, reproduced the Poole-Frenkel electric field dependence in the modelled parameter regimes. The expression obtained for charge mobility based on fitting to the simulation results was:[78]

$$\mu = \mu_0 \exp\left[-\left(\frac{2}{3}\frac{\sigma}{k_B T}\right)^2\right] \begin{cases} \exp\left[\mathcal{C}\left(\left(\frac{\sigma}{k_B T}\right)^2 - \Sigma^2\right) F^{1/2}\right] & \Sigma \geq 1.5 \\ \exp\left[\mathcal{C}\left(\left(\frac{\sigma}{k_B T}\right)^2 - 2.25\right) F^{1/2}\right] & \Sigma < 1.5 \end{cases}, \quad (1.5)$$

where σ and Σ are the diagonal and off-diagonal disorder parameters, respectively, while μ_0 is the charge mobility extrapolated to zero field strength in the $T \to \infty$ limit.

Following Bässler's original model, several improvements and adaptations were made over the following decades, notably models incorporating spatially correlated disorder (correlated disorder model, or CDM),[79–81] considering polaronic effects influencing transport through the incorporation of Marcus type transition rates,[82–84] the expression governing charge mobility was understood to take the form:[85–87]

$$\mu = \mu_0 \exp\left[-\left(\frac{E_a}{k_B T}\right)\right] \exp\left[-\mathcal{C}_1\left(\frac{\sigma}{k_B T}\right)^2\right] \exp\left[\mathcal{C}_2\left(\left(\frac{\sigma}{k_B T}\right)^2 - \Sigma^2\right)\sqrt{F}\right], \quad (1.6)$$

where E_a is an activation energy to the transfer process, and $\mathcal{C}_1$ and $\mathcal{C}_2$ are fitting parameters. This expression notably incorporates both a $1/T$ and $1/T^2$ dependence.

The parameters entering the GDM models include lattice spacings derived from structural studies, polaron activation energies and energetic disorder parameters from spectroscopic measurements, as well as incorporating spatial correlation between parameters, which would be expected to be present in real physical systems. However, these studies were generally restricted to simplistic lattice models, incorporating only nearest-neighbour hops. Nonetheless, these models have been able to reproduce experimental trends qualitatively, including the Poole-Frenkel field dependence. The presence of an inverted regime at high field strength values is also confirmed by a number of numerical and analytical studies.[84, 88–92]

Despite the successes of these models, there was a need for bridging the gap between such simplified models and realistic physical systems to be able to provide accurate predictions based on structure-property relations. The models make use of too many parameters which are often forced to take values outside the physically sensible range.[85, 92–95] Treating quantities such as donor-acceptor separation distance and polaron relaxation energies as parameters independent of system disorder is also physically inaccurate. In considering exclusively nearest-neighbour hops in lattice models, long-range charge transfer via quasi-extended states is ignored.[96, 97] Finally, as discussed above, intermolecular and intramolecular transfer occurs at significantly different rates[40] in polymeric systems, and this anisotropic nature of charge transfer must also be accounted for in a realistic model. There are recent examples in literature of models incorporating some of these ideas into a more realistic charge transfer model,[92, 98, 99] either through more refined transition rate expressions or a deviation from strictly lattice based geometries. However, these models are restricted to either single-chain only transfer,

or use reorganisation energies that are set parametrically, or do not reproduce the expected Marcus inverted regime at high field strength values.[84, 88–92] A realistic, atomistic bulk charge mobility model, incorporating all the ideas presented above is the subject of Chapter 4, namely using a realistic polymer structure, exhibiting disorder effects both energetically and structurally, and allowing for both intermolecular and intramolecular charge transfer events, between donor and acceptor states at varying distances from one another.

Quantum Dynamics Methods

The models presented above all consider a static energetic landscape that charge migrates through, which allows for comparatively large system sizes to be examined. An alternative approach to study charge transport mechanisms is to build up an understanding of the transport mechanism from real time evolution of model polymeric systems, albeit limited by the computational effort required for such work. These approaches can provide insights into dynamic processes occurring on different timescales, as well as a more complete picture of how subtle changes in physical parameters affect excited state relaxation. Information about these parameters from dynamically equilibrated systems can also be extracted to then be used in models of the first type. There are numerous examples of charge/exciton dynamics studies in the literature, using a range of time evolution techniques.[100–116] These models all rely on some form of mixed quantum-classical approach, treating nuclear degrees of freedom classically, while retaining quantum mechanical accuracy for the electronic degrees of freedom. The methods used include projected instantaneous eigenstate approaches, mean-field/Ehrenfest methods and surface-hopping algorithms. Finally, it is worth highlighting that there have been several thorough review articles published on the topic of charge transport in organic

semiconductors recently.[87, 117–120] The model presented in Chapter 5 explores such a quantum-classical dynamic process, based on a Brownian-Ehrenfest method, which examines the evolution of charge along a single polymer chain as a result of structural (torsional) fluctuations.

Charge Transport Mechanism

Reflecting on the experimental observations and computational and theoretical approaches from the past decades of active research in the area, the established mechanisms for charge transport can be summarised as follows. Firstly, the basis for the lattice models is the understanding that charge transport occurs as an incoherent hopping process between states highly localised either by polaronic effects or disorder. In the energetic regime relevant for most conjugated polymers, Anderson localisation through disorder is the dominant effect,[121, 122] and it is indeed the basis of the GDM framework introduced above. In addition to the hopping mechanism, more recent works show that additional pathways can be relevant in low disorder systems[63–66, 123] where a high level of charge mobility, though lower than that of inorganic semiconductors, is coupled with temperature dependence that is consistent with band-like conduction models commonly used in inorganic semiconductors. While this latter model is not generally compatible with most organic semiconductor systems, the recent theory of transient localisation (TL)[120, 123–125] gives an explanation for the observed trends. Within the TL framework, charge transport is inhibited by large amplitude molecular motion, resulting in dynamic disorder in the system, which localises charge carriers, even in the absence of static disorder. This behaviour was previously predicted theoretically,[101] where thermal disorder also showed a decrease in charge mobility in the ordered organic semiconductor model system. TL theory gives an estimate of charge mobility

dictated by the transient localisation length and the corresponding timescale of the motion leading to this localisation. The theory is consistent with experimental mobility measurements performed under high pressure and low temperature where thermal disorder is suppressed,[126] and the time dependence of diffusivity extracted from optical conductivity measurements.[124, 127]

1.4 Thesis Structure

The aim of this thesis is to examine the mechanism of charge transfer in π-conjugated model polymer systems in two distinctly different regimes – in a 'bulk' disordered system, and along a single polymer chain as a consequence of the subtle effects of environmental noise affecting the torsional motion. In Chapter 2, the required theoretical background is described, including the Holstein system Hamiltonian employed, the theory of the dynamics of transitions in 2-level quantum mechanical systems, and the considerations required for mixed quantum-classical dynamics models. The description of charge transfer in the framework of Marcus theory, as well as an introduction to Langevin dynamics, which is used to describe the stochastic processes studied, is also presented. Chapter 3 contains the general introduction of computational methods used in the work undertaken, most notably a summary of the framework of matrix product states to describe quantum mechanical systems, as well as the description of efficient time evolution techniques and integration schemes. The implementation of periodicity within the computational framework is also detailed. An atomistic model of charge migration in an extended disordered PPV polymer system is presented in Chapter 4. The dependence of charge mobility on polymer structure, electric field strength, temperature and various sources of disorder are examined and discussed. In Chapter 5, a quantum-classical model of intramolecular charge dynamics is presented. Charge migration is induced by

Brownian fluctuations of the torsional modes in the polymer structure, and is followed over long dynamics simulations. A mechanistic crossover between low temperature, purely adiabatic regime and a hopping regime is presented. Finally, Chapter 6 concludes this thesis with a summary of the results and with a look at potential future directions for research.

2
Theoretical Background

Modelling charge migration in conjugated polymers is a complex challenge. Computations need to encapsulate processes on multiple scales simultaneously. The length scales considered include vibrations along a single carbon-carbon bond up to hundreds of polymer chains, each made up of hundreds of atoms. Considering the dynamics of electronic states, vibrations, torsional motion and of dissipative random system-bath interactions requires extended simulations. The charge transfer processes modelled include competing intra-molecular and inter-molecular interactions. Disorder in the polymer structures and environment plays a significant role in the electronic structure of the polymers, and needs to be incorporated to model realistic systems. In trying to model inherently bulk material physical processes, we are restricting our studies to moderate to large system sizes. The large number of atoms and electrons involved make exact quantum mechanical description of our systems impossible. In this chapter, we will examine how these physical systems can be translated into a theoretical description that allows us to make the problem tractable while still giving us insights into the subtle and interesting processes manifesting in these systems. The general themes of the thesis are examined here, but the ideas are further refined in later chapters when necessary.

2.1 Quasi-1D Quantum Systems

The π-conjugated polymers under consideration all share the same structural motif – each molecule is a quasi-one dimensional chain of repeating monomers. These polymers have an extended π-electron system, with an electron in p_z-orbitals on each carbon atom of the molecular framework that is contributed to a connected electronic structure spanning significant parts, and often the whole length of the molecule. Such systems are often described by π-electron models which only directly consider these electrons, independently of the σ-bonded framework of the molecule. This is the first approximation we take when describing the systems in the following works.

2.1.1 Hückel Model

The simplest such model is the Hückel model. The Hamiltonian for this model can be written in an atomic basis as

$$\hat{H}^{\text{atomic}}_{\text{Hückel}} = -\sum_i t_i \left(\hat{c}_i^\dagger \hat{c}_{i+1} + \hat{c}_{i+1}^\dagger \hat{c}_i\right), \tag{2.1}$$

where t_i is the transfer integral between nearest neighbour atomic orbitals, and $\hat{c}_i^\dagger$ and $\hat{c}_i$ correspond to the creation and destruction of an electron in orbital i, respectively. There is no term corresponding to the on-site energies of orbitals, as the p_z-orbitals are degenerate and their energies can be set to zero. This model, and following ones building on this base model, do not incorporate electron-electron interactions. This choice is justified through a number of considerations. The quasi-particle description of excitations leads to renormalised parameters in simulations. The use of such empirical parameters can absorb some of these effects while retaining quantitatively good results in the physical processes described. In particular, the Holstein model, introduced below, works well in describing charge-polarons in phenyl-based conjugated polymers, where electron-electron correlations are comparatively

weaker than in linear polyenes.[128] Finally, given the large variety of interactions in the rich physics of conjugated polymers, it is difficult to include all contributions to the same level of detail. In this thesis, disorder effects and electron-phonon interactions receive a greater emphasis, and therefore the choice of employing a suitable non-interacting Hamilonian was made.

2.1.2 Coarse-grained Systems

The representation of the polymer chains is further simplified by a coarse-graining process that replaces the molecular structure of repeating monomers by a chain of sites, each site representing multiple atoms of the molecule. This process is demonstrated through the example of poly(*p*-phenylene-vinylene) (PPV). As illustrated in Fig. 2.1, each moiety of the polymer is represented by a site in all future calculations. The coarse-graining also necessitates recasting the Hamiltonian in a new, site-based basis.

$$|i\rangle = \hat{c}_i^\dagger|0\rangle \qquad \Rightarrow \qquad |n\rangle = \hat{a}_n^\dagger|0\rangle, \tag{2.2}$$

where the atomic basis, $\{|i\rangle\}$, is replaced by a site basis, $\{|n\rangle\}$, and the new creation (and destruction) operators, $\hat{a}_n^\dagger$ (and $\hat{a}_n$), correspond to the new coarse-grained basis.

The new, coarse-grained Hückel Hamiltonian is thus

$$\hat{H}_{\text{Hückel}}^{\text{cg}} = \sum_n \epsilon_n \hat{a}_n^\dagger \hat{a}_n - \sum_n \tilde{t}_n \left(\hat{a}_n^\dagger \hat{a}_{n+1} + \hat{a}_{n+1}^\dagger \hat{a}_n\right). \tag{2.3}$$

The first term in Eq. (2.3) are the on-site energies, with ϵ_n taking different values for even and odd sites, corresponding to the different moieties in PPV. The transfer (or hopping) term is defined as

$$\tilde{t}_n = \tilde{t}_0 \cos(\theta_n), \tag{2.4}$$

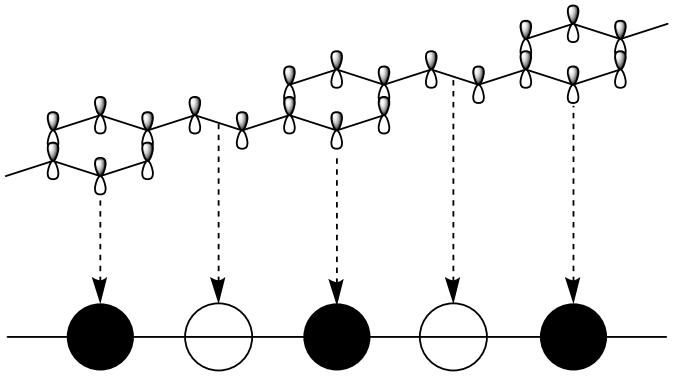


Figure 2.1: The coarse-graining of PPV into two sites per monomer, corresponding to each phenylene and vinylene moiety.

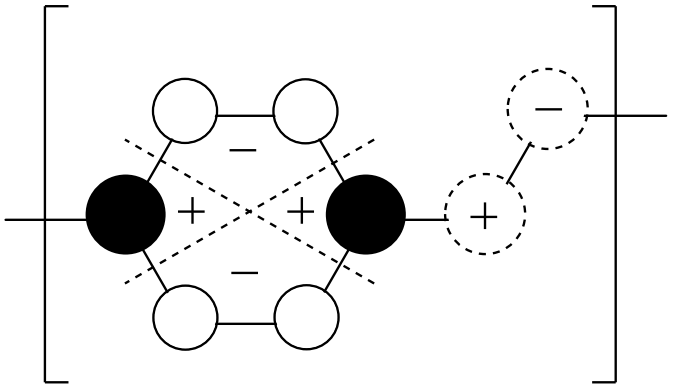


Figure 2.2: Coefficients of the atomic orbitals, φ_i, contributing to the local LUMO wavefunctions of PPV. $\varphi_{\text{filled}} = 1/\sqrt{3}$, $\varphi_{\text{unfilled}} = 1/\sqrt{12}$, $\varphi_{\text{dashed}} = 1/\sqrt{2}$, with the signs of these coefficients indicated accordingly.

with θ_n denoting the dihedral angle between neighbouring polymer moieties, and $\tilde{t}_0$ the transfer integral between planar moieties. The coarse-grained $\tilde{t}_0$ it linked to t_0 in the atomic basis set by $\tilde{t}_0 = t_0/\sqrt{6}$, arising as the product of orbital coefficients on the linking carbon atoms in the LUMO states of the phenylene and vinylene moieties, $1/\sqrt{3}$ and $1/\sqrt{2}$, respectively, as defined by the atomic orbital coefficients illustrated in Fig. 2.2.

2.1.3 Holstein Hamiltonian

Electron transfer occurs between the lowest unoccupied molecular orbitals (LUMO) (or equivalently, hole transfer between the highest occupied molecular orbitals, HO-

MOs) in each moiety. This transfer process is captured by the Hückel Hamiltonian. The Holstein Hamiltonian[129, 130] expands this simple model by adding terms to account for polaronic effects. Taking one phonon mode on each site, coupled to the electronic degrees of freedom on that site, the full Holstein Hamiltonian can be written as[131]

$$\hat{H}_{\text{Holstein}} = \hat{H}^{\text{cg}}_{\text{Hückel}} - \sum_n \Gamma_n Q_n \hat{a}^\dagger_n \hat{a}_n + \frac{K}{2}\sum_n Q_n^2 + \frac{1}{2M}\sum_n P_n^2, \tag{2.5}$$

where Q_n is the normal coordinate of the phonon mode on site n, and Γ_n is the charge-phonon coupling parameter. The coupling is assumed to be linearly dependent on the normal coordinate displacement, Q_n.[131, 132] The additional terms compared to the Hückel Hamiltonian therefore correspond to the charge-phonon coupling, and the elastic and kinetic energies of the phonon modes, respectively. K is the force constant and M is the reduced mass of the oscillator. Rewriting Eq. (2.5) using the dimensionless variables

$$\tilde{Q}_n = \left(\frac{M\omega}{\hbar}\right)^{1/2} \tag{2.6}$$

$$\tilde{P}_n = \left(\frac{1}{M\hbar\omega}\right)^{1/2}, \tag{2.7}$$

where $\omega = \sqrt{K/M}$ is the angular frequency of the oscillator, we get

$$\hat{H}_{\text{Holstein}} = \hat{H}^{\text{cg}}_{\text{Hückel}} - \hbar\omega \sum_n A_n \tilde{Q}_n \hat{a}^\dagger_n \hat{a}_n + \frac{\hbar\omega}{2}\sum_n \left(\tilde{Q}_n^2 + \tilde{P}_n^2\right), \tag{2.8}$$

where $A_n = \Gamma_n/(M\hbar\omega^3)^{1/2}$ is the dimensionless charge-phonon coupling parameter.[128]

Born-Oppenheimer Approximation

The Born-Oppenheimer (BO) approximation[133] is a further approximation often applied to conjugated polymer systems. The approximation assumes that due to

significantly larger mass of the nuclei compared to the electrons, the dynamics of electrons is significantly faster than that of nuclear degrees of freedom. This means that under the Born-Oppenheimer (or adiabatic) approximation, the overall state of the system can be factorised into the direct product of a nuclear and an electronic component, as shown in Eq. (2.9).

$$\Psi^{\mathrm{BO}}(\mathbf{r}, \mathbf{R}) = \psi_{\mathrm{el}}(\mathbf{r}; \{\mathbf{R}\})\psi_{\mathrm{nuc}}(\mathbf{R}), \tag{2.9}$$

where the electronic wavefunction, ψ_{el} depends on the electronic coordinates, $\mathbf{r}$, and is assumed to only depend parametrically on the nuclear coordinates, $\{\mathbf{R}\}$, while the nuclear wavefunction, ψ_{nuc}, only depends on the instantaneous nuclear coordinates, $\mathbf{R}$. Within the BO approximation, we therefore neglect the kinetic contributions from the nuclear degrees of freedom and have[4]

$$P\psi_{\mathrm{el}}(\mathbf{r}; \{\mathbf{R}\}) \approx P^2\psi_{\mathrm{el}}(\mathbf{r}; \{\mathbf{R}\}) \approx 0, \tag{2.10}$$

which means that we obtain the Schrödinger equation for the electronic degrees of freedom using the BO Hamilonian,

$$\hat{H}^{\mathrm{BO}}\psi_{\mathrm{el}}(\mathbf{r}; \{\mathbf{R}\}) = E_{\mathrm{el}}(\{\mathbf{R}\})\psi_{\mathrm{el}}(\mathbf{r}; \{\mathbf{R}\}), \tag{2.11}$$

where the BO Hamiltonian incorporates all terms besides the kinetic energy of the nuclear degrees of freedom. In general, the Born-Oppenheimer approximation is valid for conjugated polymer systems, given that $\hbar\omega/|t| \sim 0.1$ is typical for these systems.[131] Applying the BO approximation, the Holstein Hamiltonian in Eq. (2.8) simplifies to the following model Hamiltonian:

$$\hat{H}^{\mathrm{BO}}_{\mathrm{Holstein}} = \hat{H}^{\mathrm{cg}}_{\mathrm{Hückel}} - \hbar\omega \sum_n A_n \tilde{Q}_n \hat{a}_n^\dagger \hat{a}_n + \frac{\hbar\omega}{2} \sum_n \tilde{Q}_n^2. \tag{2.12}$$

The phonon modes of phenylene and vinylene units considered in this work are illustrated in Fig. 2.3. These correspond to a benzoid-quinoid distortion of the phenyl ring and a stretching mode of the vinylene unit.[4, 132, 134, 135]

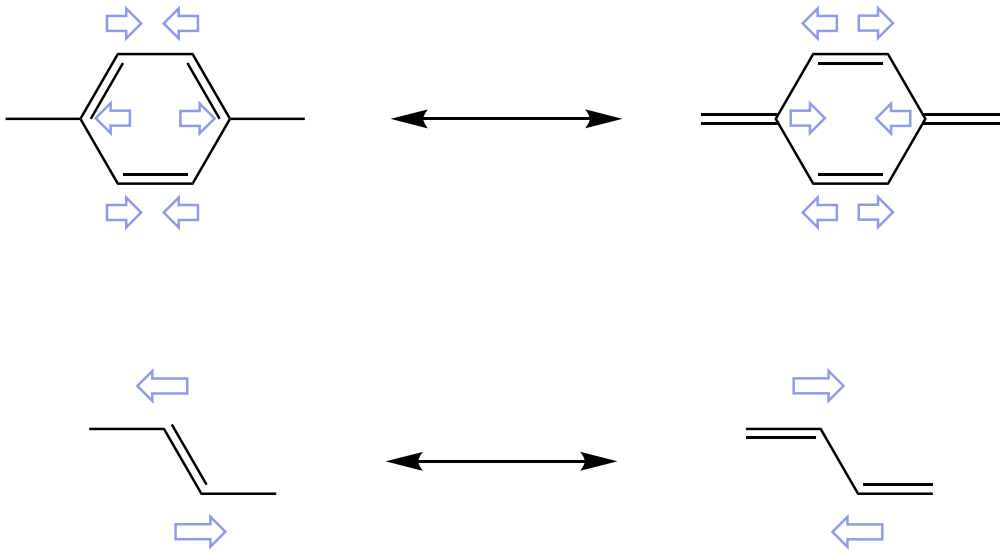


Figure 2.3: Phonon modes of phenylene and vinylene moieties.

2.1.4 Disorder and Localised States

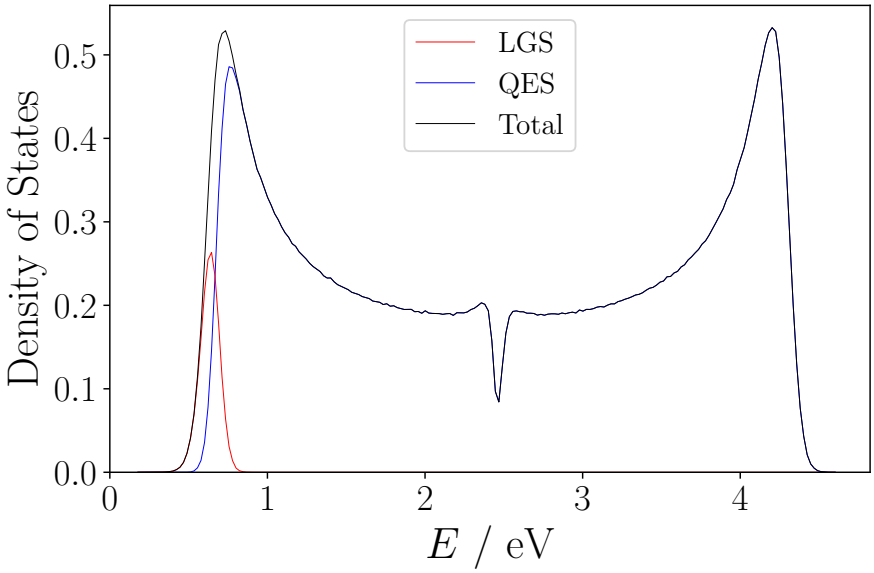


Figure 2.4: Density of states in disordered polymer systems, with $\sigma_\epsilon = 0.2\,\text{eV}$ and $\sigma_\theta = 10°$. The distribution of LGSs and QESs is shown individually. LGSs are the energetically lowest lying states.

In real polymer systems variations in density (and therefore in the local electrostatic environment) and torsional motion in the molecules result in fluctuations in the on-site energy terms, ϵ_n, and through fluctuations in the torsional angles,

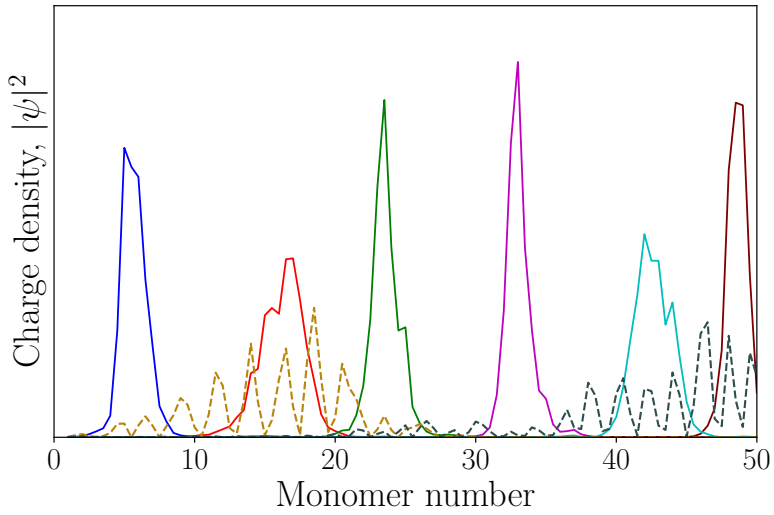


Figure 2.5: LGSs (solid lines) and two QESs (dashed lines) for a polymer chain made up of 50 monomer units. LGSs are localised to a few monomer units and are quasi-nodeless, whereas QESs are more delocalised along the chain and have nodes. ψ_n is obtained from Eq. (2.3).

θ_n, in the off-diagonal transfer terms, $\tilde{t}_n$ as per Eq. (2.4). In the context of this model, density fluctuations stem from molecular translational motion, occurring on a slower timescale than that of charge transfer. This disorder therefore becomes constant (or "static") from the perspective of charge dynamics. Such disorder results in the localisation of states along the polymer chains through Anderson localisation.[136–139]

Anderson localisation is the phenomenon of eigenstates of a system being spatially localised to a subset of the overall system, caused by disorder in the system. The disorder manifests as randomly distributed potential barriers, and leads to destructive interference of wave packets along the chain, leading to the exponential localisation of states along the chain.[128] This process is illustrated in Fig. 2.6. Anderson localisation has been shown to occur in all one-dimensional systems with finite disorder.[137, 140]

Two distinctly different types of states arising through localisation are considered. The lowest energy states will be highly localised, quasi-nodeless states, extending

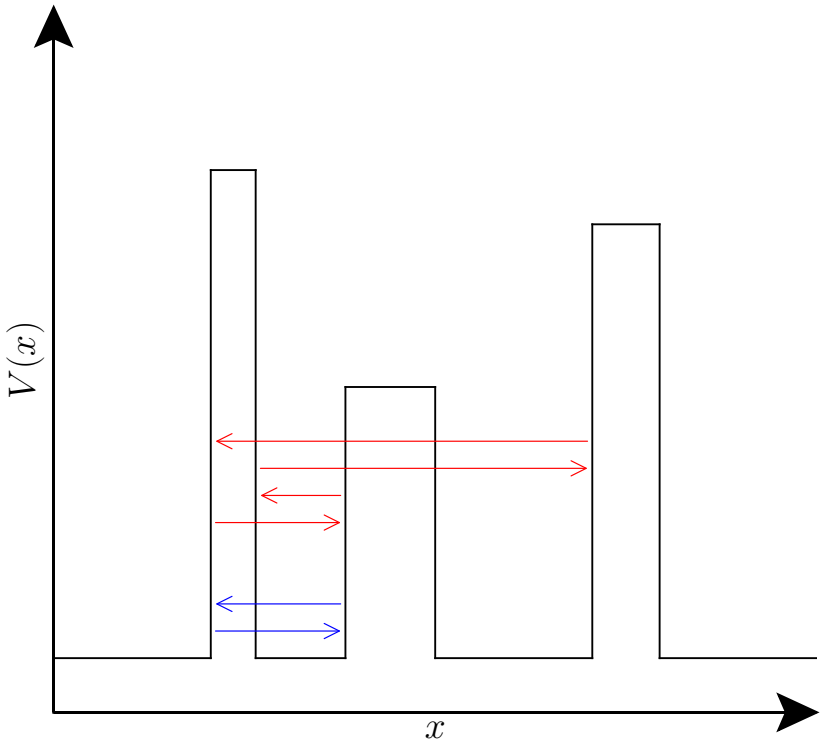


Figure 2.6: Disorder in the system acts as unevenly spaced potential barriers of varying sizes, leading to destructive interference of wave packets, and therefore localisation.

over a few monomers in the polymer chain, whereas higher energy states will be spread across a larger portion of the chain. These states are called local ground states (LGSs) and quasi-extended states (QESs), respectively. The classification of states as LGS or QES is performed using the 'signed-value' parameter (SVP)[138]

$$\text{SVP} = \left| \sum_n \psi_n |\psi_n| \right|. \tag{2.13}$$

where ψ_n is the wavefunction corresponding to the given state, and the sum is taken over all sites, n. ψ_n is found by diagonalising Eq. (2.3) for a particular value of the disorder.

LGSs are defined as states with a corresponding SVP value greater than 0.95,[138] while the remaining states are classified as QES. The density of states (DOS) shown

in Fig. 2.4 illustrates how the LGSs are the energetically lowest lying states. LGSs lie in the Lifshitz tail of the DOS and have approximately a Gaussian density of states.[141] It should be noted that the dip in the centre of the DOS arises because there are two π-conduction (valence) bands, arising from the different LUMO (HOMO) energies of the phenylene and vinylene moieties. The different states and their spatial extents are illustrated in Fig. 2.5.

Disorder in the models presented is implemented assuming that both the on-site energies and the torsional angles are assumed to follow a Gaussian distribution, with standard deviations σ_ϵ and σ_θ, respectively. To first order, fluctuations in the transfer integral can therefore be quantified by

$$\sigma_t = t_0 \sin(\theta_0)\sigma_\theta. \tag{2.14}$$

The formula above is not suitable for $\theta_0 = 0$, and higher order terms would need to be included. The width of the low energy portion of the density of states is linked to the individual disorder contributions from the on-site energetic and torsional angle fluctuations. The effective disorder contribution from each is given by exchange narrowing[142] as

$$\sigma_{\text{eff}} \sim \frac{\sigma}{\sqrt{L}}, \tag{2.15}$$

where L is the localisation length. In a system with Gaussian disorder, the localisation length near the band edge is lower than at the band centre, as has been shown theoretically[138] and numerically,[139, 143, 144] and is linked to the transfer integral, t, as

$$L \sim \left(\frac{t}{\sigma_t}\right)^{\frac{2}{3}}, \tag{2.16}$$

and therefore

$$\sigma_{t,\text{eff}} \sim \left(\frac{\sigma_t^4}{t}\right)^{\frac{1}{3}}. \tag{2.17}$$

For the calculation parameters, to be presented in Chapter 4 (Table 4.1), with $\sigma_\theta = 10^\circ$ and $\sigma_\epsilon = 0.2\,\text{eV}$, we obtain $\sigma_{t,\text{eff}} \sim 8.49\,\text{meV}$, and $\sigma_{\epsilon,\text{eff}} \sim \sigma_\epsilon/\sqrt{L} \sim 62.5\,\text{meV}$. Combining these contributions for an overall energetic disorder, we get

$$\sigma_E = \left(\sigma_{\epsilon,\text{eff}}^2 + \sigma_{t,\text{eff}}^2\right)^{\frac{1}{2}} \approx 63\,\text{meV}, \tag{2.18}$$

which is indeed the full width at half maximum (FWHM) of the LGS portion of the density of states in Fig. 2.4. The disordered Holstein model forms the basis of the simulation work presented in Chapter 4.

It is worth noting here that a different type of localisation, resulting from the coupling of the particle wavefunction to the local normal modes, is also possible. This 'self-trapping' is inherently different from the Anderson localisation above and is discussed in Chapter 5.

2.2 Theory of Charge Transfer

2.2.1 Landau-Zener Theory

The generic description of a two-level Hamiltonian system with a dynamically changing coupling between the levels is captured by Landau-Zener (LZ) theory.[145–149] We will first derive the main results of LZ theory, then apply these to arrive at expressions for the rate of charge transfer processes within the framework of LZ theory. Let us first consider the two level Hamiltonian,[34]

$$\hat{H} = \hat{H}_0 + \hat{V}, \tag{2.19}$$

with

$$\hat{H}_0 = E_a(Q)\,|a\rangle\,\langle a| + E_b(Q)\,|b\rangle\,\langle b| \tag{2.20}$$

$$\hat{V} = V_{ab}\,|a\rangle\,\langle b| + V_{ba}\,|b\rangle\,\langle a|\,, \tag{2.21}$$

where Q is the time-dependent dynamic variable controlling the Hamiltonian; and the parameters $E_a(Q)$, $E_b(Q)$, V_{ab} fulfil the following relations: at $t \to \pm\infty$, $|E_a - E_b| \gg |V_{ab}|$; and there is some intermediate crossover time, t_C, with corresponding $Q(t_C) \equiv Q_C$ such that $E_a(Q_C) = E_b(Q_C)$.

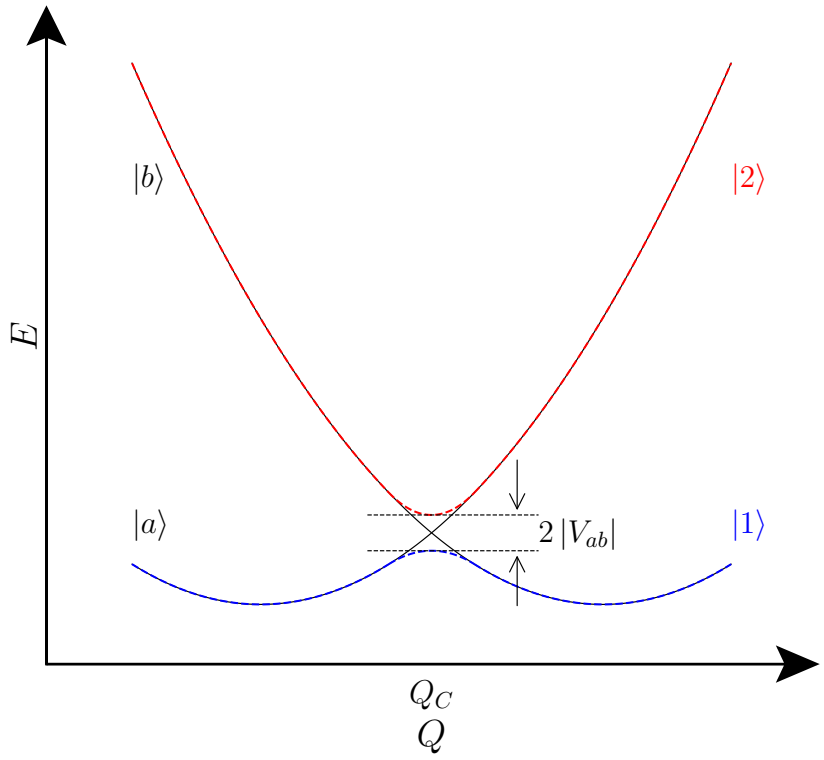


Figure 2.7: Diabatic states, $|a\rangle$ and $|b\rangle$, crossing in energy at $Q = Q_C$, and adiabatic states, $|1\rangle$ and $|2\rangle$, showing the avoided crossing and the correct asymptotic behaviour as $t \to \pm\infty$ (and consequently, $Q \to \pm\infty$).

Starting in state $|a\rangle$ at $t \to -\infty$, we look at the probability of the system ends up in state $|b\rangle$ at $t \to \infty$, denoted as $P_{b\leftarrow a}$. As such, this model effectively describes a semiclassical model of non-adiabatic transitions between two electronic states,

where the variable Q could represent the nuclear coordinates of the system.[34] The LZ problem is illustrated in Fig. 2.7, with the crossover between diabatic states, $|a\rangle$ and $|b\rangle$, occurring at Q_C. The states $|a\rangle$ and $|b\rangle$ are referred to as the *diabatic* states, whereas states $|1\rangle$ and $|2\rangle$, obtained through diagonalising the Hamiltonian, are the *adiabatic* states. Q is varied such that $Q \to -\infty$ as $t \to -\infty$ and $Q \to \infty$ as $t \to \infty$. Assuming that Q varies linearly in time, we have

$$E_a - E_b = F(Q - Q_C) = \alpha t, \tag{2.22}$$

where $F = \partial(E_a - E_b)/\partial Q$ is the force between the energy surfaces experienced along the coordinate Q. Therefore, the energy surfaces approach each other as

$$\frac{\mathrm{d}(E_a - E_b)}{\mathrm{d}t} = \dot{Q}F, \tag{2.23}$$

where $\dot{Q} = \alpha/F$ is the nuclear velocity.[34]

Writing the system as a linear combination in either the diabatic or adiabatic basis, we have

$$|\psi(Q)\rangle = C_a(Q)\,|a\rangle + C_b(Q)\,|b\rangle = C_1(Q)\,|1\rangle + C_2(Q)\,|2\rangle\,, \tag{2.24}$$

where the probability amplitudes C_i fulfils normalisation constraints $|C_a(Q)|^2 + |C_b(Q)|^2 = |C_1(Q)|^2 + |C_2(Q)|^2 = 1$ and the initial conditions $|C_a(Q \to -\infty)|^2 = |C_1(Q \to -\infty)|^2 = 1$. Solving for the transition probability, we get the LZ solution[34]

$$P_{b\leftarrow a} = |C_b(Q \to \infty)|^2 = 1 - \exp\left\{\frac{2\pi\,|V_{ab}|^2}{\hbar\alpha}\right\} \tag{2.25}$$

and consequently,

$$P_{a\leftarrow a} = |C_a(Q \to \infty)|^2 = 1 - |C_b(Q \to \infty)|^2 = \exp\left\{\frac{2\pi\,|V_{ab}|^2}{\hbar\alpha}\right\}. \tag{2.26}$$

Notably, looking at the two limits of these solutions, in the *adiabatic* limit, when changes are slow (small α) or the coupling between the two levels are large, we get $P_{b\leftarrow a}^{\text{adiabatic}} = 1$ and $P_{a\leftarrow a}^{\text{adiabatic}} = 0$, meaning the evolution proceeds on the lower adiabatic surface. Conversely, in the *non-adiabatic* limit, when changes are fast or there is weak coupling between the levels, $2\pi|V_{ab}|^2 \ll \hbar\alpha$ and therefore

$$P_{b\leftarrow a}^{\text{non-adiabatic}} \approx \left\{ \frac{2\pi \left|V_{ab}\right|^2}{\hbar\alpha} \right\} \ll 1 \tag{2.27}$$

$$P_{a\leftarrow a}^{\text{non-adiabatic}} \approx 1 - \left\{ \frac{2\pi \left|V_{ab}\right|^2}{\hbar\alpha} \right\} \approx 1. \tag{2.28}$$

This means that the system generally remains on the diabatic surface $|a\rangle$, with a small probability of a "jump" onto the lower diabatic surface $|b\rangle$ at the crossover point Q_C.

The derived transition *probabilities* between two levels of a system can now be used to establish transition *rates* for charge transfer, where the two levels considered are the electronic states involved in a charge transfer process. A model transition process is illustrated in Fig. 2.8, where the energy curves corresponding to the two electronic states are assumed to be quadratic and of the same curvature.[34] Assuming the transition to preserve energy, it is required to take place at the energetic crossing of the diabatic curves shown, at $Q = Q_C$. The activation energy of this reaction is given by

$$E_{\text{act}} = E_C - E_D^0 = \frac{1}{2}K(Q_C - Q_A)^2 = \frac{\left[(E_D^0 - E_A^0) - E_\lambda\right]^2}{4E_\lambda}, \tag{2.29}$$

where $E_\lambda = \frac{1}{2}K(Q_D - Q_A)^2$ is the reorganisation energy and K is the force constant. According to transition state theory, the rate of transfer is

$$k = \int_0^\infty \dot{Q} P(Q_C, \dot{Q}) P_{b\leftarrow a}(\dot{Q})\, \mathrm{d}\dot{Q}, \tag{2.30}$$

where $P(Q_C, \dot{Q})$ is the LZ transition probability from Eq. (2.25), and

$$P(Q_C, \dot{Q}) = \left(\frac{m}{2\pi k_B T}\right)^{1/2} \exp\left(-\frac{m\dot{Q}^2}{2k_B T}\right) \frac{\exp\left(-\frac{E_{\text{act}}}{k_B T}\right)}{\underbrace{\int_{-\infty}^{Q_C} \exp\left(-\frac{E_D(Q)-E_D^0}{k_B T}\right) \mathrm{d}Q}_{\approx\left(\frac{K}{2\pi k_B T}\right)^{1/2} \exp\left(-\frac{E_{\text{act}}}{k_B T}\right)}} \tag{2.31}$$

is the joint Boltzmann probability density of reaching the normal coordinate $Q = Q_C$ with speed $\dot{Q}$.[34]

In the adiabatic limit, when we have $P_{A\leftarrow D}^{\text{adiabatic}} \to 1$, the rate expression simplifies to

$$k_{\text{ad}} = \frac{\omega}{2\pi} \exp\left(-\frac{\tilde{E}_{\text{act}}}{k_B T}\right), \tag{2.32}$$

where $\omega = (K/m)^{1/2}$, and $\tilde{E}_{\text{act}} = E_{\text{act}} - |V_{AD}|$ is the adiabatic activation energy as can be seen in Fig. 2.7. This expression is the standard Arrhenius form that can be expected from transition state theory.

Looking at the non-adiabatic limit, we now have (as per Eq. (2.27))

$$P_{A\leftarrow D}^{\text{non-adiabatic}} \approx \frac{2\pi \left|V_{DA}\right|^2}{\hbar F \dot{Q}}, \tag{2.33}$$

so the rate expression becomes

$$\begin{aligned} k_{\text{na}} &= \frac{2\pi |V_{DA}|^2}{\hbar F} \underbrace{\int_0^\infty \left(\frac{m}{2\pi k_B T}\right)^{1/2} \left(\frac{K}{2\pi k_B T}\right)^{1/2} \exp\left(-\frac{m\dot{Q}^2}{2k_B T}\right) \mathrm{d}\dot{Q}}_{\frac{(mK)^{1/2}}{2\pi k_B T}\left(\frac{2\pi k_B T}{m}\right)^{1/2}} \exp\left(-\frac{E_{\text{act}}}{k_B T}\right) \\ &= \left(\frac{\pi K}{2k_B T}\right)^{1/2} \frac{|V_{DA}|^2}{\hbar F} \exp\left(-\frac{E_{\text{act}}}{k_B T}\right), \end{aligned} \tag{2.34}$$

where $F = K(Q_A - Q_D)$. Notably, the non-adiabatic rate's dependence on the square of the coupling strength, $|V_{DA}|^2$, indicates a perturbation theory expression, and shows agreement with the Marcus theory expressions (up to a factor of 2), presented in the following section.

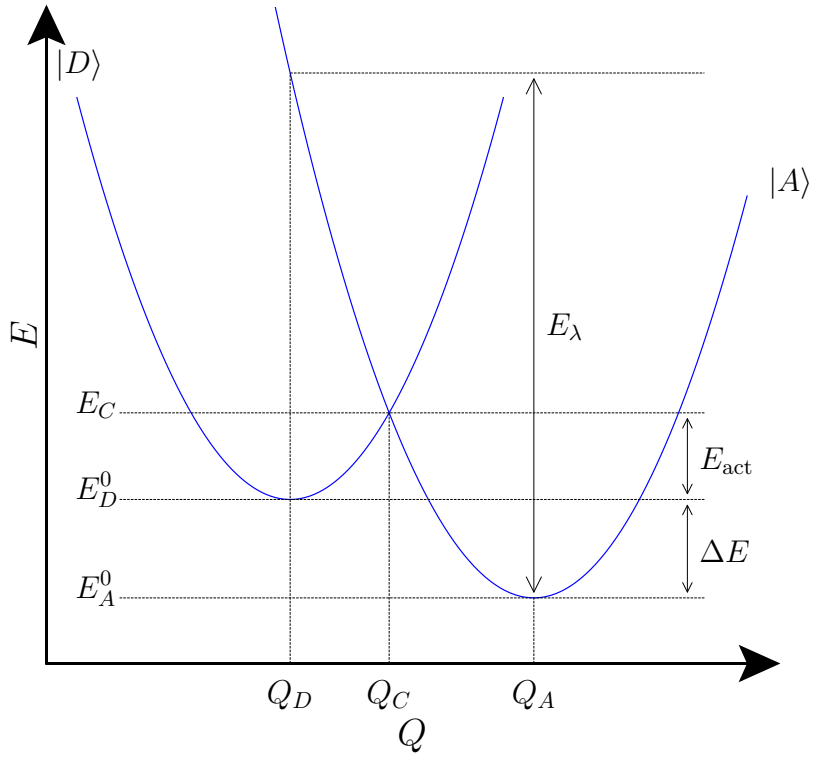


Figure 2.8: Model picture of charge transfer process. The reaction coordinates Q_D, Q_A, Q_C represent the equilibrium coordinates of the donor and acceptor states, and the coordinates corresponding to the crossover of the energy curves, respectively. These coordinates have corresponding energy levels E_D^0, E_A^0, and E_C. The definitions of the driving force, ΔE, the reorganisation energy, E_λ, and the activation energy, E_{act}, are also shown. Figure reproduced from Ref. [34].

2.2.2 Marcus Theory

While the preceding section provided a robust theoretical description of a two-level system and transition rates between the states of such a system (in the context of charge transfer processes), linking those results to a real world physical system is not trivial. The physical relevance and applicability of the parabolic energy surface and the nature of the coordinate Q used is not clear. Marcus theory[150, 151] attempts to make this link by looking at the charge transfer process in the context of a continuum dielectric picture of a polar solvent environment.[34] The underlying

picture of Marcus theory assumes that the timescale of the electron transfer is faster than that of the nuclear motions, and therefore charge transfer occurs at fixed nuclear coordinates, effectively imposing the Franck-Condon principle on the process.[152, 153] An important challenge in this picture is that while nuclear motion is slow, the redistribution of charge density accompanying the charge transfer from a donor to acceptor state can have significant energetic penalties, unless the nuclear positions and surrounding solvent structure already support this transition energetically. The model requires that such a rearrangement, through the fluctuation of nuclear and solvent degrees of freedom, happens before the charge transfer event can take place, at those fixed (on the relative timescales) positions. The transition therefore relies on these fluctuations, bringing about changes in the electrostatics of the polar solvent environment. Marcus theory identifies the relevant potential energy surfaces as free energy surfaces, linked to coordinates describing the polarisation of the solvent. The electrostatic model also necessitates the shared curvature of the potential energy surfaces that was assumed in the LZ derivation previously.[34]

Deriving a transition rate expression in this picture, we start from the Fermi Golden Rule (FGR) formalism, which is valid in the non-adiabatic regime described, and consider the low temperature limit in the first instance, where $k_B T \ll \hbar\omega_n$ for all normal modes n. Considering the initial (donor) and final (acceptor) states of the transfer process, within the Born-Oppenheimer approximation,

$$|X\rangle = |x; \{Q\}\rangle|\nu_x\rangle, \tag{2.35}$$

where $|x; \{Q\}\rangle$ is the electronic state, and $|\nu_x\rangle$ the corresponding nuclear state, for $X = D$ or A for donor and acceptor states, respectively. Simplifying the derivation, unimolecular (or intra-chain) processes are considered first, where the coordinate

Q is shared between donor and acceptor states. The charge transfer process is facilitated by the coupling term,

$$V_{DA} = \left\langle A \middle| H^{(1)} \middle| D \right\rangle, \tag{2.36}$$

where

$$H^{(1)} = -\sum_{i\in D, j\in A, \sigma} t_{ij} \left(\hat{a}^{\dagger}_{i\sigma} \hat{a}_{j\sigma} + \hat{a}^{\dagger}_{j\sigma} \hat{a}_{i\sigma} \right) \tag{2.37}$$

is the one-electron integral. Inserting the BO state definitions from Eq. (2.35), we get

$$V_{DA} = \left\langle a; \{Q\} \middle| H^{(1)} \middle| d; \{Q\} \right\rangle \langle \nu_a | \nu_d \rangle, \tag{2.38}$$

leading to the definition of the electronic matrix element,

$$t_{DA} = \left\langle a; \{Q\} \middle| H^{(1)} \middle| d; \{Q\} \right\rangle. \tag{2.39}$$

For a unimolecular transition, the FGR transition rate can then be written as follows:[4]

$$\begin{aligned} k_{DA} &= \frac{2\pi}{\hbar} \sum_{\nu_d, \nu_a} f(E_{\nu_d}) |V_{DA}|^2 \delta(E_{\nu_d} - E_{\nu_a}) \\ &= \frac{2\pi |t_{DA}|^2}{\hbar} \sum_{\nu_d, \nu_a} f(E_{\nu_d}) F_{ad} \delta(E_{\nu_d} - E_{\nu_a}) \end{aligned} \tag{2.40}$$

where $f(E_{\nu_d})$ is the Bose distribution function of the relevant vibrational levels, and $F_{ad} = \langle \nu_a | \nu_d \rangle^2$ is the Franck-Condon factor.

In the classical, high temperature limit (where $k_B T \gg \hbar\omega_n$ for all normal modes n), the transfer process is an activated process, with a barrier defined by the diabatic energy curves in Fig. 2.8. The transition rate is then given as[4]

$$k_{DA} = \frac{2\pi |t_{DA}|^2}{\hbar} \int f(Q) \delta(E_D(Q) - E_A(Q)) \, \mathrm{d}Q, \tag{2.41}$$

where t_{DA} is the transfer integral connecting the donor and acceptor states, $E_D(Q)$ and $E_A(Q)$ are the diabatic energy surfaces corresponding to the states, and $f(Q)$ is the Boltzmann distribution function,

$$f(Q) = \sqrt{\frac{M\omega^2}{2\pi k_B T}} \exp\left(-\frac{E_D(Q)}{k_B T}\right), \tag{2.42}$$

which ensures the ensemble average over initial configurations of the donor.[4] Evaluating the integral gives

$$k_{DA} = |t_{DA}|^2 \sqrt{\frac{\pi}{\hbar^2 k_B T E_\lambda}} \exp\left(-\frac{E_{\text{act}}}{k_B T}\right), \tag{2.43}$$

with E_{act} being the activation energy, and E_λ the reorganisation energy. The activation energy, defined in Fig. 2.8, can be expressed in terms of the net energy difference of the process, ΔE, and the reorganisation energy, E_λ. The latter is a crucial element of Marcus theory. It represents the energy difference that needs to be dissipated after a vertical (no change in Q) transition from the donor to the acceptor state.[34]

$$E_{\text{act}} = \frac{(\Delta E - E_\lambda)^2}{4E_\lambda} \tag{2.44}$$

The rate expression can therefore be rewritten in its final form as[151]

$$k_{DA} = |t_{DA}|^2 \sqrt{\frac{\pi}{\hbar^2 k_B T E_\lambda}} \exp\left(-\frac{(\Delta E - E_\lambda)^2}{4 k_B T E_\lambda}\right). \tag{2.45}$$

This form of the rate expression notably highlights the three distinct regimes arising in Marcus theory as a function of the relative magnitudes of the driving force, ΔE, and the reorganisation energy, E_λ. The different regimes are illustrated in Fig. 2.9. In the *'normal' regime*, where $E_\lambda < \Delta E$, increasing the driving force increases the rate of transition, until a maximum is reached, the *'activationless' limit*, where $E_\lambda = \Delta E$. Upon further increasing the driving force, we enter the

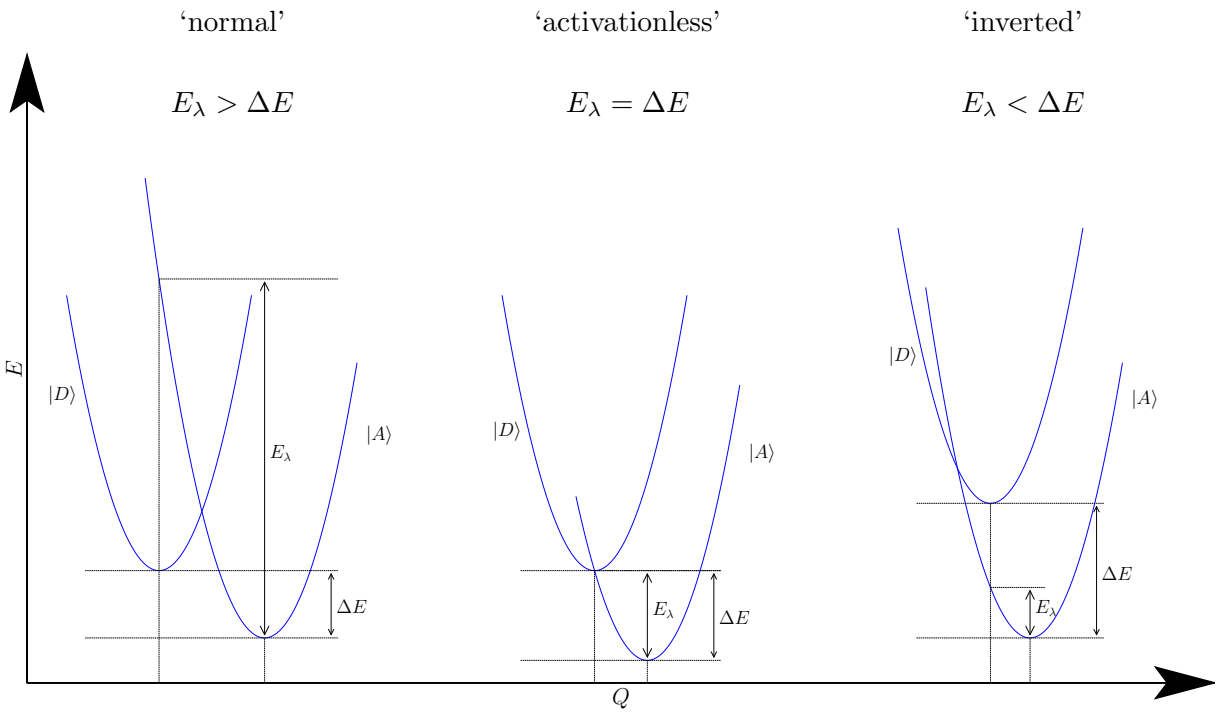


Figure 2.9: Different regimes in Marcus theory. Both the normal and inverted regimes exhibit lower transition rates than the activationless process. Figure reproduced from Ref. [4].

'inverted' regime, where transition rates decrease again, due to the large degree of reorganisation required for these reactions to proceed, leading to reduced rates of transition despite the overall reaction being hugely favourable energetically. While the existence of an inverted regime has been shown experimentally,[154–157] the level of reduction in transition rate is often overstated by Marcus theory. In this regime, nuclear quantum mechanical effects (e.g., through tunnelling) can significantly increase the transition rates,[158] and more sophisticated theoretical models can account for such effects.[159]

Finally, the transition rates for bimolecular (or inter-chain) transfer differs from the ones presented above due to the fact that there are two independent sets of coordinates, Q_D and Q_A, for the different molecules involved. The charge transfer takes place between an initially charged donor state, $|D^-\rangle$, and neutral acceptor

state, $|A\rangle$, to result in final states $|D\rangle$ and $|A^-\rangle$, respectively. The net energy change and associated reorganisation energies are denoted ΔE_D^0, E_λ^D, and ΔE_A^0, E_λ^A, on the donor and acceptor molecules, respectively. In the high temperature limit (which is used in the work presented in Chapter 4), rate expression in this case takes the form[4]

$$k_{DA} = \frac{2\pi|t_{DA}|^2}{\hbar}\int f(Q_D)f(Q_A) \times \delta((E_{D^-}(Q_D) + E_A(Q_A)) - (E_D(Q_D) + E_{A^-}(Q_A)))\,\mathrm{d}Q_D\,\mathrm{d}Q_A, \tag{2.46}$$

where $f(Q_X)$ is once again the classical Boltzmann distribution shown in Eq. (2.42). This expression can be rewritten as

$$k_{DA} = 2\pi|t_{DA}|^2\int D(\omega)A(\omega)\,\mathrm{d}\omega, \tag{2.47}$$

where $D(\omega)$ and $A(\omega)$ are spectral functions of the donor and acceptor states, defined as

$$\begin{aligned} D(\omega) &= \int f(Q_D)\delta(E_{D^-}(Q_D) - E_D(Q_D) - \hbar\omega)\,\mathrm{d}Q_D \\ &= \sqrt{\frac{\pi}{\hbar^2 k_B T E_\lambda^D}}\exp\left(-\frac{(\Delta E_D - E_\lambda^D)^2}{4k_B T E_\lambda^D}\right) \end{aligned} \tag{2.48}$$

and

$$\begin{aligned} A(\omega) &= \int f(Q_A)\delta(E_A(Q_A) - E_{A^-}(Q_A) - \hbar\omega)\,\mathrm{d}Q_A \\ &= \sqrt{\frac{\pi}{\hbar^2 k_B T E_\lambda^A}}\exp\left(-\frac{(\Delta E_A - E_\lambda^A)^2}{4k_B T E_\lambda^A}\right), \end{aligned} \tag{2.49}$$

where $\Delta E_D = \Delta E_D^{(0)} - \hbar\omega$ and $\Delta E_A = \Delta E_A^{(0)} + \hbar\omega$.

2.3 Ehrenfest Dynamics

Achieving accurate description of quantum dynamics in conjugated polymer systems is challenging task. In the following section, a mixed quantum-classical methodology is described that was used for the work presented in Chapter 5. This approximate

approach was necessary as a full quantum treatment of all degrees of freedom on the desired system size and time scale is not feasible due to the exponentially growing size of the Hilbert space describing the systems.

The relations obtained from Ehrenfest's theorem give the time evolution relations that can be implemented in the mixed quantum-classical model called time-dependent self-consistent field approach, also often simply referred to as the Ehrenfest method.[160–163] The method involves a quantum subsystem that is subject to evolution based on the time-dependent Schrödinger equation (TDSE), with the Hamiltonian depending on the mean-field values of classical variables. Simultaneously, the classical degrees of freedom are evolving as per their classical equations of motion, with forces derived from the quantum observables.[164] This classical evolution relies on Ehrenfest's theorem, which makes use of the fact that the evolution of the average values of quantum variables follows the classical equations of motions.[165]

The approach is demonstrated below using a simple model system. Consider a Hamiltonian of two interacting subsystems, denoted 1 and 2, with corresponding coordinates and masses, R_1, R_2 and M_1, M_2, respectively. Their general Hamiltonian can be written as[34]

$$\hat{H} = \hat{H}_1 + \hat{H}_2 + \hat{V}_{12}(\hat{R}_1, \hat{R}_2) \tag{2.50}$$

$$\hat{H}_k = -\frac{\hbar^2}{2M_k}\nabla_k^2 + \hat{V}_k(\hat{R}_k), \tag{2.51}$$

where $\hat{H}_k$ denote the Hamiltonians for the individual subsystems, and $\hat{R}_k$ are explicitly stated as operators to distinguish between the quantum and classical treatments of the systems. Assuming that the solution of TDSE for the system can be written as a product wavefunction of the two subsystems,

$$\Psi(t) = \psi_1(t)\psi_2(t), \tag{2.52}$$

where $\psi_k(t)$ each satisfy the TDSE as

$$\mathrm{i}\hbar\frac{\partial\,\psi_k}{\partial\,t} = \hat{H}_k\psi_k. \tag{2.53}$$

The TDSE for the overall system is then written as[34]

$$\mathrm{i}\hbar\left(\psi_2\frac{\partial\,\psi_1}{\partial\,t} + \psi_1\frac{\partial\,\psi_2}{\partial\,t}\right) = \psi_2\hat{H}_1\psi_1 + \psi_1\hat{H}_2\psi_2 + \hat{V}_{12}\psi_1\psi_2. \tag{2.54}$$

Left-multiplying by ψ_2^* and integrating over the coordinates of subsystem 2, we get

$$\mathrm{i}\hbar\left(\frac{\partial\,\psi_1}{\partial\,t} + \psi_1\left\langle\psi_2\middle|\frac{\partial\,\psi_2}{\partial\,t}\right\rangle_2\right) = \hat{H}_1\psi_1 + \psi_1\left\langle\psi_2\middle|\hat{H}_2\middle|\psi_2\right\rangle_2 + \left\langle\psi_2\middle|\hat{V}_{12}\middle|\psi_2\right\rangle_2\psi_1, \tag{2.55}$$

which can be simplified using Eq. (2.53) to give

$$\mathrm{i}\hbar\frac{\partial\,\psi_1}{\partial\,t} = \left(-\frac{\hbar^2}{2M_1}\nabla_1^2 + \hat{V}_{1,\mathrm{eff}}(\hat{R}_1)\right)\psi_1, \tag{2.56}$$

where

$$\hat{V}_{1,\mathrm{eff}}(\hat{R}_1) = \hat{V}_1(\hat{R}_1) + \left\langle\psi_2\middle|\hat{V}_{12}\middle|\psi_2\right\rangle_2. \tag{2.57}$$

The equivalent formulae for subsystem 2 also hold. The 'trick' of the Ehrenfest method comes in the form of replacing one of the subsystems (in this case, subsystem 2) with its classical counterpart, leading to the evolution of subsystem 2 as[34, 165]

$$\ddot{R}_2 = -\frac{1}{M_2}\nabla V_{2,\mathrm{eff}}(R_2), \tag{2.58}$$

where $R_2(t)$ is now a classical variable. This leads to $\langle\psi_2|\hat{V}_{12}|\psi_2\rangle_2$ being replaced by $\hat{V}_{12}(\hat{R}_1; R_2(t))$. Equation (2.56) therefore becomes[34]

$$\mathrm{i}\hbar\frac{\partial\,\psi_1}{\partial\,t} = \left(-\frac{\hbar^2}{2M_1}\nabla_1^2 + \hat{V}_{1,\mathrm{eff}}(\hat{R}_1; R_2(t))\right)\psi_1, \tag{2.59}$$

where

$$\hat{V}_{1,\mathrm{eff}}(\hat{R}_1) = \hat{V}_1(\hat{R}_1) + \hat{V}_{12}(\hat{R}_1; R_2(t)). \tag{2.60}$$

Equations (2.58) to (2.60) together give the time-dependent self-consistent field or Ehrenfest evolution scheme.[160–163]

Ehrenfest dynamics has its limitations. The formulation of the scheme means that while the interactions link the quantum and classical subsystems, each influencing the evolution of the other, as described above, there are significant errors introduced in the process. As the classical particles are governed by forces derived from the average distribution of the quantum particles,[166] the classical behaviour can deviate significantly from the realistic behaviour if multiple adiabatic states are populated, as the classical motion follows the average potential energy surface.[167, 168] The averaging also leads to a reduction in the amount of energy that can be transferred from the quantum to the classical subsystem, causing a violation of detailed balance. This can be illustrated by considering the average change in the energy (power) of a nucleus:[166]

$$\langle \dot{E}_{\mathrm{nuc}} \rangle_{\Delta t} = \frac{1}{\Delta t} \int_{t_0}^{t_0+\Delta t} \mathbf{X} \cdot \mathbf{f}(t)\, \mathrm{d}t, \tag{2.61}$$

where $\mathbf{X}$ and $\mathbf{f}(t)$ contribute to the force experienced by the nucleus from the electrons as $\mathbf{F} = -k\mathbf{X} + \mathbf{f}(t)$, representing the harmonic and non-adiabatic elements of the total force, respectively. When $\mathbf{X}$ depends on $\mathbf{f}(t)$ through the equations of motion, the correlation between them will lead to power being generated in Eq. (2.61) by the fluctuation-dissipation theorem.[169] However, the averaging of multiple electronic states within the Ehrenfest scheme breaks the exact correlation between the force and momentum, and reduces the amount of energy transferred to the nucleus.[166] This ultimately leads to the heating of the system as time progresses when a finite temperature classical subsystem is used, resulting in incorrect long term population equilibrium.[170] Despite the limitations discussed, Ehrenfest dynamics is a computationally efficient and effective method that can provide insights into

non-adiabatic processes,[171] and can be applied to certain problems successfully, including those relating to conjugated polymer systems.[166, 172–174]

2.4 Langevin Dynamics

Realistic molecular systems possess inherent randomness. Molecules in solution are a prime example where constant interactions with the surroundings through a series of collision events can continuously randomise and redistribute the energy in a system, while maintaining an overall thermal equilibrium. The Langevin equation describes such a system, interacting with its environment (a 'bath'), and through this interaction reaching thermal equilibrium with the surroundings. The form of the equation is motivated through building up a model from a simple starting point with physically relevant arguments.[34] The derivation will also be limited to a one-dimensional system for simplicity and due to its relevance for this thesis. A particle subjected to a potential, $V(x)$, follows the equation of motion

$$\ddot{x} = -\frac{1}{m}\frac{\partial V(x)}{\partial x}. \tag{2.62}$$

To model the interaction with its environment, we first apply a friction force, which slows down the particle, and thereby models energy loss from the particle to its environment. A natural choice is to take this friction force as being proportional to the particle's velocity, giving

$$\ddot{x} = -\frac{1}{m}\frac{\partial V(x)}{\partial x} - \gamma\dot{x}, \tag{2.63}$$

where γ is the proportionality constant, called the *friction coefficient*. Without any additional terms the system would lose energy over time due to this friction term. In order to describe a system in thermal equilibrium, this energy loss needs to be recovered by the system. This is done in the form of a random force, $R(t)$, which

can be thought of as mimicking random molecular collisions with the environment. The addition of this random force term gives the general form of the Langevin equation in one dimension, which now reads[175, 176]

$$\ddot{x} = -\frac{1}{m}\frac{\partial V(x)}{\partial x} - \gamma\dot{x} + \frac{1}{m}R(t). \tag{2.64}$$

The nature of this random force, $R(t)$, can be reasoned as follows. Describing thermal equilibrium, a stationary process, $\langle R(t)\rangle = 0$ must hold for symmetry reasons. Given that Eq. (2.63) describes a system relaxing at $T = 0$, the random force must be a function of the temperature of the environment. Additionally, Eq. (2.63) also shows a Markovian process, so if the damping is of a Markovian nature, the random force must also mirror this and be independent of the history of the system. Finally, as the force is meant to encapsulate a range of contributions from the environment, it is reasonable to assume that it can be modelled as a Gaussian random variable.[34] A Markovian process requires that the relaxation timescale of the environment is significantly faster than the system's, but for the stochastic force to affect the system, this timescale needs to be finite. If we assume that the force $R(t)$ is constant within a time interval $[t, t + \tau_R]$, where τ_R denotes the relaxation time of the bath, instances of the force that are more than $\tau_R/2$ apart in time can be treated as independent Gaussian random variables.[34] Therefore

$$\langle R(t_1)R(t_1 + t)\rangle = \mathcal{C}g(t), \tag{2.65}$$

where $\mathcal{C}$ is a constant and

$$g(t) = \begin{cases} 1 & \text{if} \quad |t| < \tau_R/2 \\ 0 & \text{otherwise} \end{cases} \tag{2.66}$$

as above. As the friction force and the stochastic force acting together keep the system in thermal equilibrium, γ and $\mathcal{C}$ are clearly linked. This link is provided by

the fluctuation-dissipation theorem,[177, 178] leading to the correlation function

$$C_R(t) \equiv \langle R(t_1)R(t_1+t)\rangle = 2m\gamma k_B T\delta(t), \tag{2.67}$$

where the quantities take their usual physical meaning. The link to the friction coefficient, γ, ensures that at long times thermal equilibrium is reached. Given the time correlation function of the stochastic force, by the Wiener-Khintchine theorem, its power spectrum is given as the Fourier transform of the time correlation function.[34]

$$S_R(\omega) = \frac{1}{2\pi}\int_{-\infty}^{\infty} \exp\left(-\mathrm{i}\omega t\right) C_R(t)\,\mathrm{d}t = \frac{m\gamma k_B T}{\pi} = \text{constant} \equiv S_R \tag{2.68}$$

Notably, the power spectrum being constant means that all frequencies contribute equally to the force spectrum. Such random processes are referred to as white noise. Using this power spectrum of R, observables of the Langevin equation can be calculated. Specifically, for a harmonic potential, $V(x) = \frac{1}{2}m\omega_0^2 x^2$, the position time correlation function can be calculated as[34]

$$\begin{aligned} C_x(t) &= \frac{\pi S_R}{m^2\gamma\omega_0^2}\left(\cos\left(\omega_1 t\right) + \frac{\gamma}{2\omega_1}\sin\left(\omega_1 t\right)\right)\exp\left(-\frac{\gamma t}{2}\right) \\ &= \frac{k_B T}{m\omega_0^2}\left(\cos\left(\omega_1 t\right) + \frac{\gamma}{2\omega_1}\sin\left(\omega_1 t\right)\right)\exp\left(-\frac{\gamma t}{2}\right), \end{aligned} \tag{2.69}$$

where $\omega_1 = \sqrt{\omega_0^2 - \gamma^2/4}$.

In the work presented in Chapter 5, Brownian forces are applied to the rotational degrees of freedom in the system. The relations listed in Table 2.1 show the linear-rotational equivalency of physical quantities, and allow us to recast the Langevin equation in terms of rotational variables as

$$I\frac{\mathrm{d}\Omega_n(t)}{\mathrm{d}t} = I\frac{\mathrm{d}^2\phi_n}{\mathrm{d}t^2} = -I\gamma\Omega_n(t) + \Gamma_n^{\mathrm{syst}}(t) + R_n(t), \tag{2.70}$$

where the random force now fulfils the relation

$$\langle R(t_1)R(t_1+t)\rangle = 2I\gamma k_B T\delta(t). \tag{2.71}$$

Table 2.1: The equivalence of rotational and linear variables for the Langevin equation.

Angular		**Linear**	
Angular displacement	ϕ	Linear displacement	x
Angular velocity	Ω	Linear velocity	v
Angular momentum	L	Linear momentum	p
Torque	$\Gamma = -\partial\langle\hat{H}\rangle/\partial\Delta\phi$	Force	$F = -\partial\langle\hat{H}\rangle/\partial x$
Inertia	I	Mass	m
Force constant	K (energy rad^{-2})	Force constant	K (energy length^{-2})

3
Computational Methods

A general theme throughout this thesis is examining propagation of charge in conjugated systems. This necessitates time evolution of system variables – position of charge, evolution of wavefunctions and classical variables alike. This chapter summarises the computational techniques that this time evolution involves in the different systems under consideration. Firstly, in the bulk polymer model presented in Chapter 4, the kinetic Monte Carlo method is used to simulate the stochastic propagation of electric charge throughout the bulk system.

The model discussed in Chapter 5 requires the quantum mechanical time evolution of the polaron wavefunction. A well-established method for low-dimensional systems is within the formalism of matrix product states, with time evolution performed according to the time-evolving block decimation algorithm.[179, 180] The use of this powerful computational machinery presented below is motivated by the desire for adding quantum mechanical accuracy to degrees of freedom beyond the charge wavefunction, i.e., to move beyond purely Ehrenfest models. The presented tensor network methods were utilised as implemented in the TNT library,[181, 182] a computer package designed to simulate one-dimensional quantum systems using the matrix product state formalism.

Finally, the evolution of classical rotational motion coupled to the quantum mechanical evolution is solved by a numerical integration algorithm of the Langevin equation.[183]

3.1 Kinetic Monte Carlo

Kinetic Monte Carlo (kMC) algorithms have a long history of simulating time-dependent processes in materials science.[184] In the context of charge carrier simulation, the method stretches back to the works of Silver[185, 186], and, notably, Bässler's influential studies,[78, 187] and it continues to be an increasingly widely employed method.[188]

The kinetic Monte Carlo (kMC) approach models subsequent stochastic events to build an image of time evolution within the studied system. In the context of the hopping transport problem, given a particular starting (donor) state, D, and a number of potential final (acceptor) states, A_i, one can define transition rates, $k_{D\to A_i}$, between these states, for all possible starting states. The algorithm then proceeds as follows:[78]

Step (1) Using a randomly generated number, find the acceptor state, where the transition probability to a particular potential acceptor state is defined as

$$P_{D\to A_k} = \frac{k_{D\to A_k}}{\sum\limits_i k_{D\to A_i}}. \tag{3.1}$$

Step (2) Update the relevant observables (e.g., displacement of charge) using the new state.

Step (3) The currently occupied state becomes the new donor state. Before the following stochastic event, a 'dwelling' time is calculated, which serves

as the basis of the accumulating simulation time. This time is calculated from an exponential random distribution with mean dwelling time

$$\langle t_{\mathrm{dwell},D} \rangle = \frac{1}{\sum_i k_{D \to A_i}}, \tag{3.2}$$

where D now denotes the new donor state.

Step (4) Repeat Steps (1)–(3) until the desired total simulation time is achieved.

Given the stochastic nature of the simulation process, ensemble averages over multiple trajectories must be calculated.

3.2 Matrix Product States and Time-Evolving Block Decimation

3.2.1 Matrix Product States

The general representation of a one-dimensional quantum system of L sites, can be written as[189]

$$|\psi\rangle = \sum_{\sigma_1,\ldots,\sigma_L} C_{\sigma_1,\ldots,\sigma_L} |\sigma_1,\ldots,\sigma_L\rangle, \tag{3.3}$$

where $C_{\sigma_1,\ldots,\sigma_L}$ is the probability amplitude tensor. The physical indices, $\{\sigma_i\}$, represent the d-dimensional local space of each site $1,\ldots,L$. The size of the probability amplitude tensor is then d^L.

Through a series of singular value decompositions (SVDs), the probability amplitude tensor may be broken down into matrices of smaller dimensionality. Singular value decomposition is defined as follows. For any matrix, $M^{m\times n}$, there exists a decomposition[189]

$$M = USV^\dagger, \tag{3.4}$$

where

- U, made up of orthonormal columns (left singular vectors), is a $m \times \min(m,n)$ matrix. $U^\dagger U = \mathbb{1}$ (if $m \leq n$, then U is unitary, and $UU^\dagger = \mathbb{1}$).
- S is the $\min(m,n) \times \min(m,n)$ diagonal matrix of non-negative *singular values*. The number of non-zero singular values is the (Schmidt) rank of the matrix M.
- V, made up of orthonormal rows (right singular vectors), is a $\min(m,n) \times n$ matrix. $VV^\dagger = \mathbb{1}$ (if $n \leq m$, then V is unitary, and $V^\dagger V = \mathbb{1}$).

Therefore, the representation in Eq. (3.3) can be rewritten as a series of matrix products, giving the matrix product state formalism, as[189]

$$|\psi\rangle = \sum_{\sigma_1,\ldots,\sigma_L} \sum_{\alpha_1,\ldots,\alpha_L} M^{\sigma_1}_{1,\alpha_1} M^{\sigma_2}_{\alpha_1,\alpha_2} \cdots M^{\sigma_{L-1}}_{\alpha_{L-2},\alpha_{L-1}} M^{\sigma_L}_{\alpha_{L-1},1} |\sigma_1,\ldots,\sigma_L\rangle, \tag{3.5}$$

where M^{σ_i} are a set of d matrices on site i, corresponding to the local states. α_i are called the internal indices.

Canonical Forms of MPSs

Matrix product state representations of a given quantum state are not unique, as can be easily demonstrated starting from Eq. (3.5). Inserting $I = XX^{-1}$ between any $M^{\sigma_i} M^{\sigma_{i+1}}$ pair, where X is an invertible matrix, the local matrices can be rewritten as $\tilde{M}^{\sigma_i} = M^{\sigma_i} X$ and $\tilde{M}^{\sigma_{i+1}} = X^{-1} M^{\sigma_{i+1}}$, without changing the quantum state, $|\psi\rangle$, and still adhering to the matrix product formalism.[190] Such insertions can generate special, canonical forms of matrix product states. The representation

$$|\psi\rangle = \sum_{\sigma_1,\ldots,\sigma_L} \sum_{\alpha_1,\ldots,\alpha_L} A^{\sigma_1}_{1,\alpha_1} A^{\sigma_2}_{\alpha_1,\alpha_2} \cdots A^{\sigma_{L-1}}_{\alpha_{L-2},\alpha_{L-1}} A^{\sigma_L}_{\alpha_{L-1},1} |\sigma_1,\ldots,\sigma_L\rangle \tag{3.6}$$

is called the *left canonical* form, where all local matrices, A^{σ_i}, are left-normalised, such that $\sum_{\sigma_i} A^{\sigma_i \dagger} A^{\sigma_i} = I$. Similarly, the representation

$$|\psi\rangle = \sum_{\sigma_1,\ldots,\sigma_L} \sum_{\alpha_1,\ldots,\alpha_L} B^{\sigma_1}_{1,\alpha_1} B^{\sigma_2}_{\alpha_1,\alpha_2} \cdots B^{\sigma_{L-1}}_{\alpha_{L-2},\alpha_{L-1}} B^{\sigma_L}_{\alpha_{L-1},1} |\sigma_1,\ldots,\sigma_L\rangle \tag{3.7}$$

is called *right-canonical*, as it is constructed from right-normalised matrices B^{σ_i}, such that $\sum_{\sigma_i} B^{\sigma_i} B^{\sigma_i\dagger} = I$. Finally, the *mixed-canonical* form,

$$|\psi\rangle = \sum_{\sigma_1,\ldots,\sigma_L} \sum_{\alpha_1,\ldots,\alpha_L} A^{\sigma_1}_{1,\alpha_1} \cdots A^{\sigma_{m-2}}_{\alpha_{m-2},\alpha_{m-1}} M^{\sigma_m}_{\alpha_{m-1},\alpha_m} B^{\sigma_{m+1}}_{\alpha_m,\alpha_{m+1}} \cdots B^{\sigma_L}_{\alpha_{L-1},1} |\sigma_1,\ldots,\sigma_L\rangle, \tag{3.8}$$

where $M^{\sigma_m}_{\alpha_{m-1},\alpha_m}$ is the orthogonality centre of the MPS, and allows for efficient calculation of expectation values at the orthogonality centre.

The internal indices, α_m, have dimensions χ_m. The MPS form of a quantum state is exact when[190]

$$\chi_m = \begin{cases} d^m & \text{for} \quad m < L/2 \\ d^{L-m} & \text{for} \quad m \geq L/2. \end{cases} \tag{3.9}$$

Physically, χ_m is related to the entanglement entropy across 'bond' m between a bipartite system, i.e.,[191]

$$S(\rho_A, m) = -\operatorname{Tr}\left[\rho_{A,m} \log\left(\rho_{A,m}\right)\right] = S(\rho_B, m), \tag{3.10}$$

where A and B are the two subsystems. Consequently, the maximum possible entanglement entropy across 'bond' m is[179]

$$S_{\max}(\rho_A, m) = \log\left(\chi_m\right). \tag{3.11}$$

Dimensionality Truncation

So far, nothing presented reduces the overall size of the Hilbert space considered, so large systems are prohibitively expensive. For minimally entangled systems, MPS representation can be efficient. Starting from the mixed canonical form in Eq. (3.8), performing the contraction

$$D^{\sigma_m,\sigma_{m+1}}_{\alpha_{m-1},\alpha_{m+1}} = \sum_{\alpha_m} M^{\sigma_m}_{\alpha_{m-1},\alpha_m} B^{\sigma_{m+1}}_{\alpha_m,\alpha_{m+1}} \tag{3.12}$$

we get

$$|\psi\rangle = \sum_{\sigma_1,\ldots,\sigma_L} \sum_{\alpha_1,\ldots,\alpha_{m-1}} \sum_{\alpha_{m+1},\ldots,\alpha_L} A^{\sigma_1}_{1,\alpha_1} \cdots D^{\sigma_m,\sigma_{m+1}}_{\alpha_{m-1},\alpha_{m+1}} \cdots B^{\sigma_L}_{\alpha_{L-1},1} |\sigma_1,\ldots,\sigma_L\rangle. \quad (3.13)$$

A singular value decomposition,

$$D^{\sigma_m,\sigma_{m+1}}_{\alpha_{m-1},\alpha_{m+1}} = \sum_{\alpha_m} A^{\sigma_m}_{\alpha_{m-1},\alpha_m} S_{\alpha_m,\alpha_m} B^{\sigma_{m+1}}_{\alpha_m,\alpha_{m+1}}, \quad (3.14)$$

leads to the Schmidt decomposed form of the state:

$$|\psi\rangle = \sum_{\alpha_m} S_{\alpha_m} |\alpha_m\rangle_A |\alpha_m\rangle_B, \quad (3.15)$$

where

$$|\alpha_m\rangle_A = \sum_{\sigma_1,\ldots,\sigma_m} \sum_{\alpha_1,\ldots,\alpha_{m-1}} A^{\sigma_1}_{1,\alpha_1} \cdots A^{\sigma_m}_{\alpha_{m-1},\alpha_m} |\sigma_1,\ldots,\sigma_m\rangle \quad (3.16)$$

and similarly for $|\alpha_m\rangle_B$. These correspond to the subsystems of sites 1 through m, and $m+1$ through L, respectively. To reduce the size of the overall Hilbert space, only the largest singular values are retained. Truncation can be performed by limiting the maximum number of singular values retained, enforcing a cutoff threshold for the ratio $S_{\alpha_m}/S_{\max}$, or both.

Operators in MPS

The orthonormality relations described above mean that careful selection of the orthonormality centre in the mixed canonical forms allows for efficient evaluation of observables. Notably, evaluating a single-site observable on site m, using the mixed-canonical form shown in Eq. (3.8) reduces to:

$$\langle\psi|\hat{O}_m|\psi\rangle = \sum_{\sigma_m,\sigma'_m} \sum_{\alpha_{m-1},\alpha_m} \langle\sigma'_m|\hat{O}_m|\sigma_m\rangle M^{\sigma_m\dagger}_{\alpha_m,\alpha_{m-1}} M^{\sigma'_m}_{\alpha_{m-1},\alpha_m} \quad (3.17)$$

This requires four contractions, regardless of the total system size.

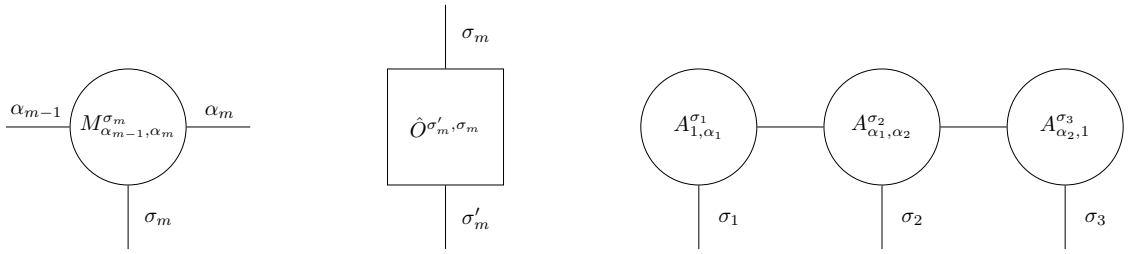


Figure 3.1: Tensor diagrams representing (from left to right): an individual site, a single-site operator, and an MPS consisting of three sites in a left-canonical form.

Tensor Diagrams

Tensor networks quickly become cumbersome algebraically and are often described in diagrammatic terms to visually demonstrate network structures and computational algorithms. Examples of such diagrams are shown in Fig. 3.1. In general, vertical lines represent physical indices and horizontal lines correspond to internal indices. Connected lines indicate that summation is performed over the indices in question.[192]

3.2.2 Time-Evolving Block Decimation

The time-dependent Schrödinger equation is solved via

$$|\Psi_{\mathrm{MPS}}(t+\delta t)\rangle = \exp\left(-\mathrm{i}\hat{H}\delta t/\hbar\right)|\Psi_{\mathrm{MPS}}(t)\rangle \tag{3.18}$$

Noting that for a Hamiltonian consisting of only on-site and nearest-neighbour terms, it can be rewritten as:

$$\hat{H} = \sum_{n=1}^{L-1} \hat{H}_{n,n+1} \tag{3.19}$$

While the terms $\hat{H}_{n,n+1}$ generally do not commute, utilising (second-order) Suzuki-Trotter decomposition, the time evolution propagator in Eq. (3.18) can be written as[193–195]

$$\mathrm{e}^{-\mathrm{i}\hat{H}\delta t/\hbar} \approx \mathrm{e}^{-\mathrm{i}\hat{H}_{1,2}\delta t/2\hbar}\mathrm{e}^{-\mathrm{i}\hat{H}_{2,3}\delta t/2\hbar}\cdots\mathrm{e}^{-\mathrm{i}\hat{H}_{2,3}\delta t/2\hbar}\mathrm{e}^{-\mathrm{i}\hat{H}_{1,2}\delta t/2\hbar} + \mathcal{O}(\delta t^3). \tag{3.20}$$

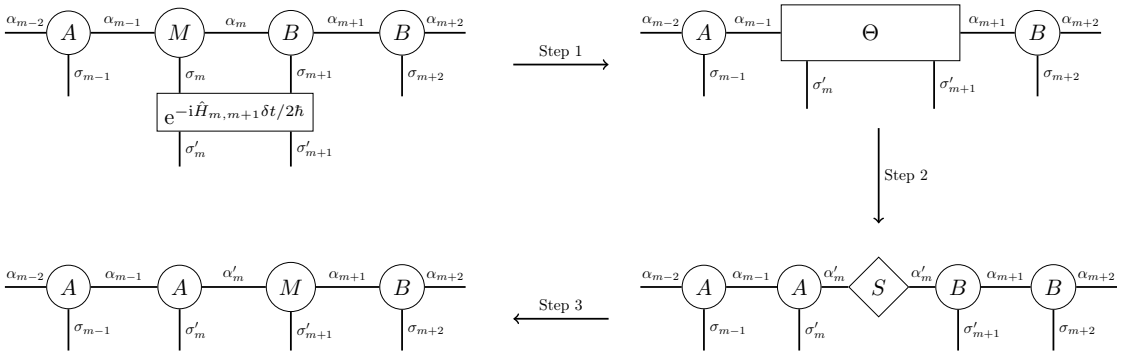


Figure 3.2: Diagrammatic representation of the TEBD algorithm steps. Image reproduced from Ref. [108]. The three steps indicated together represent one half time step evolution of sites m and $m+1$.

This decomposition gives the basis of the TEBD scheme, as applying the time propagators as local, 2-site operators can be implemented efficiently in the context of matrix product states. The algorithm proceeds as follows:[108, 179, 180]

Step (1): The 2-site time evolution propagator is applied to orthogonality centre, m, and its neighbouring site, $m+1$. Contractions along the indices α_m, σ_m, σ_{m+1} are calculated.

Step (2): The resulting 2-site block, Θ, is decomposed using SVD, and dimensionality truncation according to the calculation parameters is completed.

Step (3): The resulting singular value matrix, S, is absorbed into the site $m+1$, thereby completing the time propagation step and moving the orthogonality centre one site along the chain.

The steps described above are repeated in a left-to-right and then a backwards, right-to-left sweep of the whole chain to complete one full time evolution step as stated in Eq. (3.18). The algorithm outlined above is illustrated in Fig. 3.2, while the complete time-evolution 'staircase' is presented in Fig. 3.3.

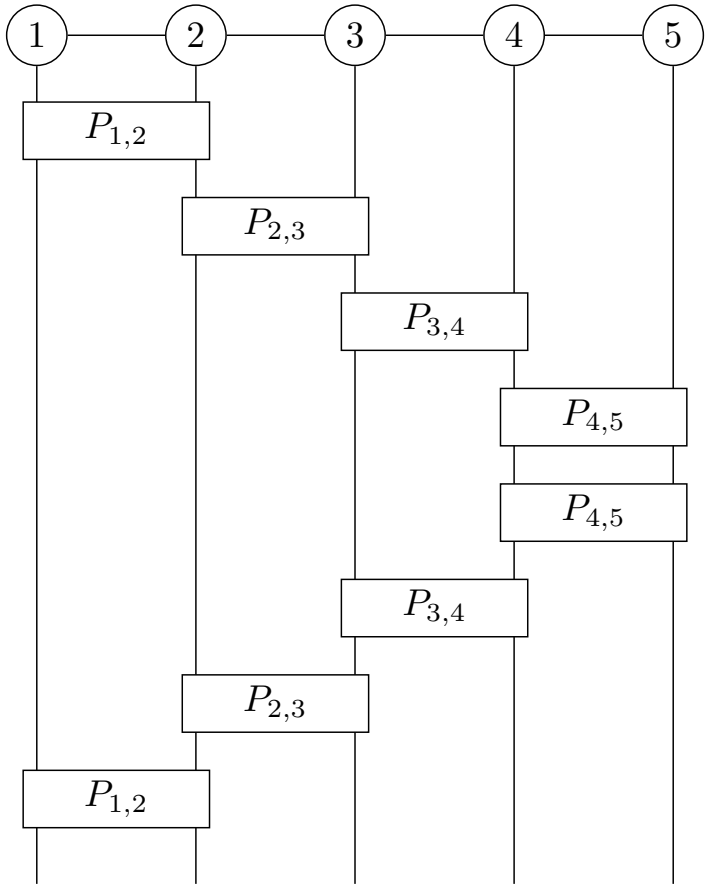


Figure 3.3: Time evolution staircase applied to a 5-site, open boundary system. The circles represent the sites of the system, and $P_{i,i+1}$ are the 2-site time propagators. The application of each propagator is performed as illustrated in Fig. 3.2.

3.2.3 Periodic Boundary Conditions

The standard routines in the TNT library do not offer algorithms for the treatment of periodic systems. Such functionality is desired to reduce finite size effects of 1D systems, as well as for modelling other systems of interest such as macrocycles. The implementation of such functionality within the MPS/TEBD formalism is complicated due to interactions being applied between neighbouring sites in the system, as shown previously. Applying time evolution within the TEBD scheme[179, 180] requires that end sites of the modelled system are brought together in space. This can be achieved using so-called 'swap gates' between neighbouring in a sequence

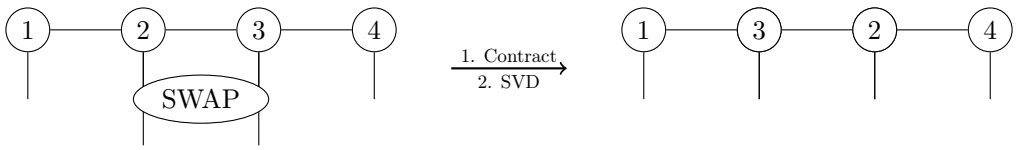


Figure 3.4: Swap gate applied to neighbouring sites, 2 and 3, interchanges their physical indices.

until the end sites are located next to each other.[196] This operation is represented in Fig. 3.4. The 'swap gate' can be represented for two, d=2 sites as

$$\text{SWAP} = \begin{array}{c} \begin{matrix} |00\rangle & |01\rangle & |10\rangle & |11\rangle \end{matrix} \\ \begin{pmatrix} 1 & 0 & 0 & 0 \\ 0 & 0 & 1 & 0 \\ 0 & 1 & 0 & 0 \\ 0 & 0 & 0 & 1 \end{pmatrix} \end{array} \begin{matrix} |00\rangle \\ |01\rangle \\ |10\rangle \\ |11\rangle . \end{matrix} \tag{3.21}$$

With the use of such swap operations, a new time evolution staircase can be defined, which applies a time evolution step between the last and first sites of the chain. The overall time evolution in this modified scheme is defined by:

$$\begin{aligned} \mathrm{e}^{-\mathrm{i}\hat{H}\delta t/\hbar} \approx\, & \mathrm{e}^{-\mathrm{i}\hat{H}_{1,2}\delta t/2\hbar}\mathrm{e}^{-\mathrm{i}\hat{H}_{2,3}\delta t/2\hbar}\cdots\mathrm{e}^{-\mathrm{i}\hat{H}_{L-1,L}\delta t/2\hbar} \\ & \times \mathcal{X}_{L-1,L}\mathcal{X}_{L-2,L-1}\cdots\mathcal{X}_{1,2}\mathrm{e}^{-\mathrm{i}\hat{H}_{1,L}\delta t/2\hbar}\mathrm{e}^{-\mathrm{i}\hat{H}_{1,L}\delta t/2\hbar}\mathcal{X}_{1,2}\cdots\mathcal{X}_{L-1,L} \\ & \times \mathrm{e}^{-\mathrm{i}\hat{H}_{L-1,L}\delta t/2\hbar}\cdots\mathrm{e}^{-\mathrm{i}\hat{H}_{1,2}\delta t/2\hbar} + \mathcal{O}(\delta t^3), \end{aligned} \tag{3.22}$$

where $\mathcal{X}_{i,i+1}$ is the swap operator acting on neighbouring sites, i and $i+1$. This is shown diagrammatically in Fig. 3.5. When compared to the open boundary Trotter scheme, defined in Eq. (3.20), the procedure introduces a large number of additional contractions and SVD decompositions, and hence increases the computational cost over the open boundary implementation. The benchmarking of the algorithm is presented in Appendix B.

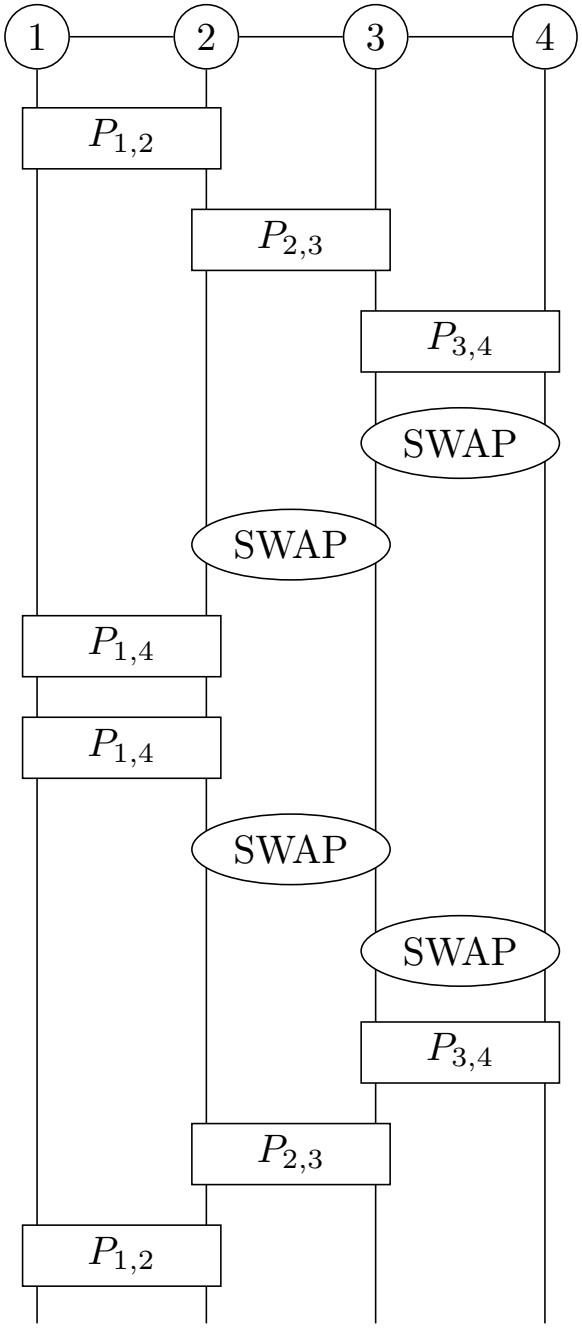


Figure 3.5: Time evolution staircase applied to a 4-site, periodic system. The circles represent the sites of the system, and $P_{i,i+1}$ are the 2-site time propagators. The SWAP gates interchange the physical indices of the two sites the act on, as shown in Fig. 3.4.

3.3 Langevin Algorithm

Solving the Langevin equation introduced in the previous chapter is achieved using a simple yet effective position-Verlet scheme, introduced by Grønbech-Jensen and Farago.[183] Given the Langevin equation for rotational variables, introduced in Eq. (2.70):

$$I\frac{\mathrm{d}^2\phi_n}{\mathrm{d}t^2} = -I\gamma\frac{\mathrm{d}\phi_n}{\mathrm{d}t} + \Gamma_n^{\mathrm{syst}}(t) + R_n(t), \tag{3.23}$$

the integration scheme reads

$$\phi_n(t+\Delta t) = 2b\phi_n(t) - a\phi_n(t-\Delta t) + \frac{b(\Delta t)^2}{I}\Gamma_n^{\mathrm{syst}}(t) + \frac{b\Delta t}{2I}\left(R^{t+\Delta t} + R^t\right), \tag{3.24}$$

where

$$a = \frac{1-\frac{\gamma\Delta t}{2}}{1+\frac{\gamma\Delta t}{2}} \tag{3.25}$$

$$b = \frac{1}{1+\frac{\gamma\Delta t}{2}}, \tag{3.26}$$

and the integrated stochastic force, defined as

$$R^t = \int_{t-\Delta t}^{t} R_n(t')\,\mathrm{d}t', \tag{3.27}$$

is a Gaussian random number with

$$\langle R^k\rangle = 0 \tag{3.28}$$

$$\langle R^k R^l\rangle = 2I\gamma k_B T\Delta t\delta_{k,l}. \tag{3.29}$$

An example calculation using the integration scheme is shown in Fig. 3.6, where a set of harmonic (rotational) oscillators were started in their equilibrium positions, subjected to evolution under the Langevin equation. The autocorrelation function of the angles, shown in Fig. 3.6, decays exponentially to settle into small fluctuations around zero at long times, in line with the analytic form of the autocorrelation presented in Eq. (2.69).

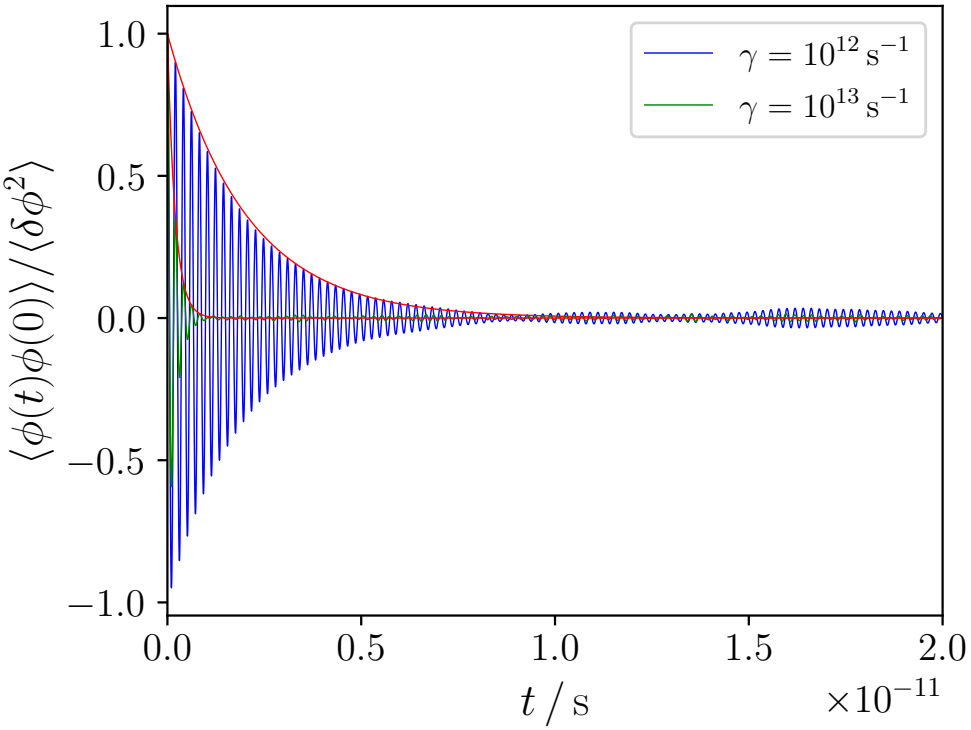


Figure 3.6: Autocorrelation function of the angular displacements at finite temperatures, with different values of friction coefficients. The oscillation frequency is determined by the of the underlying harmonic oscillator. Each decay is bound by red curve of $\exp(-\gamma t/2)$, as predicted by Eq. (2.69).[34]

4

Realistic Model of Bulk Charge Mobility

As discussed in Chapter 1, understanding charge mobility in organic semiconducting systems, especially π-conjugated polymer systems, has long been of keen interest in the scientific community. The modelling approach presented in this chapter builds on and extends a number of these different approaches, and most notably, develops a novel and atomistic description of charge mobility in bulk polymer systems. Conformationally static and on-site disorder leads to classes of Anderson localised and quasi-extended donor and acceptor states.[138, 139] The realistic treatment of disorder leads to an almost Gaussian distribution of states, providing a clear link to Bässler's GDM model. Inter-chain and intra-chain charge transfer are separately accounted for, using a bimolecular Marcus rate theory for the former. Intra-chain charge transfer is examined in the framework of Troisi and co-workers' unimolecular Marcus theory via 'fluctuating bridges'.[92, 97] The Marcus-type transition rate expressions therefore incorporate polaronic effects through the reorganisation energy terms. The inter-state hopping is not restricted to nearest-neighbour donor and acceptor states, but allows for hopping between states at a range of spatial separations. Since this model describes the disorder-dependent spatial extent of the donor and acceptor states, it also predicts the disorder-

dependent relaxation energies that appear in the Marcus expressions. Finally, electronic overlaps are also calculated using a realistic formalism, which takes into account the effect of torsional disorder in the chain, resulting in a physical account of off-diagonal disorder. The majority of the work is performed using the model system of poly(*p*-phenylene-vinylene) (PPV), but comparisons to poly(2-methoxy-5-(2'-ethylhexyloxy)-*p*-phenylene vinylene) (MEH-PPV) polymers are also included.

4.1 Model Hamiltonian

The modelled PPV system is described by the Holstein Hamiltonian introduced in Chapter 2. As a reminder, the coarse-grained Hückel Hamiltonian takes the form

$$\hat{H}^{\mathrm{cg}}_{\mathrm{Hückel}} = \sum_n \epsilon_n \hat{a}^\dagger_n \hat{a}_n - \sum_n \tilde{t}_n \left(\hat{a}^\dagger_n \hat{a}_{n+1} + \hat{a}^\dagger_{n+1} \hat{a}_n \right). \tag{4.1}$$

Incorporating polaronic effects gives us the Holstein Hamiltonian, as described in Chapter 2. In the coarse-grained site basis, it can be written as

$$\hat{H}_{\mathrm{Holstein}} = \hat{H}^{\mathrm{cg}}_{\mathrm{Hückel}} - \hbar\omega \sum_n A_n \tilde{Q}_n \hat{a}^\dagger_n \hat{a}_n + \frac{\hbar\omega}{2} \sum_n \tilde{Q}^2_n,$$

whose terms have have been introduced in detail earlier in Section 2.1.3. The dimensionless charge-phonon coupling parameter, A_n, is related to the Huang-Rhys parameter, S_n, used later as $S_n = A_n^2/2$. In the model presented, only the coupling to a single local normal mode for each moiety is considered. These normal modes are the phenylene and vinylene modes illustrated in Fig. 2.3. The values of the individual parameters in the Hamiltonians are summarised in Table 4.1.

4.2 Donor and Acceptor States

4.2.1 Role of Polaronic Effects

In the adiabatic *limit*, i.e., $\hbar\omega/t \to 0$, electron-phonon coupling causes self-localised Landau polarons.[129, 130] However, as shown in Refs. [121, 122] (and

noted by Fornari and Troisi[92]), in the adiabatic *regime* relevant to conjugated polymers (i.e., $\hbar\omega/t \sim 0.1$), the self-localisation length scale is much larger than the localisation length caused by disorder (as discussed in Section 4.2.2). Thus, the "polaronic" effects considered here are "self-trapping", i.e., a reorganisation energy that appears in the Marcus rate expressions (see Section 4.3), but not a self-localised charge wavefunction.

4.2.2 Role of Disorder

The effect of disorder on the system was described in detail in Section 2.1.4 of Chapter 2. A realistic polymer system has both diagonal (on-site) and off-diagonal (torsional) disorder present, and this is reflected in the chosen simulation parameters. This disorder results in Anderson localisation of the states along each polymer chain, resulting in LGSs and QESs. Donors and acceptors in the charge transfer process are selected from these states, as detailed in the following sections.

4.3 Marcus Theory of Transition Rates

Charge transfer in disordered organic semiconductors is understood to occur via an incoherent hopping mechanism: charge carriers are confined to localised states in the polymer system and evolve in time by hopping between these states, resulting in overall charge transport.[92] This is necessarily a non-adiabatic process by nature.

Hops can occur to nearby localised states (LGSs) and thus charge travels only a short distance with each hop. Alternatively, they can occur to more delocalised states (QESs), ultimately relaxing into a localised state further away. This mechanism was examined in the literature before,[96, 97, 197, 198] and was found to be a relevant competing pathway for diffusion of quasiparticles. Both pathways are therefore implemented in the simulation program. Beyond the general introduction

of Marcus theory in Chapter 2, the relevant forms of the rate expressions used in the simulation model will be discussed below.

4.3.1 Bimolecular (inter-chain) transfer

Assuming that the normal modes on different polymer chains are decoupled, the interchain charge transfer is described by a bimolecular Marcus theory rate expression, as introduced in Section 2.2.2. In the high-temperature limit ($k_BT \gg \hbar\omega$ for all normal modes considered), when the transfer process is thermally activated, the rate is[4, 199]

$$k_{DA,\text{inter}} = \frac{2\pi}{\hbar}|w_{DA}|^2 \int D(E)A(E)\,\mathrm{d}E, \tag{4.2}$$

where w_{DA} is the resonance transfer integral between donor and acceptor states, and $D(E)$ and $A(E)$ are spectral functions.

The spectral functions for the donor ($X = D$) and acceptor ($X = A$) states are defined as

$$X(E) = \left(\frac{1}{4\pi k_BTE_\lambda}\right)^{\frac{1}{2}} \exp\left(-\frac{(E_X - E_\lambda)^2}{4\pi k_BTE_\lambda}\right), \tag{4.3}$$

where E_X denotes the energy of the donor and acceptor states

$$E_D = E_{00}^D - E \tag{4.4}$$

$$E_A = E - E_{00}^A, \tag{4.5}$$

with E_{00}^X denoting the field-dependent energy of a state, which changes with applied field, $\mathbf{F}$, as a function of the centre-of-mass position of the given state, X, as

$$E_{00}^X \to E_{00}^X - q\mathbf{F}\cdot\mathbf{R}^{\text{CoM}}. \tag{4.6}$$

E_λ is the reorganisation energy corresponding to the charge transfer process. The reorganisation energy is[131, 200]

$$E_\lambda = \hbar\omega \sum_n^{N_{\text{site}}} S_n \left|\psi_n\right|^4 = \hbar\omega S_{\text{eff}}, \tag{4.7}$$

where S_{eff} is the effective Huang-Rhys parameter and $S_n = A_n^2/2$ takes a value depending to which moiety the site corresponds (see Fig. 2.1 and Table 4.1 for its values). We note that for constant S_n we may express Eq. (4.7) as

$$E_\lambda = \frac{\hbar\omega S}{\text{PN}}, \tag{4.8}$$

where PN (the participation number) is defined as

$$\text{PN} = \frac{1}{\sum_n |\psi_n|^4}, \tag{4.9}$$

and is proportional to the wavefunction localisation length, L. Thus, from Eq. (2.16) we observe that E_λ is an increasing function of disorder. This observation has implications for the role of disorder on charge mobility, as discussed with the results below.

For the calculation of the overlap integrals, Mulliken's approximation[201, 202] is used, which estimates resonance integrals by the orbital overlap integrals multiplied by a constant. The overlap between the donor and acceptor states, D and A, respectively, is defined as

$$w_{DA} = \sum_n^{N_{\text{site}}} \sum_{i\in n} \sum_m^{N_{\text{site}}} \sum_{j\in m} w_{ij} \left(\varphi_i \psi_n^D\right) \left(\varphi_j \psi_m^A\right), \tag{4.10}$$

where the orbital overlaps, w_{ij}, between the p-orbitals on atoms i and j, are defined as[201, 202]

$$w_{ij} = S_{ij} \times 10.6\,\text{eV}, \tag{4.11}$$

$$\begin{aligned} S_{ij} = &\cos\Phi_{ij}\,\cos\Omega_{ij}\,\cos\Theta_{ij} \times S_{2p_z,2p_z}(r_{ij}) \\ &- \sin\Omega_{ij}\,\sin\Theta_{ij} \times S_{2p_\sigma,2p_\sigma}(r_{ij}), \end{aligned} \tag{4.12}$$

with

$$\Phi_{ij} = \arccos\left(\hat{\mathbf{p}}_\mathbf{i} \cdot \hat{\mathbf{p}}_\mathbf{j}\right) \tag{4.13}$$

$$\Omega_{ij} = \arcsin\left(\hat{\mathbf{p}}_\mathbf{i} \cdot \hat{\mathbf{r}}_\mathbf{ij}\right) \tag{4.14}$$

$$\Theta_{ij} = -\arcsin\left(\hat{\mathbf{p}}_\mathbf{j} \cdot \hat{\mathbf{r}}_\mathbf{ij}\right), \tag{4.15}$$

where $\hat{\mathbf{p}}_\mathbf{i}$ and $\hat{\mathbf{p}}_\mathbf{j}$ are the unit vectors parallel to the p_z orbitals on atoms i and j, respectively, and $\hat{\mathbf{r}}_\mathbf{ij}$ is the unit vector parallel to the vector from atom i to j. Finally,

$$S_{2p_z,2p_z}(r) = \exp\left(-r\xi\right)\left(1 + r\xi + \frac{2}{5}(r\xi)^2 + \frac{1}{15}(r\xi)^3\right) \tag{4.16}$$

$$S_{2p_\sigma,2p_\sigma}(r) = \exp\left(-r\xi\right)\left(-1 - r\xi - \frac{1}{5}(r\xi)^2 + \frac{2}{15}(r\xi)^3 + \frac{1}{15}(r\xi)^4\right), \tag{4.17}$$

where $\xi = 3.07\,\text{Å}^{-1}$ and r is the interatomic separation.

4.3.2 Unimolecular (intra-chain) Transfer

The model separately allows for charge hopping along a polymer chain. In particular, dynamical torsional fluctuations will cause non-adiabatic transfers via the "fluctuating bridges" mechanism proposed by Skourtis[96] and further examined by Troisi et al.[92, 97] This perturbative expression is given by

$$k_{DA,\text{intra}} = k^{(0)} + k^{(2)}, \tag{4.18}$$

where

$$k^{(0)} = \frac{\langle V^2\rangle}{\hbar}\sqrt{\frac{\pi}{E_\lambda k_B T}}\exp\left(-\frac{(\Delta E^0 - E_\lambda)^2}{4E_\lambda k_B T}\right), \tag{4.19}$$

and

$$k^{(2)} = k^{(0)}\frac{2\hbar^2}{\tau_c^2}\left[\frac{(\Delta E^0 - E_\lambda)^2 - 2E_\lambda k_B T}{(4E_\lambda k_B T)^2}\right]\left(1 - \frac{\langle V\rangle^2}{\langle V^2\rangle}\right). \tag{4.20}$$

τ_c is the rotational correlation timescale. The second order correction, $k^{(2)}$, is $\sim 1-2$ orders of magnitude smaller than the leading order term. The coupling term, $\langle V^2\rangle$,

arises from torsional rotational motion in the polymer chains and takes the form

$$\langle V_{ij}^2 \rangle = \left(\tilde{t}_0 \sin\theta_0\right)^2 \left(\frac{k_B T}{K_{\rm tor}}\right) \sum_{n=1}^{N-1} \Big\{ (\psi_n^i \psi_{n+1}^j)^2 + (\psi_n^i \psi_{n-1}^j)^2 \Big\}, \tag{4.21}$$

where $\tilde{t}_0$ is the transfer integral, θ_0 is the mean torsional angle between neighbouring monomers in the chain, and $K_{\rm tor}$ is the elasticity constant for torsional motion. In Eq. (4.21) we have used $\langle \delta\theta^2 \rangle = k_B T / K_{\rm tor}$ from the principle of equipartition.

The reorganisation energy for intramolecular transfer is determined by considering the two states involved, D and A, on the polymer chain. Generalising Eq. (4.7), this is

$$E_\lambda = \hbar\omega \sum_{n}^{N_{\rm site}} S_n \Big\{ (\psi_n^D)^2 - (\psi_n^A)^2 \Big\}^2, \tag{4.22}$$

where S_n is the Huang-Rhys parameter for the $n^{\rm th}$ moiety as described above.[1]

4.4 Realistic Polymer Conformations

Polymer chain conformations are generated through a series of vector additions, building up the polymer chains by one monomer unit at a time, starting and ending with a phenylene unit. Fixed bond lengths of 1.39 Å, 1.33 Å and 1.44 Å for the phenylene ring, the vinylene double bond and the single linking bond between the moieties, respectively, are used.[203] The bond angles in the phenylene ring, as well as the angle between the single and double bond of the vinylene units, is 120°. The values (both mean and standard deviation) of the torsional angles – assumed to follow a Gaussian distribution – between the planes of the neighbouring phenylene and vinylene units are controlled by input parameters of the simulation, as shown in Table 4.1. The average monomer spacing[204] is used to calculate the volume of the simulation box. Generated polymer chains are then randomly distributed within the

[1] The cross-terms in Eq. (4.22), i.e., $-2(\psi_n^D)^2(\psi_n^A)^2$ arise because the reorganisation energy vanishes when the donor and acceptor states spatially overlap.

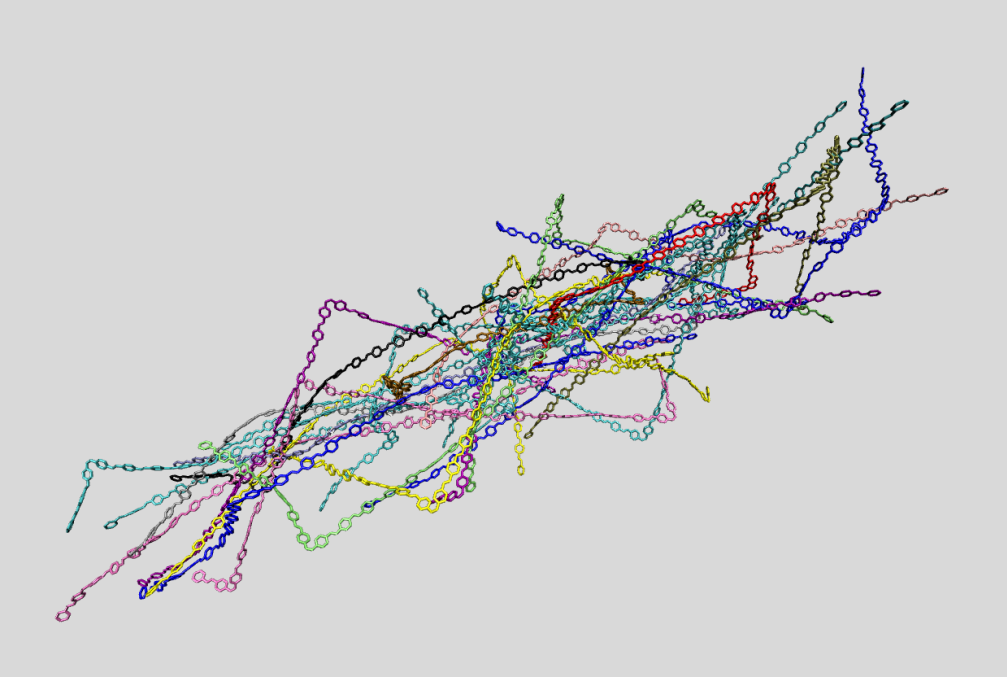


Figure 4.1: Randomised polymer chain morphology from the simulation code, showing 'home box' polymer chains only.

calculated simulation box. Periodic boundary conditions are implemented with 18 neighbouring boxes (side and edge-sharing boxes of the 'home' box). The periodic boundary conditions mean that when a charge lands in one of the neighbouring simulation boxes, it is reset to the equivalent state in the 'home' box before the next charge transfer event. The density within the 'home' box is $1.65 \pm 0.05\,\mathrm{g\,cm^{-3}}$, which is higher than the experimentally measured density of $\sim 1.24 - 1.28\,\mathrm{g\,cm^{-3}}$.[205] The system size considered in the simulations is 100 polymer chains of 300 ring units (or 599 coarse-grained sites) each, as charge mobilities were found to plateau as a function of size at these values. The option to add cis/trans defects in the vinylene units with a given probability is controlled by the input parameters.

4.5 Kinetic Monte Carlo

The charge dynamics in this model is simulated using the kinetic Monte Carlo (kMC) approach described in Chapter 3. This approach allows for certain states to

Table 4.1: Parameters used in the simulations.

Phonon energy	$\hbar\omega$	0.2 eV
Huang-Rhys parameter (phenylene)	S_P	0.91
Huang-Rhys parameter (vinylene)	S_V	2.00
Transfer integral	$\tilde{t}_0$	0.90 eV
Phenylene on-site interaction	ϵ_P	2.4 eV
Vinylene on-site interaction	ϵ_V	2.6 eV
Mean torsional angle	θ_0	10°
On-site energetic disorder	σ_ϵ	$0.0 - 0.4$ eV
Torsional disorder	σ_θ	$10 - 20°$
Probability of cis/trans defects	$P_{\text{cis/trans}}$	0% or 10%
Elasticity for torsional motion	K_{tor}	10.5 eV
Rotational correlation time	τ_c	15 ps
Average monomer spacing		4 Å

'trap' the charge and therefore lower the drift velocity, and consequently the mobility. The formulation of transition rates incorporates a link to the torsional dynamics of chains via the rotational correlation timescale, τ_c. For PPV systems, this is estimated to be ~ 15 ps.[206] It can therefore be argued that this is the longest timescale that a charge is allowed to dwell in a state within the framework of the static disorder model; a longer charge trapping time is avoided by randomly placing the charge carrier into a different donor state on the same chain and continuing the random walk of the charge carrier from that state.

The relaxation from QES to LGS states is assumed to be significantly faster than the hops between LGS states and LGS to QES states, and is therefore assumed to occur instantaneously. The probability of this rapid intramolecular relaxation, P_{if}, is defined by

$$P_{if} = \frac{\alpha_{if}}{\sum\limits_f \alpha_{if}}, \tag{4.23}$$

where

$$\alpha_{if} = \sum_n |\psi_n^i|^2 |\psi_n^f|^2 \tag{4.24}$$

and the sums are taken over all sites on the chain, n, and the initial QES state and final LGS state on the same chain are denoted by ψ_n^i and ψ_n^f, respectively. This means that only LGSs can act as donor states in this model. These charge propagation pathways are illustrated in Fig. 4.4.

Each kMC random walk is run until a set total simulation time is achieved; the displacement as a function of time is used to calculate the drift velocity and hence the charge mobility. Sampling over a large number of trajectories and multiple polymer morphologies was performed at each field strength value and initial parameter set to obtain results with no significant statistical fluctuations. In practice, this meant 10 MC trajectories initiated on each polymer chain in the simulation 'home' box (1000 MC trajectories), and the process was repeated over $5-10$ realisations of the randomised structural and energetic landscape, through the use of different random number seeds, leading to $5000-10000$ total MC trajectories at each given set of parameters. Outlier values (MC trajectories resulting in charge mobilities more than two standard deviations away from the total sample mean) were excluded from the final averages. Each MC trajectory was run for a sufficiently long time that the time dependence of charge displacement, $\langle X(t)\rangle$, was in the linear, i.e., drift-controlled, regime. This can be understood from the following considerations. Diffusive displacement is controlled by the diffusion relation

$$\left\langle X^2(t)\right\rangle = 2Dt, \tag{4.25}$$

where D denotes the diffusion constant of the process. This means that the root mean square displacement, X_{rms}, has a time dependence of

$$X_{\mathrm{rms}} \propto \sqrt{t}. \tag{4.26}$$

On the other hand, drift induced displacement is described as

$$X_{\text{drift}} \equiv \langle X(t) \rangle_{\text{drift}} = vt, \tag{4.27}$$

where v is the drift velocity of the charge carrier. These two relations show that drift dominated behavior, i.e., when $X_{\text{drift}} > X_{\text{rms}}$, occurs when the kinetic Monte Carlo trajectories are run for sufficiently long times. The fulfilment of this condition is shown in Figs. 4.2 and 4.3 across a range of electric field strength values.

Charge mobility values were obtained from averaging the drift velocities obtained from each MC trajectory, and then using the drift mobility formula

$$\mu = \frac{\langle v(F) \rangle}{qF}, \tag{4.28}$$

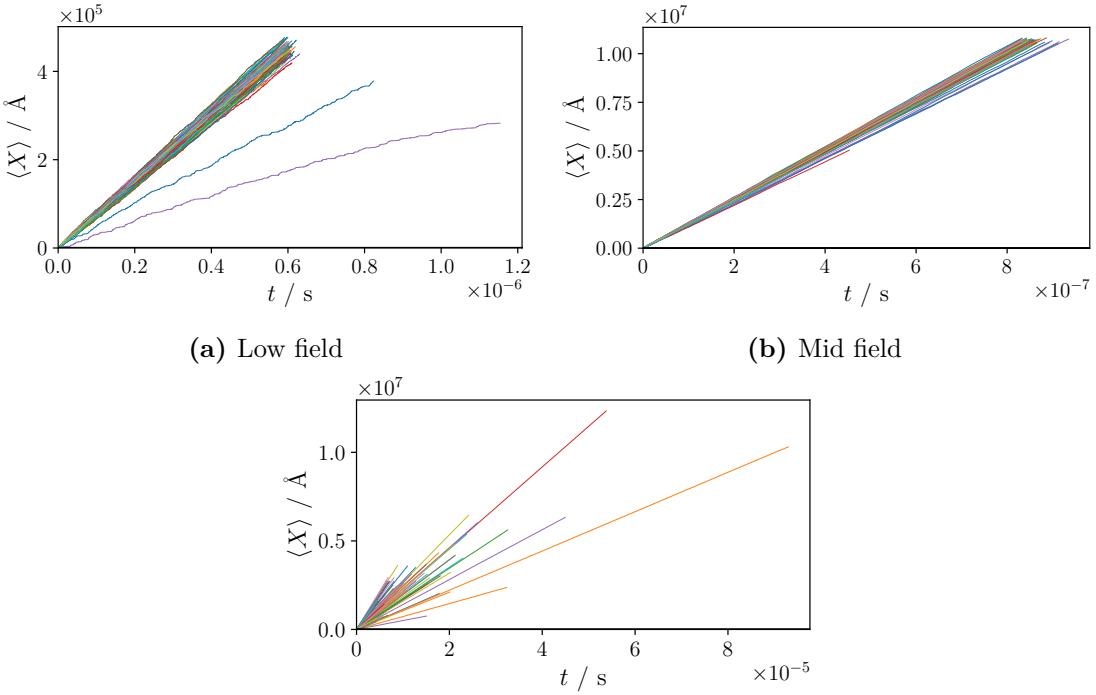
where $v(F)$ is the field-dependent drift velocity of the charge carrier and q is its charge.

In the model, various tuneable parameters were used, and are presented in Table 4.1. In particular, for the various values of on-site disorder ($\sigma_\epsilon = 0.0 - 0.1 - 0.2 - 0.4\,\text{eV}$), the effective disorder, σ_E, i.e. the width of the LGS portion of the total DOS, was found to be $28 - 143\,\text{meV}$, which is $\sim (1 - 5) \times k_B T$ at 298 K. This is in agreement with values reported elsewhere in the literature.[47, 78, 207, 208]

4.6 Mobility with LGS-only Hopping

4.6.1 Electric Field Dependence

Charge mobility was initially examined via hopping between the highly localised, low energy states (LGSs) only. This would correspond to a pathway made up of only the green arrows shown in Fig. 4.4. The dependence of average transition rates, hopping distances and ultimately charge mobility on temperature, disorder and polymer chain orientations are presented in this section.



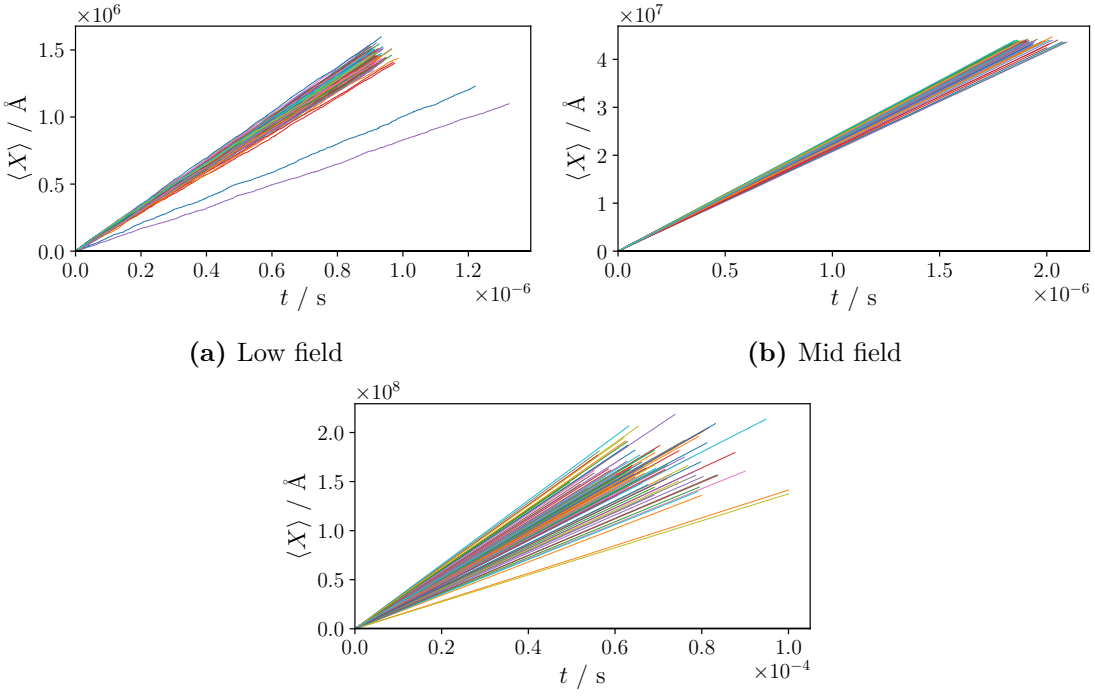
(a) Low field **(b)** Mid field

(c) High field

Figure 4.2: Time dependence of charge carrier displacement in multiple kMC trajectories. The drift velocity is given by the gradient of each trajectory. LGSs only transport.

The average rates shown in Fig. 4.5 are the means of the sums of transition rates, $\langle \sum_A k_{DA} \rangle_D$, out of each possible donor states, D, i.e., the total rate of charge carriers flowing out of a given donor state. A linear $\log k_{DA}$ vs $-\sqrt{F}$ regime is observed at high fields, despite none of the rate expressions used in the model containing this proportionality explicitly. The observation that in the high field regime higher disorder leads to higher transition rates is explained by the facts that first, at low disorder with a narrower DOS, the energetic differences between states are lower and so the large field bias pushes the system further into the Marcus inverted regime than for higher disorder. Second, as Eqs. (2.16) and (4.8) show, at higher levels of disorder, the localisation length is reduced, and therefore the reorganisation energy increases. This shifts the Marcus inverted regime to higher field strength values.

Figure 4.6 shows the fraction of hops that took place in the kMC simulations,



(a) Low field **(b)** Mid field

(c) High field

Figure 4.3: Time dependence of charge carrier displacement in multiple kMC trajectories. The drift velocity is given by the gradient of each trajectory. LGSs+QESs transport.

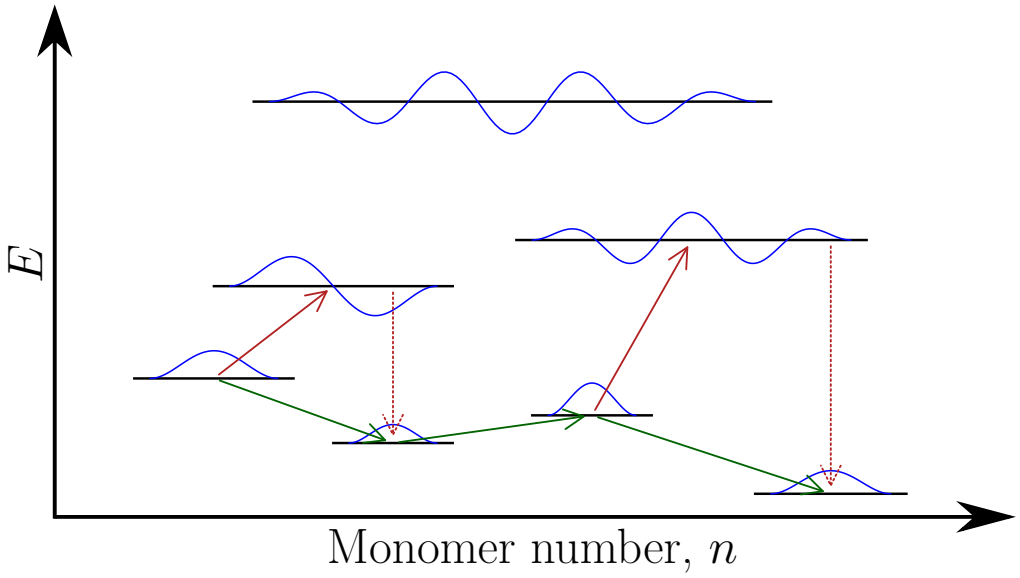


Figure 4.4: Marcus hopping. Green arrow: LGS → LGS hop, red solid arrow: LGS → QES hop, red dotted arrow: QES → LGS relaxation.

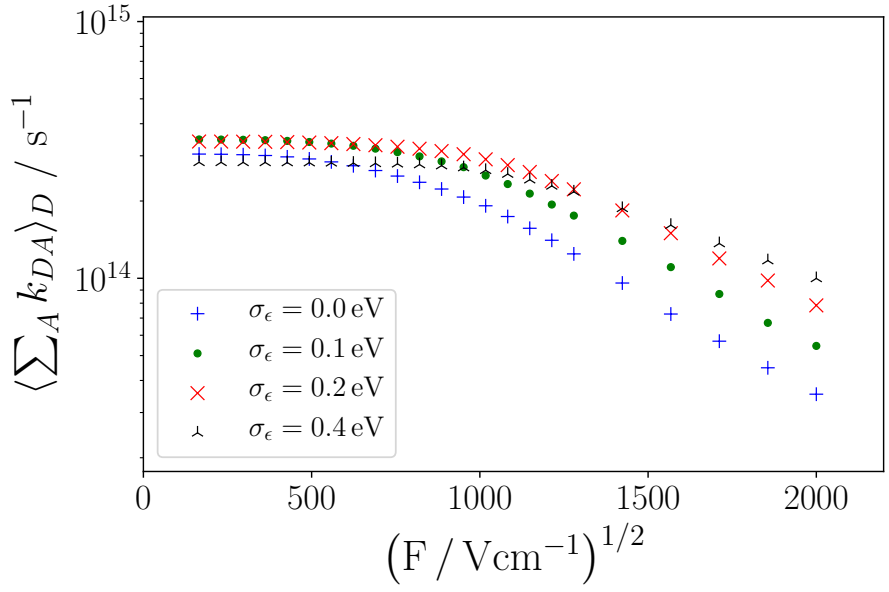


Figure 4.5: The total charge carrier escape rates from donor states as a function of electric field, averaged over all possible donor states, plotted at various levels of on-site disorder for randomly oriented chains with 10% cis/trans defects, 10° torsional disorder at 298 K temperature. LGSs to LGSs only transitions.

being classified either as an intermolecular or intramolecular transition. It is observed that charge transport seems to be driven almost exclusively by intermolecular hops, across all field strength values. This is explained by the small spatial overlap between LGSs found on the same polymer chain (as shown in Fig. 2.5), leading to low intramolecular transition rates.

Charge mobilities were calculated over a range of parameters and field strength values; the results presented in Figs. 4.7 to 4.11 demonstrate the trends observed in charge mobilities as a response to changing a single simulation parameter in turn. The parameter set for the data set in red is the same in plots Figs. 4.7 to 4.11, i.e., randomly oriented chains with 10% cis/trans defects, 0.2 eV on-site and 10° torsional disorder at 298 K temperature. The parameters for the other data sets are the same, except as indicated otherwise in the legends.

Three different relative orientations of polymer chains were considered. A quasi-parallel orientation of the polymer chains was ensured by aligning the end-to-end

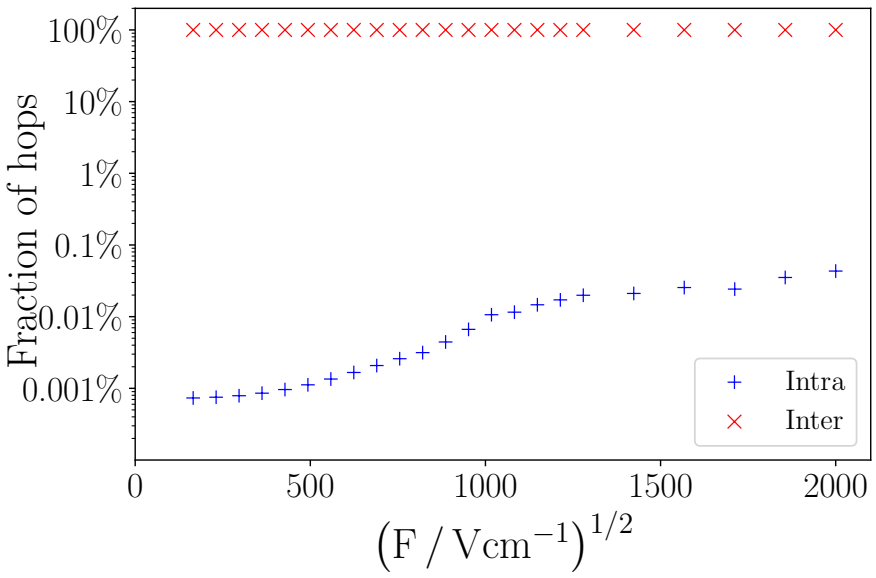


Figure 4.6: Fraction of hops being either inter or intramolecular for the kMC. Same simulation parameters as Fig. 4.5, with $\sigma_\epsilon = 0.2\,\mathrm{eV}$. LGSs to LGSs only transitions.

vectors of polymer chains. For quasi-parallel chains, the simulations were performed both with the electric field parallel (longitudinal) to the common chain orientation as well as it being applied in the perpendicular (transverse) direction. Further to these, a more realistic model of disordered polymer chains, i.e., molecules with randomised alignment was also investigated. The variation in charge mobility with orientation is presented in Fig. 4.7, showing that the mobility is independent of chain orientations in the low field regime. At high fields, however, the higher mobilities were observed for transverse and randomly oriented chains, both being significantly higher than the longitudinal case. This can be explained by the low intramolecular transition rates for LGS-only transitions, as it would be mostly intramolecular hops resulting in charge movement along the field direction in the longitudinal case.

In real polymer systems, structural defects in the form of cis/trans defects can be observed, leading to some of the vinylene units taking a cis bond arrangement rather than the energetically favourable trans one, resulting in the coiling of

polymer chains. In Fig. 4.8 it is shown that coiling of the chains results in significantly higher mobilities, as this structural defect can bring intermolecular donor-acceptor pairs closer together spatially, improving wavefunction overlaps and therefore transition rates.

The effect of varying on-site energetic disorder in the polymer chains is shown in Fig. 4.9. The effect of disorder is larger at low fields, which can be attributed to the larger disorder resulting in larger activation barriers to charge transfer. The effect of these differences diminishes as the applied energetic bias due to the electric field increases. As with the transition rates presented in Fig. 4.5, the inversion at high fields was observed once again – increasing disorder leads to slightly, but consistently higher mobilities. The explanation for this is that the higher levels of disorder lead to wider distribution of donor-acceptor energetic differences, as well as the localised states becoming more localised spatially, leading to larger reorganisation energies. Both of these contributions have the potential effect of counteracting large energetic biases coming from the applied electric field, leading to higher transition rates, due to being pushed less far into the Marcus inverted regime. The same trends emerge from changing the level of structural (torsional) disorder, shown in Fig. 4.10.

Figures 4.9 and 4.10 indicate that in the low-field (normal Marcus) regime the role of disorder is significant: doubling either the on-site or torsional disorder leads to a reduction in the mobility by up to two orders of magnitude. Experimentally measured charge mobilities for PPV-based systems range between $10^{-8} - 10^{-3}$ $\mathrm{cm^2\,V^{-1}\,s^{-1}}$ based on the applied field strength value and charge carrier density.[39, 47, 49–53, 75] This suggests that the larger levels of disorder show better quantitative agreement with experimental results. The overall energetic disorder (defined in Eq. (2.18)), σ_E, for $\sigma_\epsilon = 0.2\,\mathrm{eV}$ and $\sigma_\theta = 20°$ is $\sim$ 156 meV, and for $\sigma_\epsilon =$ 0.4 eV and $\sigma_\theta = 10°$, it is $\sim 143\,\mathrm{meV}$. These values are close to the disorder

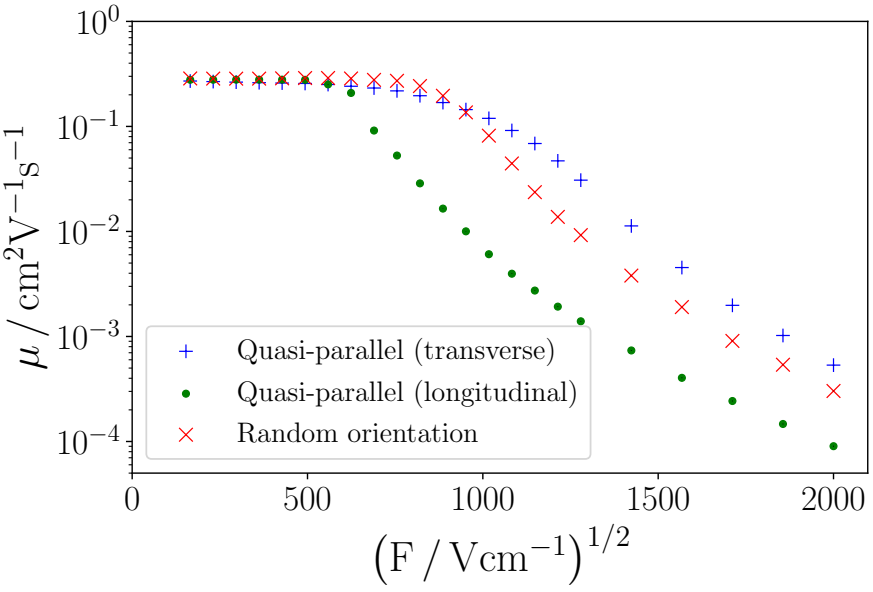


Figure 4.7: Charge mobilities obtained from simulations involving hops between low-energy localised grounds states (LGSs) only. Presented are results with varying relative chain and electric field orientations.

parameters reported in the literature, obtained from fitting Bässler's formula to experimental measurements.[207] A discussion of more realistic modelling for PPV is presented in Section 4.8.

4.6.2 Temperature Dependence

Next, the temperature dependence of charge mobility was examined. As shown in Fig. 4.11, changing the simulation temperature was found to only affect mobilities at low fields, as the results converge at high fields, where the energetic differences due to the applied field bias become the dominant driving force. The differences in low fields behaviour is interpreted as follows: at 120 K and 180 K the thermal energy is too low to overcome all the activation barriers to transport, and therefore charge mobility is initially increased by the application of a field bias, until a maximum is reached, at which point the reduction due to entering the Marcus inverted regime occurs. As the temperature is increased, the gradient of low field

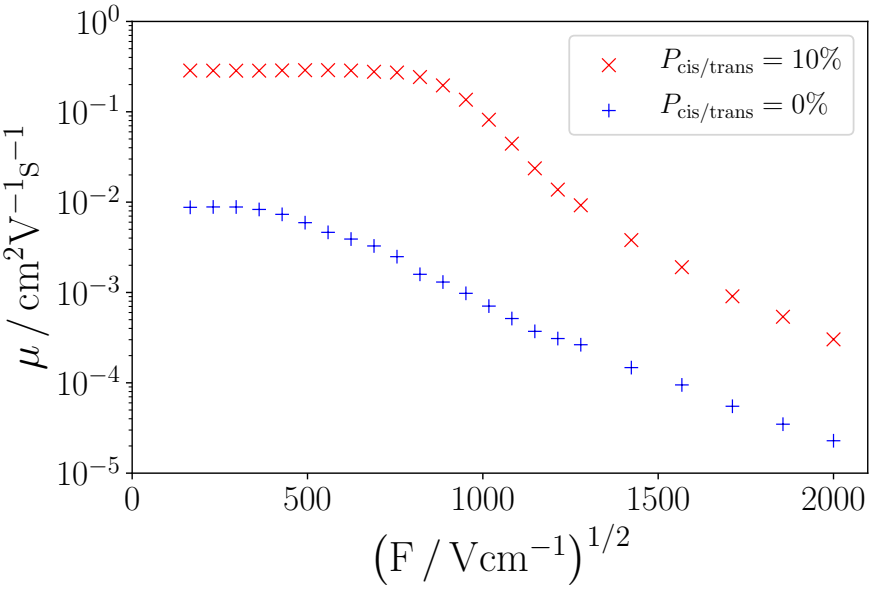


Figure 4.8: Charge mobilities obtained from simulations involving hops between low-energy localised grounds states (LGSs) only. Presented are results with varying levels of cis/trans disorder.

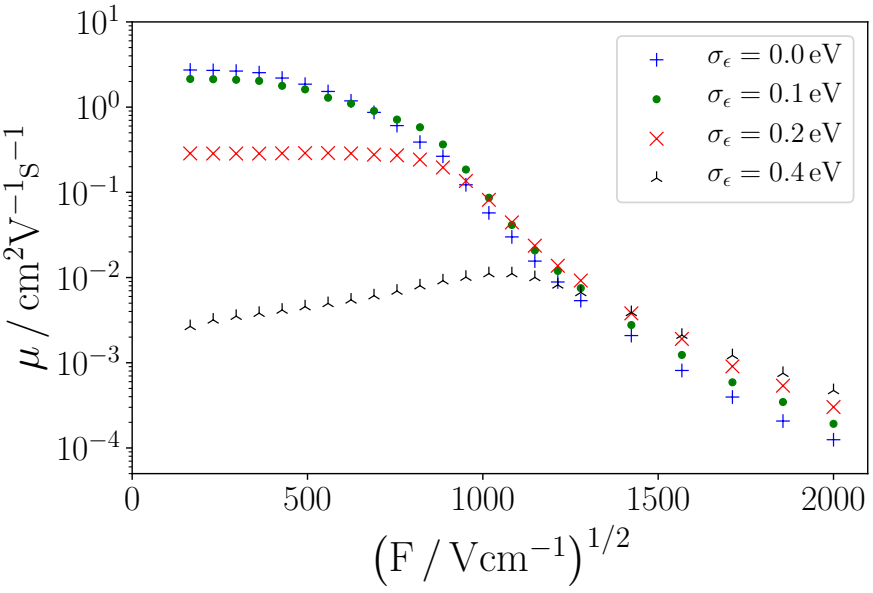


Figure 4.9: Charge mobilities obtained from simulations involving hops between low-energy localised grounds states (LGSs) only. Presented are results with varying magnitude of on-site energetic disorder.

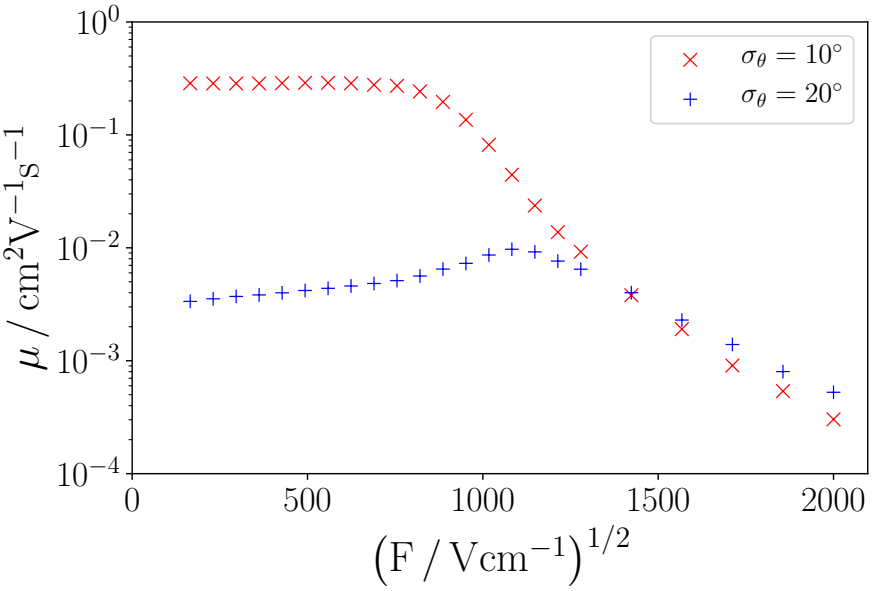


Figure 4.10: Charge mobilities obtained from simulations involving hops between low-energy localised grounds states (LGSs) only. Presented are results with varying magnitude of torsional disorder.

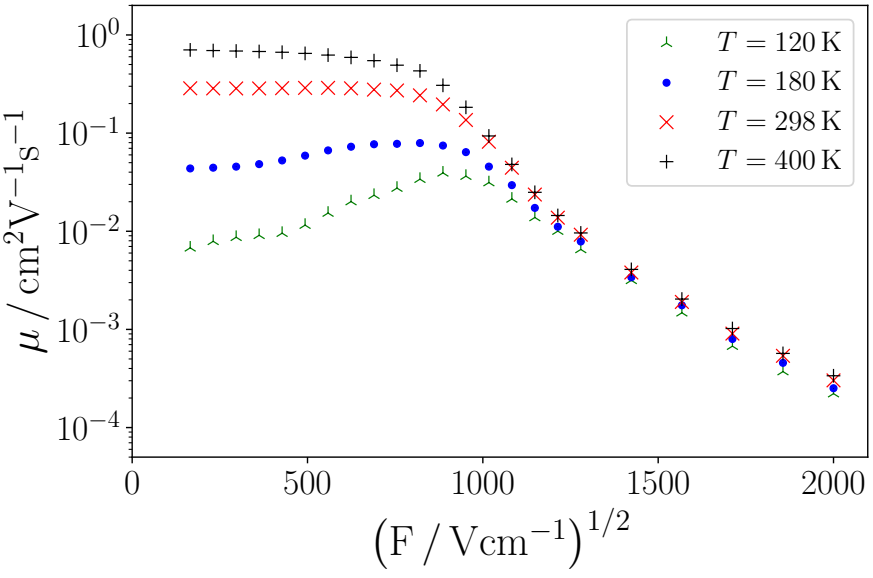


Figure 4.11: Charge mobilities obtained from simulations involving hops between low-energy localised grounds states (LGSs) only. Presented are results with varying temperatures of simulation.

mobility decreases, and becomes slightly negative at 400 K. This change is in qualitative agreement with the generally accepted[78–81] experimentally verified[53, 54, 71] relation describing charge mobility presented in Eq. (1.6).

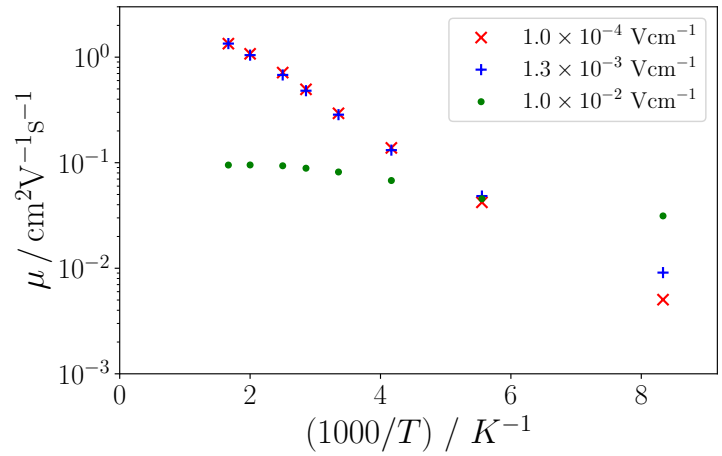
Fishchuk and co-workers developed[86] a unified description of charge mobility at low fields, accounting for both polaron and disorder effects, leading to the temperature dependence described by Eq. (1.6), namely

$$\mu(T) \propto \exp\left[-\frac{E_a}{k_B T} - C\left(\frac{\sigma}{k_B T}\right)^2\right], \tag{4.29}$$

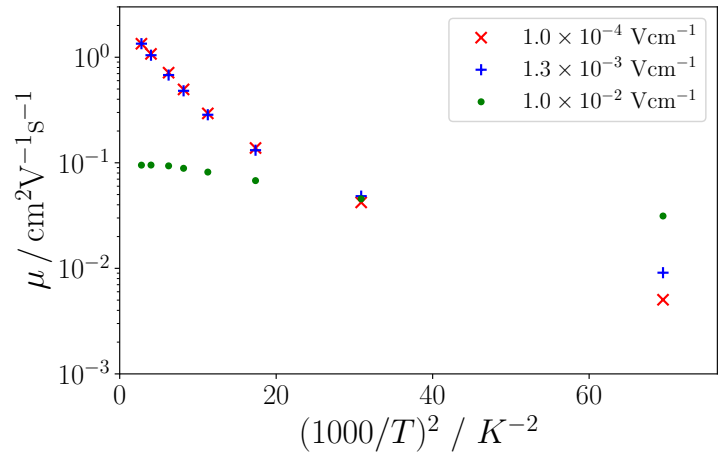
where the terms are the same as those described for Eq. (1.6). In this description, the first term is an Arrhenius-type dependence, capturing polaronic effects, whereas the second term accounts for disorder effects. As shown in Figs. 4.9 to 4.11 already, our model produces results which are consistent with the second term, showing a reduction in charge mobility both with increased disorder and lower temperatures at low fields. Fishchuk's analysis predicts a cross-over from disorder controlled transport to a polaron controlled mechanism at a critical temperature,

$$T_c = \frac{C}{k_B E_a}\sigma^2, \tag{4.30}$$

where the factor C itself depends on the ratio of disorder, σ, and polaron activation energy, E_a, varying in the range of $1/8 < C < 1$. E_a can be obtained in terms of the reorganisation energy, E_λ, as $E_a = E_\lambda/4$. Based on the model parameter set, corresponding to $\sigma_E \approx 62.5$ meV and $E_\lambda \approx 19$ meV, this expression predicts $T_c > 1000$ K, suggesting disorder controlled transport at all temperatures probed in this work. This prediction was examined through the behaviour of mobility, plotted against both $1/T$ and $1/T^2$, as shown in Figs. 4.12a and 4.12b. Based on these figures, we cannot conclusively deduce either polaron or disorder dominated transport behaviour, but the Arrhenius-type, $\log \mu \sim 1/T$, plot (Fig. 4.12a) appears



(a)



(b)

Figure 4.12: Charge mobility, μ, plotted against (a) $1/T$, and (b) $1/T^2$, for temperatures $120 - 600$ K. The field-strength values for each dataset are shown in the legend. The lowest field-strength value, shown in red, represents approaching the zero-field limit. The standard parameter set was used, same as in Fig. 4.11.

more linear. However, as noted previously, the nature of temperature dependence is often hard to ascertain when considering such narrow temperature ranges, and either formula can result in a reasonable fit.[47, 53, 62]

It should also be noted that temperature affects the localisation length via the temperature dependence of the torsional disorder. As it is difficult to quantify this dependency in the condensed phase, however, such effects are not considered here.

4.7 Exploring the Role of QES States

The role of the energetically higher lying, more delocalised QESs in charge transport was examined by considering the effect of their inclusion on the transition rates, nature of transport hops, average hopping distances and charge mobility. The number of allowed QES acceptors for each donor state was determined by a spectral overlap cutoff, only keeping donor-acceptor pairs that have sufficient energetic overlap to result in transition rates high enough to compete with the LGSs to LGSs transitions considered previously. This approach would translate to allowing all of the illustrated pathways in Fig. 4.4.

The transition rates presented in Fig. 4.13 show no significant changes in overall magnitude or in the trends observed for various levels of on-site disorder and the strength of electric field applied, when compared to LGSs only transitions (shown in Fig. 4.5). This indicates that any differences observed for the charge mobility results with the inclusion of QESs will not be a result of significantly different transition rates.

As a result of the increased hopping distances – states away from the band edge are less localised,[143] so LGS to QES transitions will generally result in larger charge displacement – and the involvement of intramolecular hops in the charge transport process (because of better spatial overlap), charge mobilities are higher at all field strength values when LGS to QES transitions are included. As shown in Fig. 4.14, it is observed that at very low field values the inclusion of QESs as possible acceptors leads to a small increase in mobility that is difficult to account for, however this feature is also present in simulations and experimental work from Bässler and co-workers.[46, 78] Their reasoning for such an increase is that charge carriers may be able to take fast, thermally activated routes partially against the

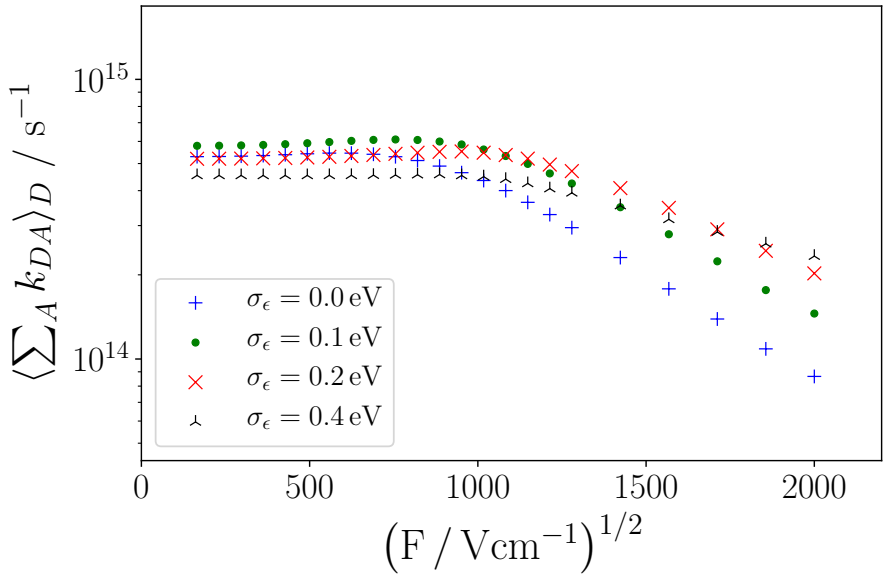


Figure 4.13: The total charge carrier escape rates from donor states, averaged over all possible donor states, plotted at various levels of disorder, allowing for LGSs to QESs transitions.

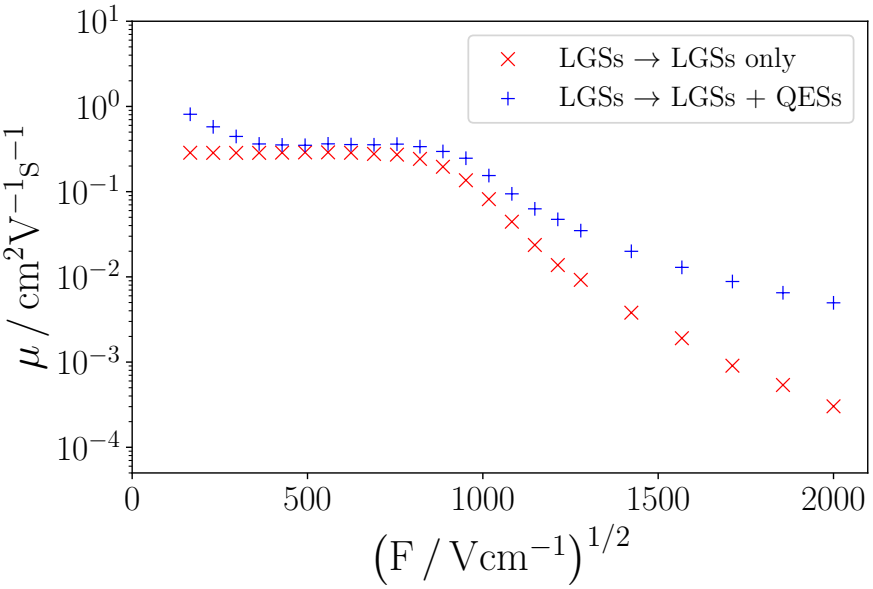


Figure 4.14: Comparison of charge mobilities obtained from simulations involving hops between low-energy localised grounds states (LGSs) only as well as from LGSs to QESs. The same parameter set as for the red symbols of Figs. 4.7 to 4.11.

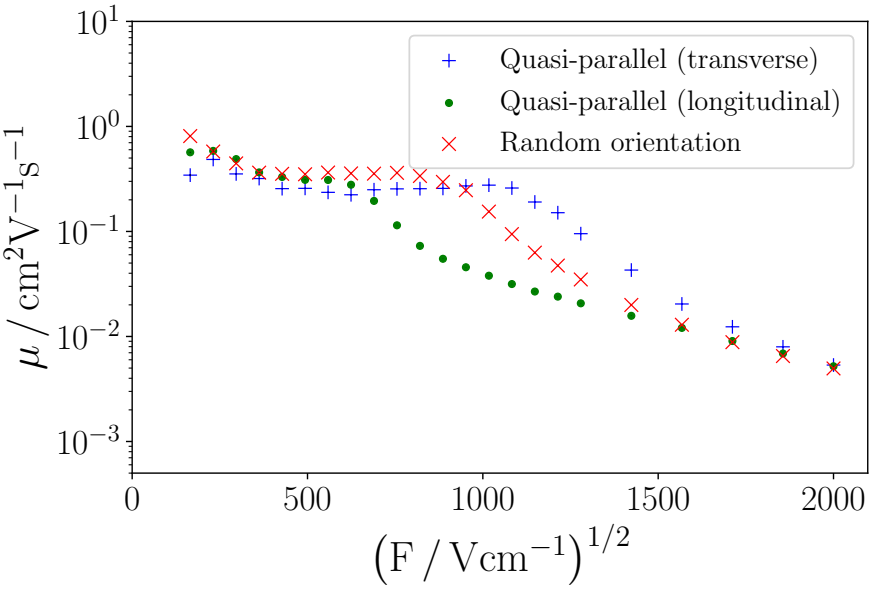


Figure 4.15: Field/chain orientation dependence of charge mobility when allowing hops from LGSs to both LGSs and QESs. The inclusion of QESs as acceptor states reduces the system anisotropy. The same parameters as Fig. 4.7.

applied electric field, which are shut off as the electric field bias increases. As we do not observe significantly higher transition rates in this field regime, we cannot confirm this reasoning. We can also discount the possibility of diffusive motion dominating drift motion,[87] because, as shown in Figs. 4.2 and 4.3, the simulation times are always long enough for drift motion to dominate.

For the rest of the low field regime, the differences remain relatively small, but the inclusion of QESs has a significant impact at high fields, leading to an increased mobility by up to two orders of magnitude, while still retaining the decreasing trends in the inverted Marcus regime.

The introduction of QESs as potential acceptors also reduces the dependence of charge mobility on the orientation of polymer chains with respect to each other and the applied electric field, as shown in Fig. 4.15. At low fields, there is no clearly favoured orientation. At mid-field-strength, the same ordering is observed as in Fig. 4.7, but at high fields, in the inverted Marcus regime, the mobilities

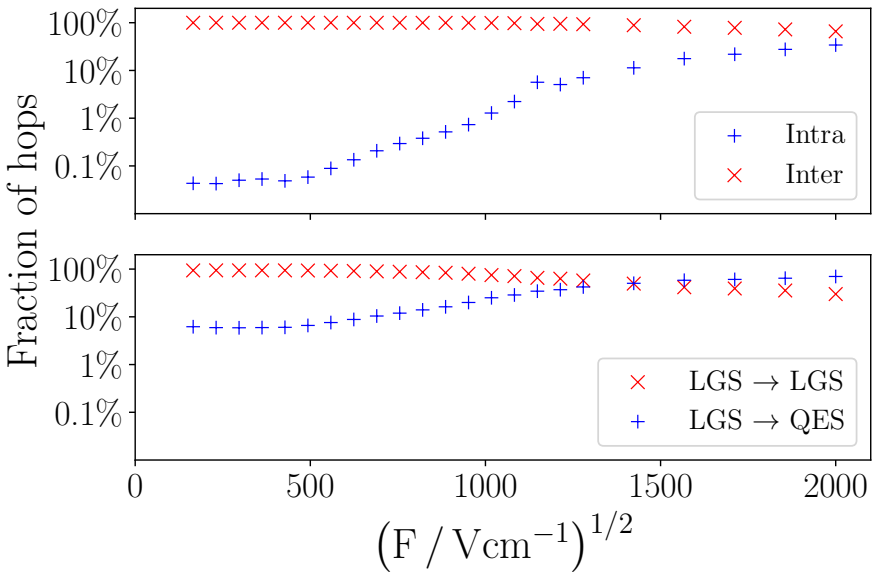


Figure 4.16: Fraction of hops occurring either inter or intramolecularly and from either LGS to LGS or LGS to QES, for the same system as in Fig. 4.6 but with the inclusion of QESs.

converge again, becoming orientation-independent.

Looking at the hopping ratios in Fig. 4.16, it is observed that the fraction of intramolecular hops is highly correlated with the fraction of LGS to QES hops. At higher field strength values, intramolecular transport competes equally with intermolecular transport, while LGS to QES transitions become the dominant mode of charge transfer. This is because at higher field strengths the higher energy QESs are pulled down in energy to become quasi-degenerate with the LGSs. This clearly emphasises the importance of QESs and hence variable range hopping in the intramolecular transport mechanism for large fields. This also helps explaining why the charge mobilities observed without and with the inclusion of QESs (Figs. 4.7 and 4.15, respectively) are qualitatively different at high field strength values.

4.8 Comparison to MD Polymer Conformations

To further assess the model's applicability, even better PPV-like polymer structures were examined. Qin and Troisi performed molecular dynamics (MD) simulations on poly(2-methoxy-5-(2'-ethylhexyloxy)-p-phenylene vinylene) (MEH-PPV) oligomer systems.[144] Their simulations on 20 and 40 chains, of 16 monomer units each, were equilibrated at 300 K and dynamics were simulated for 200 ns. Snapshots taken at 0.1 ns intervals were used to obtain structural parameters from their results, leading to dynamics-based parameters for the mean torsional angle, $\theta_0 = 26.6°$, its standard deviation, $\sigma_\theta = 16.8°$, the ratio of cis/trans defects in the vinylene units, $P_{\text{cis/trans}} = 22\%$, and the system density determined monomer spacing, equal to 6 Å. Given that the standard deviation of the transfer integral, σ_t, depends on both the mean and the standard deviation of the torsional angles, as shown in Eq. (2.14), these represent a higher level of disorder than those previously used in the simulations, and even without on-site energetic disorder, lead to an effective disorder of $\sigma_E = 190$ meV. The equilibrated geometries also confirmed that chains are randomly oriented with respect to each other, in agreement with the orientation previously used as most realistic. Simulations in our model were performed using LGSs to LGSs only transfer using these parameters. As no value of on-site energetic disorder, σ_ϵ, could be extracted from the MD results, this was ignored for the purpose of these simulations to avoid introducing further parametric assumptions not derived from the MD simulations. The charge mobility results are shown in Fig. 4.17. The trends observed are in agreement with other high disorder simulations, previously presented in Figs. 4.9 and 4.10: low field mobility is field-assisted before reaching a maximum, and then decreases with increasing electric field due to the Marcus

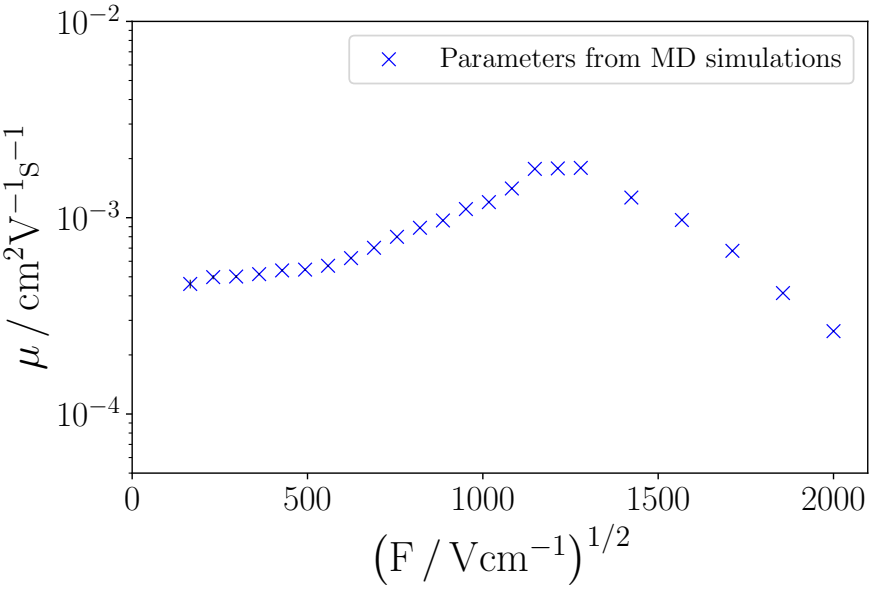


Figure 4.17: Charge mobility from simulations with structural parameters obtained from Qin and Troisi's MD simulation.[144]

inverted regime. This realistic parameter set also reduced the charge mobility in general, leading to a better agreement with experimental values.[39, 47, 49–53, 75]

4.9 Summary

In this work, a realistic theory has been presented and the modelling of charge mobility in conjugated polymer thin films has been described. Using realistic conformations of disordered PPV polymer chains, a clear link between polymer structure and the off-diagonal disorder is established. Modelling the competing intra- and intermolecular charge transport processes via Marcus theory allowed an examination of the relative importance of these in bulk charge mobility and the relative roles of localised (LGSs) and quasi-extended (QESs) states. The two main findings are follows. Firstly, charge transport is described by an almost exclusively intermolecular mechanism, involving only the LGSs dominates at low electric fields, but an important intramolecular pathway opens at high field due to the increased participation of QESs. Secondly, the encoded polymer chain structure

helped in identifying anisotropic, field orientation dependent charge mobility in certain field regimes, which can be explained by the interplay of intermolecular and intramolecular transport. The findings are summarised in more detail below.

The model agrees with experimental observations regarding the electric field dependence of charge mobility at lower field strength values,[54, 71] namely that the charge mobility obeys a Poole-Frenkel type, $\log \mu \propto \sqrt{F}$, relation. The gradient of this proportionality changes depending on the relative magnitudes of the effective disorder, σ_E, and thermal energy, $k_B T$, as Eq. (1.6) would suggest. For higher levels of disorder/lower temperature, the charge mobility is weakly field assisted; for $\sigma_E / k_B T \approx 1$, it is field-independent; and the gradient becomes negative for low disorder/high temperature (see Figs. 4.9 to 4.11). The increasing charge mobility with field strength is a feature that appears in most numerical work based on lattice GDMs and Miller-Abrahams-type rate theory.[78–81] This feature arises in some, but not all experimental charge mobility measurements.[45, 46, 53, 54, 71] Using a realistic theory of donor and acceptor states, the model justifies the predictions of GDMs.

Examining the temperature dependence of the charge mobility in the framework of Fishchuk and co-workers'[86] description of polaron or disorder controlled transport, a better linear fit is observed for the $\log \mu \sim 1/T$ plot, suggesting polaron controlled transport, but as highlighted by Fishchuk, differentiating a goodness of fit between $\log \mu \sim 1/T$ and $\log \mu \sim 1/T^2$ plots over a limited temperature range is often quite challenging. Therefore, it cannot be conclusively deduced whether the transport is controlled by either polaron or disorder based on the results.

The model predicts that the charge mobility undergoes a $\log \mu \propto -\sqrt{F}$ reduction in the high electric field regime, which is observed in the charge transfer rates as well, and is attributed to the high field bias pushing the system into the inverted

Marcus regime. This agrees with experimental observations for doped polycarbonate systems[48, 88] and analytical work performed in the framework of Marcus theory for 1D systems.[89] Similar conclusions about the high field behaviour were reached by numerical work in the framework of Marcus theory.[84]

It is found that including only the highly localised states, LGSs, in the charge transport process leads to an almost exclusively intermolecular transfer mechanism, regardless of disorder, temperature or field orientation. These results are easily rationalised by the poor wavefunction overlap between LGSs on the same polymer chain. As will be shown the next chapter, the introduction of increased torsional fluctuations drive the intramolecular transfer process.

The inclusion of QESs as potential acceptor states seems particularly important for intramolecular transport, as these states have better spatial wavefunction overlap with LGSs on the same polymer chain. They also enable larger hopping distances with respect to the electric field bias. Thus, there is an increased fraction of intramolecular transport and higher overall charge mobility. The role of higher energy QESs as potential acceptors for donor LGSs becomes especially significant at higher fields, because their energies are pulled down by the electric field. This has consequences for the next conclusion.

At low and high field strengths the charge mobility is isotropic (i.e., independent of field orientation with respect to molecular orientations). However, at intermediate field values (i.e., $F \sim 5 \times 10^5 - 2 \times 10^6$ V cm^{-1}) the mobility is anisotropic, with larger mobilities in the transverse direction to the average polymer orientation (see Fig. 4.15). This behaviour is attributed to predominantly LGSs to LGSs and hence inter-chain transitions at low fields, while LGSs to QESs and hence intra-chain transitions compete at higher fields (see Fig. 4.16). This prediction

is a potentially key experimental observable that distinguishes this model from simpler lattice models.

The role of disorder is subtle. At low fields (i.e., in the normal Marcus regime), increasing disorder significantly decreases the mobility, because (i) the variation in activation energies is larger than the driving force and (ii) the localisation lengths and hence hopping distances are shorter. However, at higher fields (i.e., in the inverted Marcus regime), increasing disorder slightly increases the mobility, because (i) the increase in reorganisation energy (because of the decrease in localisation length) with disorder pushes the inverted Marcus regime to higher fields and (ii) increased disorder broadens the density of states (see Figs. 4.9 and 4.10).

Using structural parameters derived from MD simulations[144] in the model leads to charge mobility values that are in quantitative agreement with experimental measurements. The model therefore agrees with experimental observations with no adjustable parameters (see Fig. 4.17). Notably, charge mobility is significantly lower in the results obtained using this parameter set. This highlights the fact that the higher bulk polymer density of the initial parameters, as shown in Section 4.4, must be the primary reason for the relatively high charge mobilities observed.

Model Improvements

This model could be further improved in a number of ways. First, in the model presented, quasi-extended states are assumed to relax effectively instantaneously into localised states. According to Mannouch and Barford,[108] however, exciton relaxation in PPV systems is fast, but not instantaneous. Similar treatment of QESs to LGSs relaxation in the framework of time-evolving block decimation (TEBD) could provide a better understanding of the time scale and nature of the charge relaxation process, as well as identifying potential QESs to QESs transitions. The

instantaneous relaxation present in the current model is not expected to result in unphysical displacement (and therefore charge migration), since this relaxation process has been confirmed to take place, associating a finite timescale with this process would be expected to reduce overall charge mobility, and hence bring the simulation results closer to experimental values.

Second, the intramolecular transfer process could be more accurately modelled through studying single polymer chains, examining charge motion along the chain as a consequence of Brownian fluctuations in the torsional motion of the chains. As will be shown in the following chapter, this also causes adiabatic "crawling" motion along the chain.[102, 107].

Finally, improving the accuracy of transition rates is also possible. This work used the high temperature limit ($k_B T \gg \hbar\omega$ for all normal modes) of Marcus theory. While this conditions is not strictly valid, it is a common approximation made in mobility studies in the literature, and was therefore chosen for suitable comparison. The rates could therefore be improved within the framework of Marcus theory, by using the expressions described in Chapter 2, incorporating the appropriate Franck-Condon factors. Going beyond Marcus theory is another option. As already mentioned beforehand, the reduction in transition rates in the inverted regime can be overstated by Marcus theory, as nuclear quantum mechanical effects, such as those of tunnelling, can significantly increase transition rates.[158] The improvement of the current model would be possible through incorporating transition rate models that account for such effects.[159]

Acknowledgement of Contributions

The simulation program used in this chapter benefitted from the initial coding efforts of former members of the Barford research group, Alice Grout-Smith and

Jessica Ellen Poole. The initial program code was then debugged, fixed, amended and expanded in functionality by me.

5

Charge Dynamics Induced by Torsional Fluctuations

5.1 Introduction

Results from the previous chapter examined charge migration at the 'bulk' scale, assuming a frozen energetic landscape for the hopping charge transfer events to take place in. The simulations incorporating quasi-extended acceptor states highlight the important role of higher energy, delocalised states, as well as the increased portion of transitions occurring intramolecularly within the charge transfer process. The natural progression from these results was to assess the dynamics of charge excitations at a quantum level. In this chapter, the intramolecular process is explored through the evolution of the excitation induced by Brownian fluctuations of the torsional angles in poly(p-phenylene) polymer (PPP) chains. The electronic Hamiltonian is solved using the TEBD approach introduced in Chapter 3, while the nuclear degrees of freedom are evolved using the integration of the Langevin equation, with the two dynamics linked through the Ehrenfest scheme. This approach is assumed to realistically represent the random motion effects in bulk polymer and solvated systems, where collisions lead to uncorrelated displacements of the individual chain segments. Additionally, simulations incorporating quantum

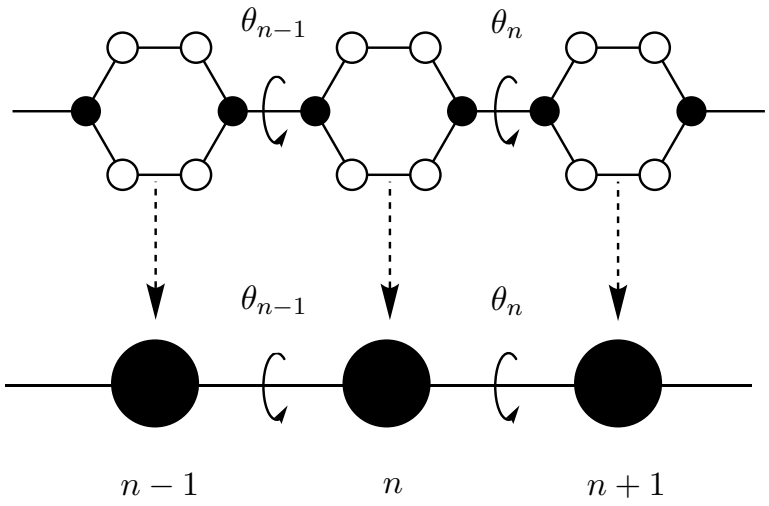


Figure 5.1: The coarse-graining of PPP to a linear chain of 'sites'. The p_z atomic amplitudes on the phenyl ring are $1/\sqrt{3}$ for filled circles and $-1/\sqrt{12}$ for unfilled circles. $\theta_n = (\phi_{n+1} - \phi_n)$ is the torsional angle of the nth bond, where ϕ_n is the rotational angle of the nth ring with respect to the molecular axis.

mechanical corrections to the torsional modes are also presented. While the additional computational cost of including such corrections test the limits of the simulation model, they corroborate the findings of the Ehrenfest simulations. This model displays a range of competing physical effects – coupling the electronic degrees of freedom to the slow torsional motion causes localisation by self-trapping, forming Landau-type polarons. Simultaneously, the fluctuations in torsional angles lead to changes in the off-diagonal elements of the system Hamiltonian, leading to the dynamics of the polaron, while also acting as a source of disorder that localises the wavefunction along the polymer chain via Anderson localisation. The interplay of these effects lead to the dynamics examined in this chapter. The polymer systems incorporate the periodic boundary condition implementations detailed in Chapter 3, but links to the open boundary systems are shown at the beginning, especially to highlight the limitations of these systems in long simulations.

5.1.1 Model Hamiltonian

Similarly to the approach in Chapter 4, the polymer chain is modelled as a chain of coarse-grained sites. This is illustrated in Fig. 5.1 for the PPP system considered in this work. The charge-roton Hamiltonian for the periodic boundary condition (PBC) PPP model system reads

$$\hat{H} = \sum_{n=1}^{N} \epsilon_n \hat{a}_n^\dagger \hat{a}_n + \sum_{n=1}^{N} J(\theta_n) \hat{T}_{n,n+1} + \sum_{n=1}^{N} \left(\frac{K_{\text{rot}}}{2} (\Delta\phi_n)^2 + \frac{L_n^2}{2I} \right), \tag{5.1}$$

where ϵ_n represent the uniform on-site energy terms, $\hat{a}_n^\dagger/\hat{a}_n$ are the charge excitation creation/annihilation operators in the coarse-grained site basis, and

$$\hat{T}_{n,n+1} = \left(\hat{a}_n^\dagger \hat{a}_{n+1} + \hat{a}_{n+1}^\dagger \hat{a}_n \right) \tag{5.2}$$

is the symmetric jump operator. The angle-dependent transfer integral,

$$J(\theta_n) = J_0 \cos\theta_n \tag{5.3}$$

is expressed as a function of the torsional angle across bond n, θ_n. The torsional angle is defined as the difference between the rotational angles on neighbouring sites,

$$\theta_n = \phi_{n+1} - \phi_n. \tag{5.4}$$

Assuming small angular displacements from equilibrium, ϕ_n^0,

$$J(\theta_n) \simeq J_0 \cos\theta_n^0 - J_0 \sin\theta_n^0 \times (\Delta\phi_{n+1} - \Delta\phi_n). \tag{5.5}$$

Introducing dimensionless variables

$$\tilde{\phi} = (K/\hbar\omega)^{1/2} \phi \tag{5.6}$$

$$\tilde{L} = (\omega/\hbar K)^{1/2} L, \tag{5.7}$$

using Eq. (5.5) and ignoring the uniform on-site energy terms, Eq. (5.1) becomes

$$\hat{H} = \sum_{n=1}^{N} \left[J_0 - \hbar\omega A(\theta_n^0)(\Delta\tilde{\phi}_{n+1} - \Delta\tilde{\phi}_n) \right] \hat{T}_{n,n+1} + \frac{\hbar\omega}{2} \sum_{n=1}^{N} \left((\Delta\tilde{\phi}_n)^2 + \tilde{L}_n^2 \right), \quad (5.8)$$

where

$$A(\theta_n^0) = \frac{J_0 \sin\theta_n^0}{(\hbar\omega K_{\mathrm{rot}})^{1/2}} \quad (5.9)$$

is the dimensionless charge-roton coupling constant. Notably, $\hbar\omega$ now represents the energy of the roton, also highlighted in Table 5.1. This is different from the use of $\hbar\omega$ in Chapter 4.

In order to model the system with open boundary conditions (OBC), the Hamiltonian in Eq. (5.8) the transfer term between the end sites, 1 and n, is removed, but it is otherwise unchanged.

As outlined in Chapter 3, the quantum mechanical system is represented in the MPS formalism, and the time-dependent Schrödinger equation is solved for the charge via

$$|\Psi_{\mathrm{MPS}}(t+\delta t)\rangle = \exp\left(-\mathrm{i}\hat{H}\delta t/\hbar\right) |\Psi_{\mathrm{MPS}}(t)\rangle . \quad (5.10)$$

The dynamics is implemented within the TNT Library,[181, 182] and is solved using the time-evolving block decimation (TEBD) scheme,[179, 180] which is coupled with a classical evolution of the angular displacements according to the Ehrenfest equations of motion. Periodic boundary conditions were implemented in the TNT library as part of this project, as described earlier.

5.1.2 Landau Polarons

Anderson localisation was previously described as emerging in disordered system as a scattering phenomenon. The other type of localisation considered is through the formation of Landau polarons, as a consequence of coupling between the electronic

degrees of freedom and the slow nuclear (in this case, rotational) motion self-trapping the particle wavefunction. To understand this phenomenon, we first look at the the dimensionless torque on each monomer,

$$\begin{aligned}\Gamma_n^{\text{syst}} &= -\frac{\partial\langle\hat{H}/\hbar\omega\rangle}{\partial\Delta\tilde{\phi}_n} \\ &= -\Delta\tilde{\phi}_n + \lambda_n,\end{aligned} \tag{5.11}$$

where

$$\lambda_n = A_{n-1}\langle\hat{T}_{n-1,n}\rangle - A_n\langle\hat{T}_{n,n+1}\rangle \tag{5.12}$$

is the torque exerted by the charge, while the first term in Eq. (5.11) originates from the harmonic force. Equilibrium angular displacements in the charged state are given by the equilibrium condition

$$\Gamma_n^{\text{syst}} = 0, \tag{5.13}$$

or equivalently,

$$\Delta\tilde{\phi}_n^{\text{eq}} = \lambda_n. \tag{5.14}$$

In the staggered polymer configuration considered in this work, where the consecutive monomer displacements satisfy $\theta_{n+1} = -\theta_n$ in the neutral state, the equilibrium displacement in the continuum limit can be written as[109]

$$\Delta\tilde{\phi}_n^{\text{eq}} \sim \rho_n \times (-1)^n, \tag{5.15}$$

where ρ_n is the charge density, given by the continuum limit solution

$$\rho_n = \left(\frac{\kappa}{2}\right)\text{sech}^2\kappa(n - n_0) \tag{5.16}$$

and $\kappa = A^2\hbar\omega/4J$. The large-polaron limit is $\kappa^{-1} \gg 1$, implying a sufficiently small electron-phonon coupling. The functional form of the solution confirms that the

particle is self-trapped and self-localised as a Landau polaron with,

$$E_r = \frac{J}{12}\left(\frac{\hbar\omega}{J}\right)^2\left(\frac{A^2}{2}\right)^2. \tag{5.17}$$

being the reorganisation energy in the continuum limit.[128, 129, 209] The polaron reorganisation energy is the emergent low-energy scale from Eq. (5.8), so $T_r = E_r/k_B$ serves as a convenient temperature scale for the low temperature dynamics, and will be used in the following discussion. The classical, Landau polaron is rigorously valid in the limit that $\hbar\omega/J \to 0$, as then the oscillators respond infinitesimally slowly to the charge dynamics so that the polaron effective mass diverges.[121] The centre of the polaron, n_0, is determined by disorder and as will be shown later, when the disorder is dynamical, n_0 varies with time, implying polaron dynamics.

5.1.3 Ehrenfest and Langevin Dynamics

The classical angular displacements, $\Delta\phi_n$, are evolved through the Ehrenfest equations of motion,

$$\frac{\mathrm{d}\Delta\tilde{\phi}_n}{\mathrm{d}\tilde{t}} = \tilde{L}_n \tag{5.18}$$

and

$$\frac{\mathrm{d}\tilde{L}_n}{\mathrm{d}\tilde{t}} = \Gamma_n^{\mathrm{syst}} - \tilde{\gamma}\tilde{L}_n + R_n(t), \tag{5.19}$$

where $\tilde{t} = \omega t$ and $\tilde{\gamma} = \gamma/\omega$ is a dimensionless friction coefficient. The rotational motion of the monomers in the polymer chain is modelled to follow Langevin dynamics, as introduced in Chapter 2, using the integration scheme detailed in Chapter 3. The random torques, $R_n(t)$, model the role of temperature, originating from the Brownian motion of solvent molecules for a polymer system in solution.

They are uncorrelated in space and time, and independent of the systematic torque, $\Gamma_n^{\text{syst}}(t)$. By the fluctuation-dissipation theorem they satisfy[34]

$$\langle R_n(0)R_m(t)\rangle = 2\tilde{\gamma}\left(\frac{k_BT}{\hbar\omega}\right)\delta_{mn}\delta(\tilde{t}). \tag{5.20}$$

The stochastic forces therefore follow a Gaussian distribution with a standard deviation of

$$\sigma_R = \left(\frac{2\tilde{\gamma}k_BT}{\hbar\omega\Delta\tilde{t}}\right)^{\frac{1}{2}}. \tag{5.21}$$

Without polaronic coupling, the Brownian fluctuations and random forces would result in a random distribution of angular displacements, whose variance satisfies the principle of equipartition,

$$\langle\Delta\tilde{\phi}^2\rangle = \frac{k_BT}{\hbar\omega}. \tag{5.22}$$

The fluctuations in the angular displacements result in off-diagonal disorder in the model Hamiltonian shown in Eq. (5.8) and would cause localisation of the wavefunction through Anderson localisation at high temperatures ($T > T_r$).

5.1.4 Relaxation

As an initial test of the simulation algorithm, relaxation (evolution at $T = 0$) behaviour was examined, with OBC and PBC system differences being of particular interest. The time evolution was initiated from the lowest energy eigenstate of the OBC exciton Hamiltonian, i.e., a sinusoidal state. Under these conditions, the system is expected to relax into a self-localised polaron state.[128] This result was confirmed through a Hellmann-Feynman (H-F) minimisation routine, whose results are shown in Fig. 5.2 for 50 site chains. The size (participation number, PN) of the polaron state is ~ 8.9, and its shape follows Eq. (5.16). This polaron size is well converged at a system size of ~ 30 sites, as shown in Fig. 5.3. The H-F solver

iteratively finds the equilibrium angular displacements using the torque expression in Eq. (5.11), using the equilibrium condition of $\Gamma_n^{\text{syst,eq}} = 0$.

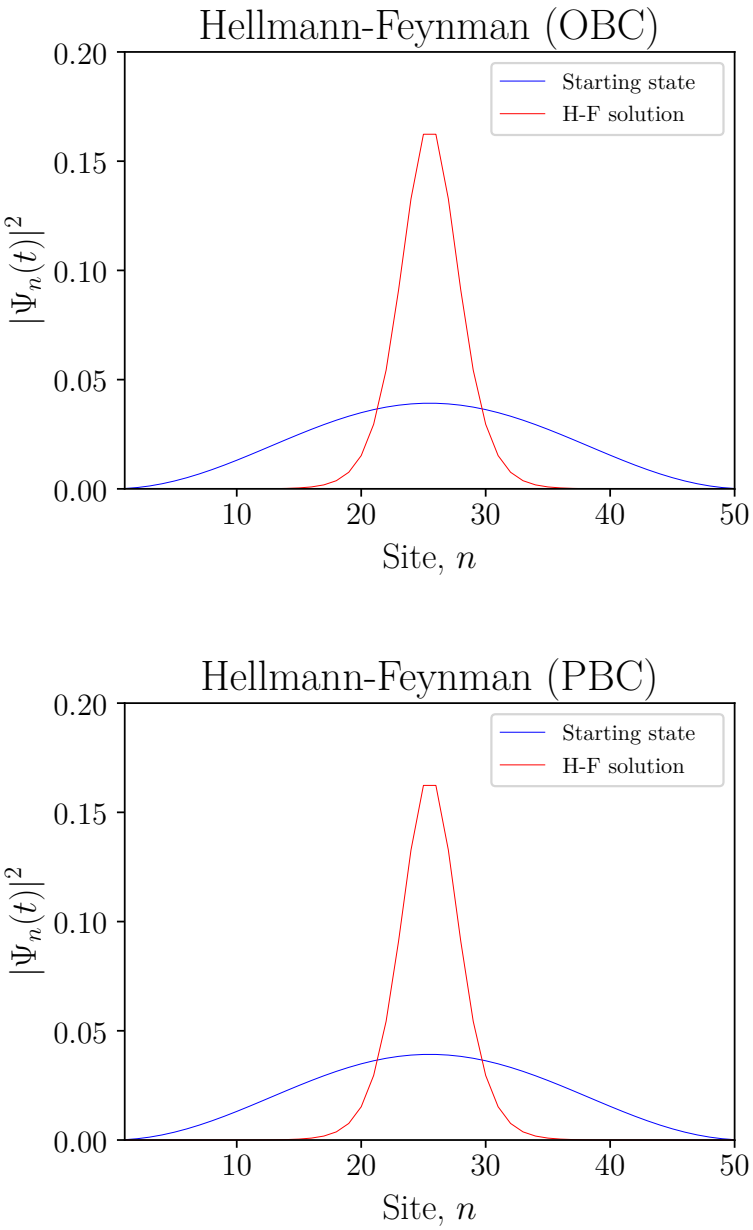


Figure 5.2: Hellmann-Feynman minimised solution of the system Hamiltonian at $T = 0$, illustrating a Landau polaron. The solutions for open (top) and periodic (bottom) boundary conditions are identical.

Using the TEBD-Ehrenfest program, at $T = 0$, OBC and PBC time evolution from an initial sinusoidal starting state, the lowest eigenstate of the OBC system,

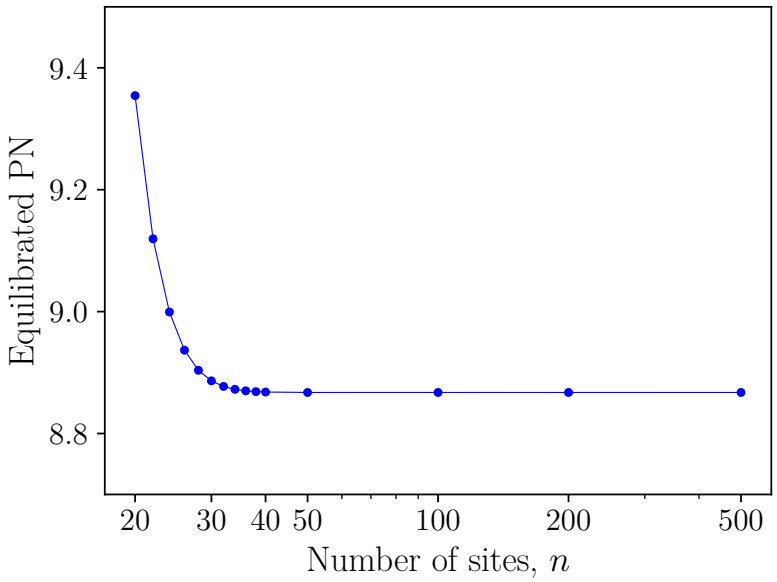


Figure 5.3: The localisation length (as measured by the participation number) of the Hellmann-Feynman minimised solution of the system Hamiltonian at $T = 0$, for a variety of chain lengths.

both result in the formation of a localised polaron state. The OBC system relaxes fully onto the H-F polaron state, while the PBC system approaches this solution but fails to fully converge to it. This is shown in Fig. 5.4 for various chain lengths. These differences can be attributed to the fact that the sinusoidal starting state is not an eigenstate of the PBC Hamiltonian, and therefore additional excited state contributions need to be dissipated, which the Ehrenfest approach fails to achieve completely, as discussed in Chapter 2. This problem is revisited later in the chapter. For the sake of consistent comparison, the simulations of charge diffusion under the influence of Brownian fluctuations, at $T > 0$, were initiated in the fully relaxed, H-F polaron state for all subsequent simulations.

5.1.5 Simulation Parameters

As a result of the insights about the relaxation behaviour of the system, a system size of $N = 50$ sites (i.e., 50 coarse-grained monomers) was chosen for the dynamics

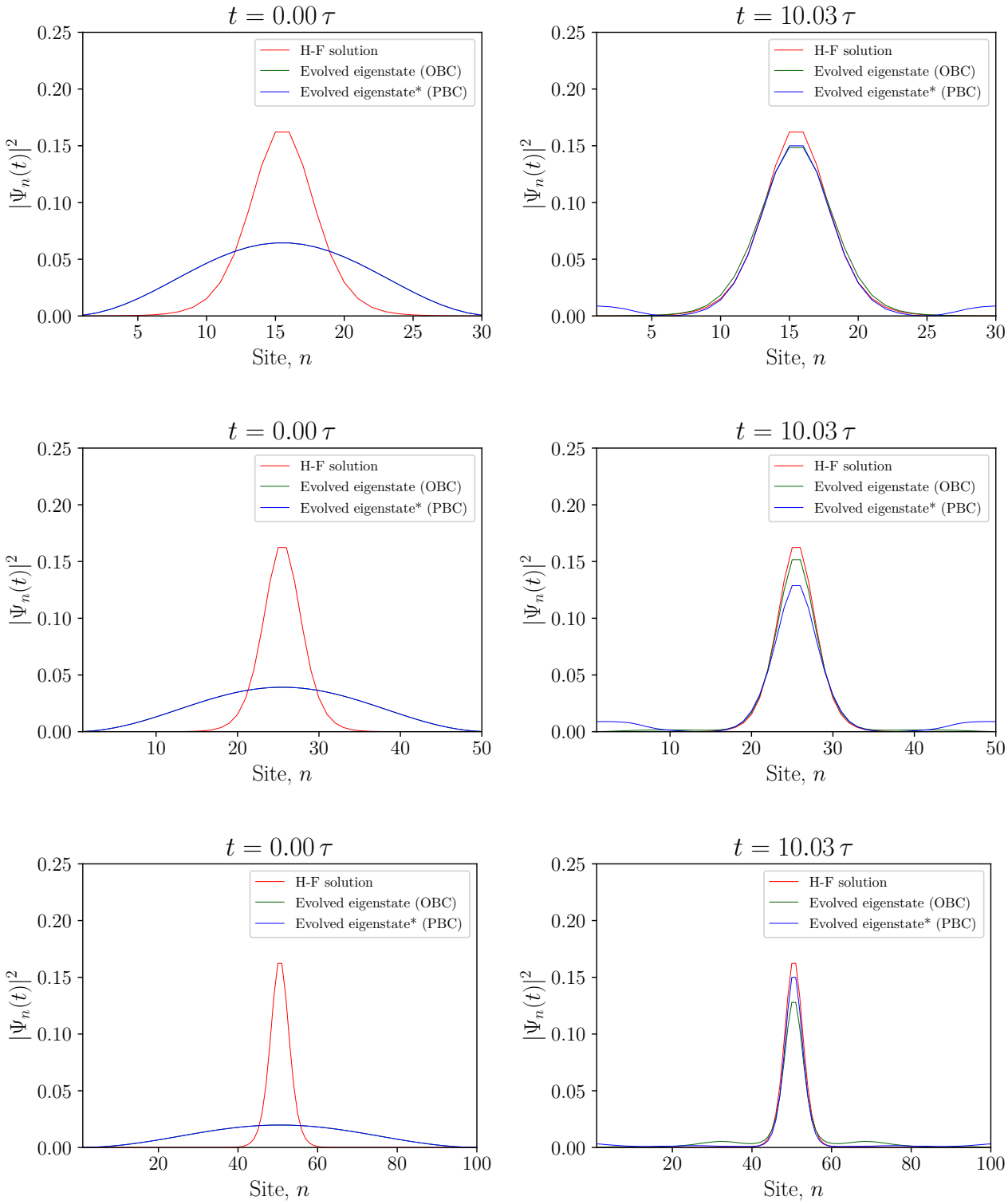


Figure 5.4: Relaxation results for systems of 30 (top row), 50 (middle row) and 100 (bottom row) monomers. τ is the monomer rotational period.

simulations, as this represents a good balance between using a suitable large system while keeping the computational effort manageable. The parameters used in the simulations of charge-polaron dynamics in PPP are listed in Table 5.1. Periodic boundary conditions were used for the simulations and ensemble averaging over at least 25 different trajectories was performed at each temperature. The dynamics in each instance are initiated in a localised polaron state, obtained via a H-F minimisation routine, as highlighted above. The polaron reorganisation energy is obtained numerically via the H-F iterator. The simulation time for each trajectory is $\sim 7 \pm 3$ days.

Table 5.1: Parameters[1, 109] used in the simulations of charge-polaron dynamics in PPP.

Roton energy	$\hbar\omega$	$0.02\,\mathrm{eV}$
Charge transfer integral	J_0	$-0.7133\,\mathrm{eV}$
On-site energy (phenylene)	ϵ_n	2.4 eV
Charge-roton coupling constant	A	1.87
Ground state torsional angle	ϕ^0	$\pm 10^\circ$
Rotational force constant	K_{rot}	$0.90\,\mathrm{eV\,rad^{-2}}$
Dissipation coefficient	γ	$10^{12}\,\mathrm{s^{-1}}$
Total simulation time		$300\,\tau$
Rotational period	$\tau = 2\pi/\omega$	$0.2\,\mathrm{ps}$
Charge-polaron reorganisation temperature	$T_r = E_r/k_B$	$\sim 400\,\mathrm{K}$
Quantum dynamics time step	$\delta\tilde{t}$	10^{-4}
Classical dynamics time step		$100\,\delta\tilde{t} = 10^{-2}$

5.1.6 Boundary Effects

The charge dynamics examined in this work manifests in the (partially) localised states migrating along the length of the polymer chains. Over the simulation timescales, this means that while the localisation length is significantly smaller than the length of the chain, the overall displacement over the course of the dynamics can be substantially larger than the chain length, and therefore boundary effects need

to be considered. In open boundary systems, even at low temperatures, where the migration is expected to be the slowest, the edge of the polymer chain is regularly reached. This is shown using the charge densities in Fig. 5.6 and through centre of mass positions Fig. 5.5. Noticeably, the polaron 'bounces' off the edge of the chain upon approaching it and returns towards the centre. This can also be accompanied by a distortion of the shape of the polaron, which could lead to an unphysical drop in localisation length, an example of which can be seen in Fig. 5.5. These issues are not observed for PBC systems, where the polaron can freely migrate across the chain boundary, as will be shown later. Due to this limitation of OBC systems, only periodic boundaries are considered for the remainder of this work.

5.2 Polaron Dynamics Results

There are two types of dynamics presented below, both falling in the $T < T_r$ regime. At the lowest temperatures, the system evolves quasidiabatically, resulting in an activationless diffusive, crawling motion along the polymer chain. At higher temperatures, but still below T_r, the population of higher-lying states is observed, through an activated transfer mechanism, corresponding to hopping between diabatic states.

5.2.1 Low Temperature Polaronic Crawling

The dynamics in the low temperature regime, defined as $T \ll T_r$, follows a quasidiabatic evolution in the lowest energy diabatic state. This leads to a 'crawling' displacement of the polaron along the polymer chain, and therefore to a net migration of charge. The displacement of the polaron is determined by tracking the centre of mass, i.e., $\bar{n}(t) = \sum_n n\rho_n(t)$, over time. Snapshots of the evolution of the polaron density as a function of time are shown in Fig. 5.7. The polaron

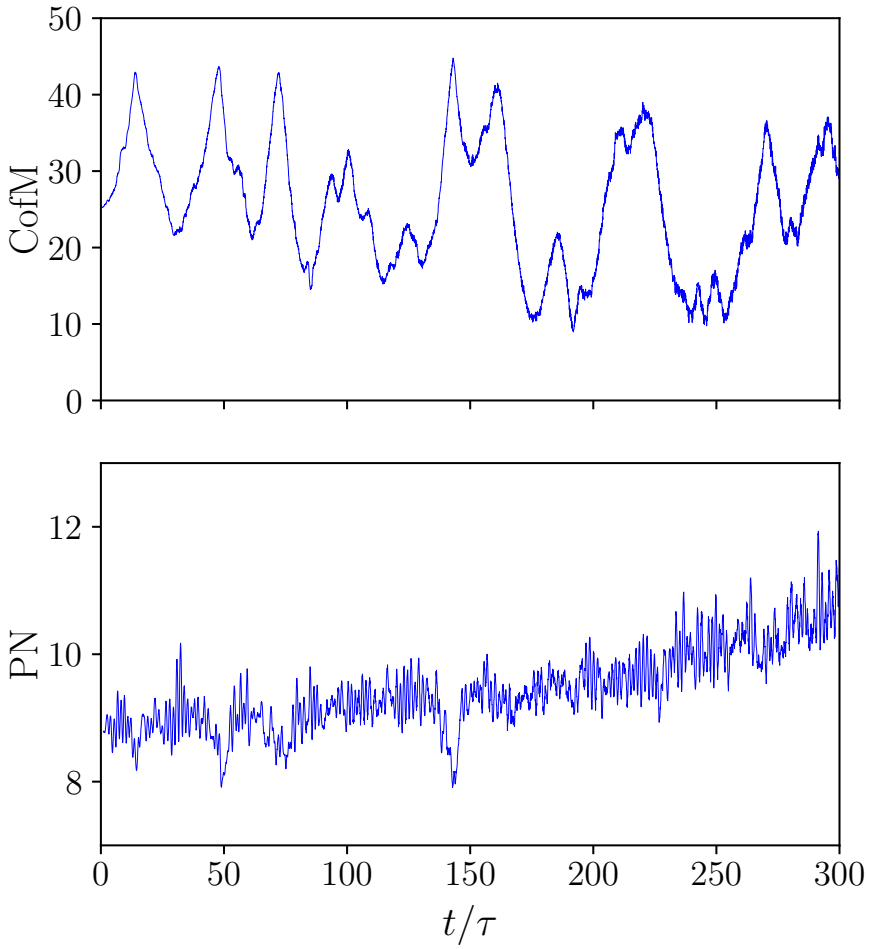


Figure 5.5: Centre of mass position (top) and localisation length (bottom) of a sample trajectory of the OBC system at $T = 0.024\,T_r$. τ is the monomer rotational period. Unphysical dips in localisation length upon reaching the chain boundaries are particularly pronounced at $t \approx 50\,\tau$ and $t \approx 145\,\tau$.

is seen to migrate across the chain boundaries, free from the boundary effects highlighted earlier, retaining its shape throughout. The localisation length, defined by the participation number, remains small throughout the simulations, as shown in Fig. 5.8 for individual trajectories, and in Fig. 5.17 for trajectory ensemble averages. The diabatic nature of the evolution is also demonstrated by the absence of energy crossovers between the lowest instantaneous eigenstates of the Hamiltonian (shown in Fig. 5.9), and by considering the overlap of the evolving wavefunction with

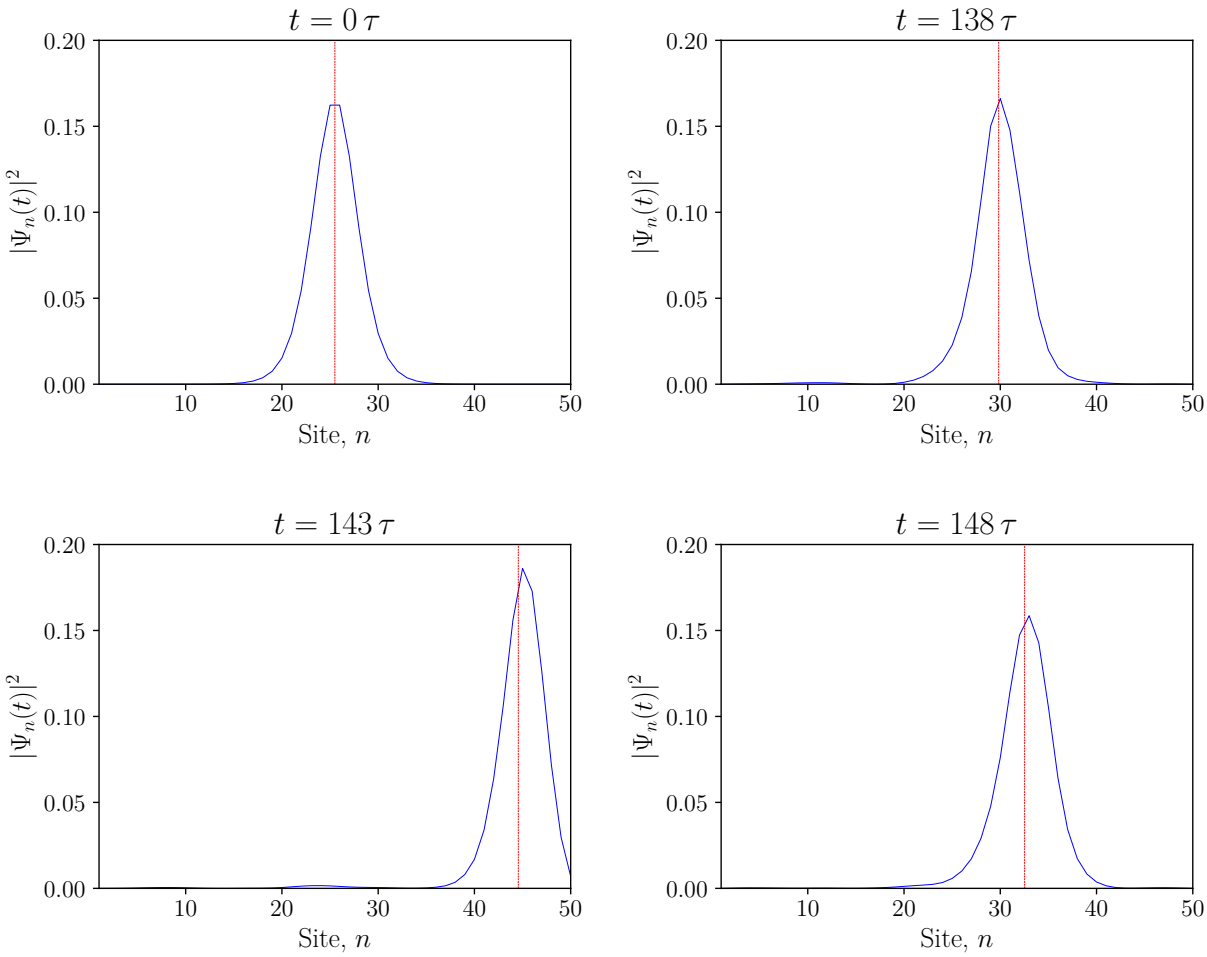


Figure 5.6: Dynamics snapshots at $T = 0.024\,T_r$ in an OBC system. τ is the monomer rotational period. The centre of mass is shown by the red vertical line. The snapshots are from the same trajectory that is shown in Fig. 5.5.

these adiabatic eigenstates, shown in Fig. 5.10.

The displacement of centre of mass positions leads to a net diffusion of the charge. This is visualised through the mean-squared displacement plots in Fig. 5.11. Keeping track of the centre of mass positions across periodic boundaries is achieved by centring the chain indices around the centre of mass position at each time step, and calculating displacements relative to this position. As displacements between consecutive discrete time steps are expected to be small, this approach avoids artificially and unphysically large jumps that would result from the centre of mass

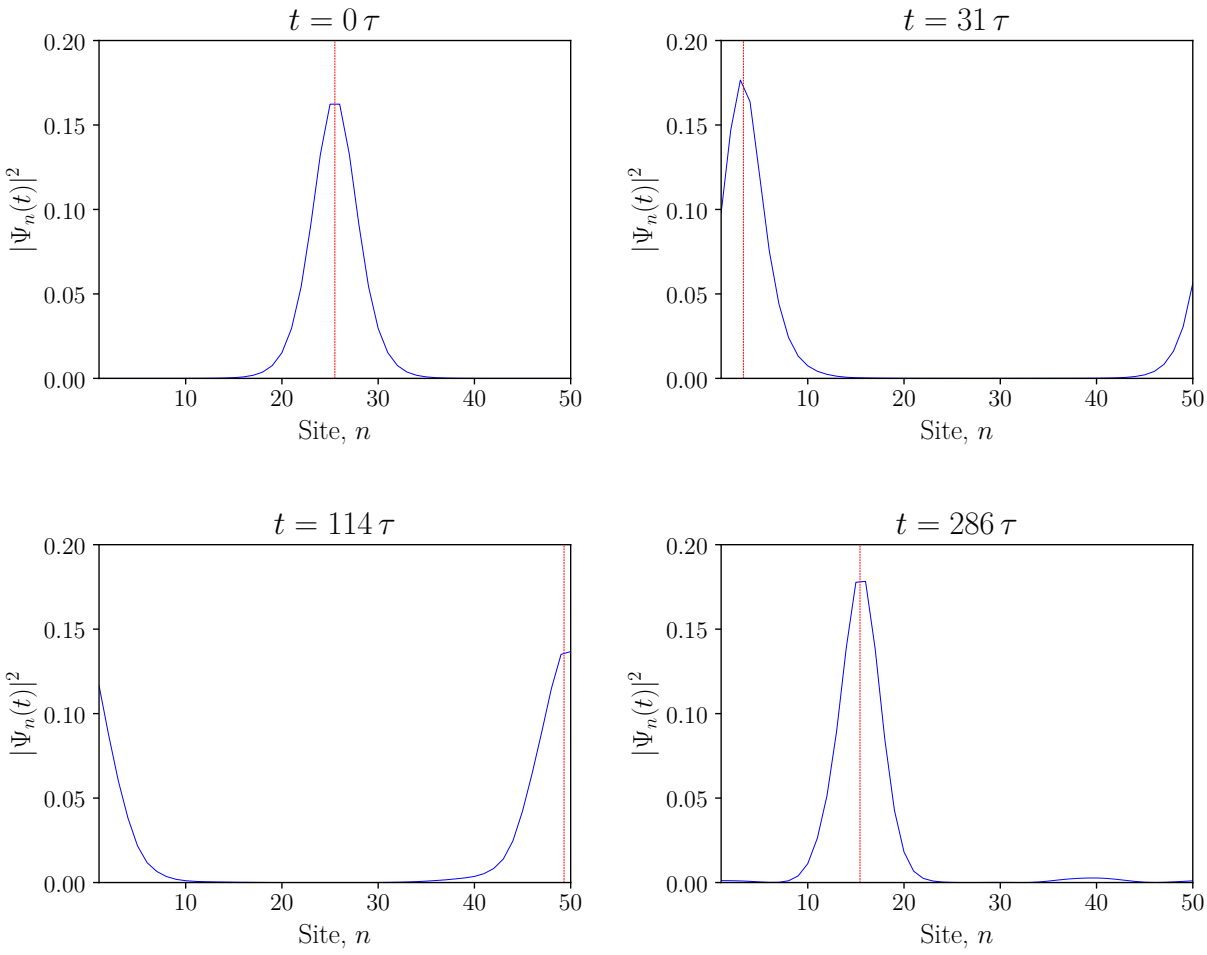


Figure 5.7: Dynamics snapshots at $T = 0.024\,T_r$ in a PBC system. τ is the monomer rotational period. The centre of mass is shown as the red vertical line.

crossing the periodic boundary in real space. The mean-squared displacement, $\langle X^2(t)\rangle$, is calculated as

$$\langle X^2(t)\rangle = \sum_{k=1}^{N_t=t/\Delta t} \left\{\bar{n}\left[k\Delta t\right] - \bar{n}\left[(k-1)\Delta t\right]\right\}^2, \tag{5.23}$$

where Δt is chosen so that small fluctuations around the same physical position on the chain are averaged out. $\Delta t \sim \tau$ was found to give good results. Across all temperature values it is diffusive behavior, *i.e.*, a linear change in the mean-squared displacement over time is achieved after an initial equilibration period of $\sim 100\tau$.

The gradient of the diffusion plots, taken after the initial equilibration, gives

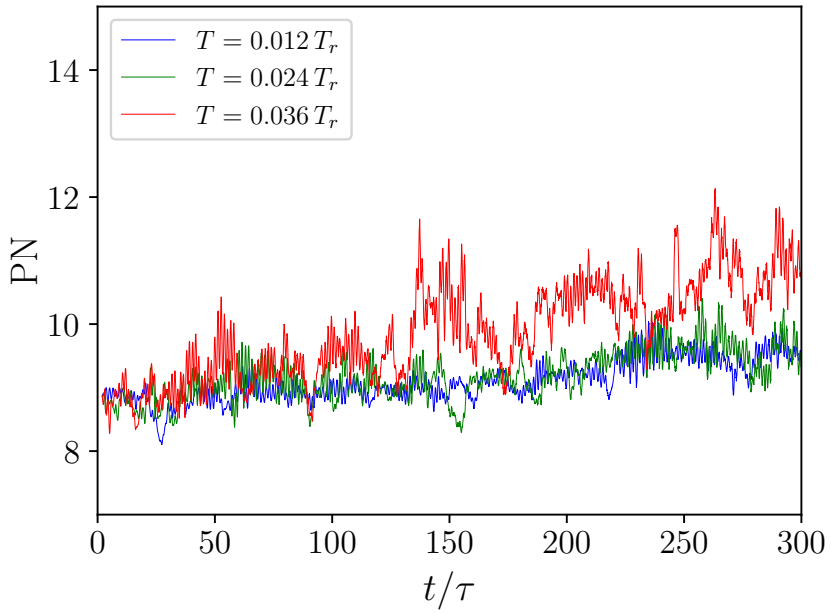


Figure 5.8: Localisation length of the evolving state, $|\Psi(t)\rangle$, as a function of time in the lowest temperature regime, $T \ll T_r$. The curves are smoothed for better legibility.

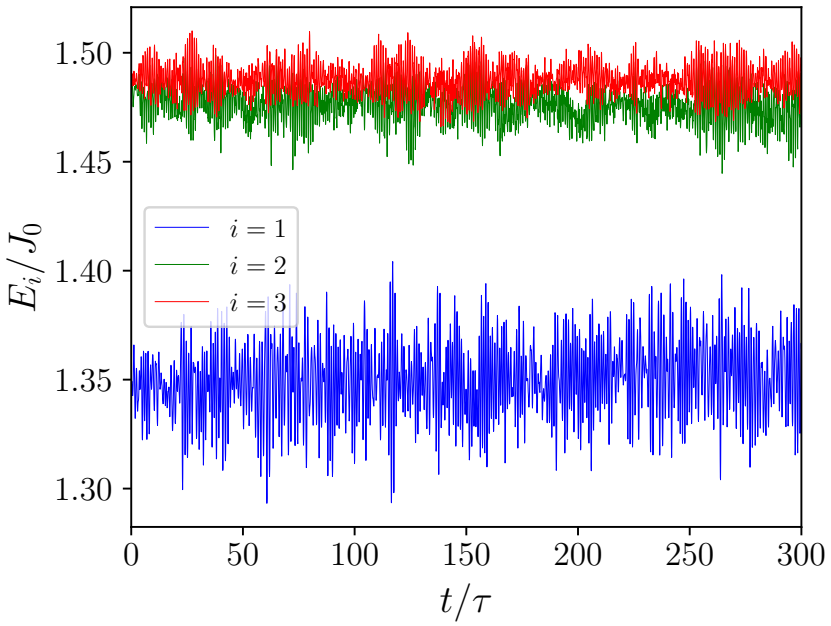


Figure 5.9: Energies of the lowest instantaneous eigenstates as a function of time at $T = 0.024\,T_r$.

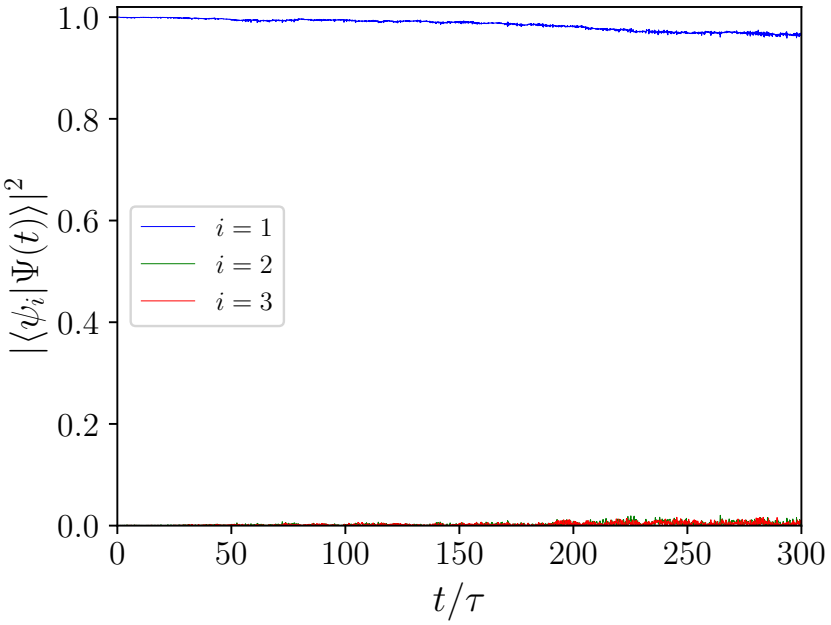


Figure 5.10: Probabilities that the evolving state, $|\Psi(t)\rangle$, occupies an instantaneous adiabatic state, $|\psi_i\rangle$, as a function of time at $T = 0.024\,T_r$.

an estimate of the diffusion constant, D, as

$$D = \frac{1}{2d} \lim_{t\to\infty} \frac{\mathrm{d}\langle X^2(t)\rangle}{\mathrm{d}t}, \tag{5.24}$$

where d is the dimensionality of the system, so $d = 1$ in the case of quasi-1D systems such as the model under investigation. The diffusion constant is expected to be proportional to the temperature for activationless processes, and this is what is observed in the low temperature regime, as shown in Fig. 5.12. These results are in agreement with previous work on this topic.[102, 103, 107, 114]

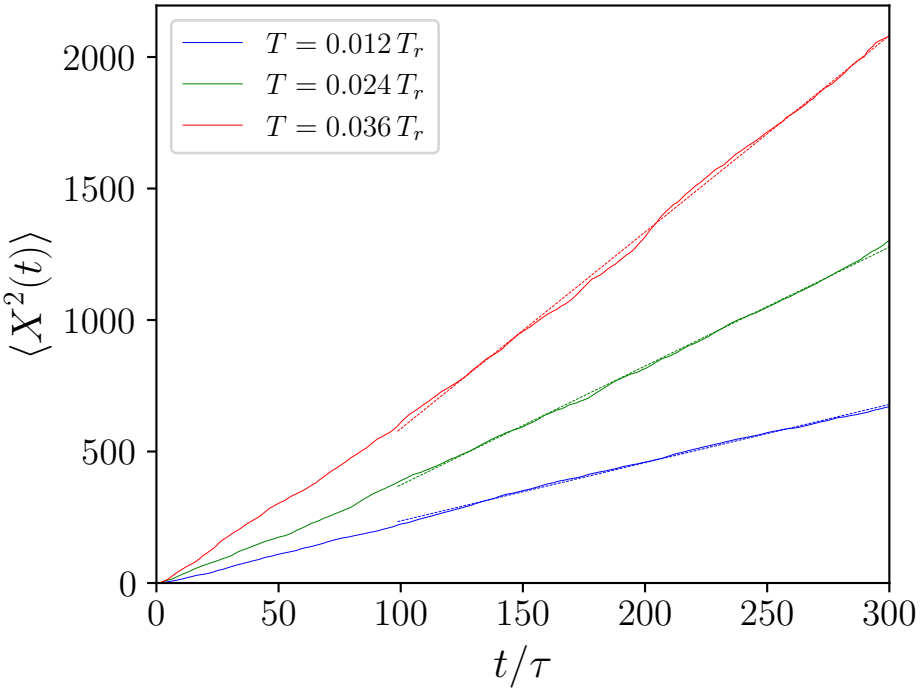


Figure 5.11: Ensemble average of polaron mean-square-displacement as a function of time in the lowest temperature regime, $T \ll T_r$. The dashed lines are linear fits to the data (in solid) taken after an equilibration time of $100\,\tau$.

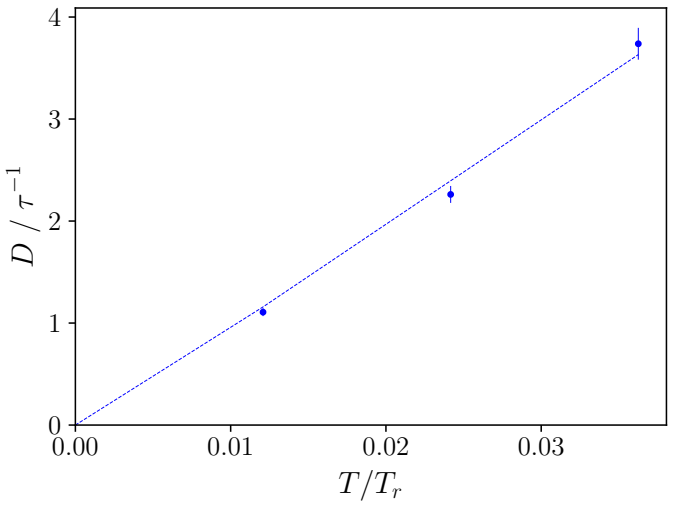


Figure 5.12: Diffusion constant, D, as a function of temperature in the lowest temperature regime, $T \ll T_r$, indicating an activationless process.

5.2.2 Intermediate Temperature Polaronic Hopping

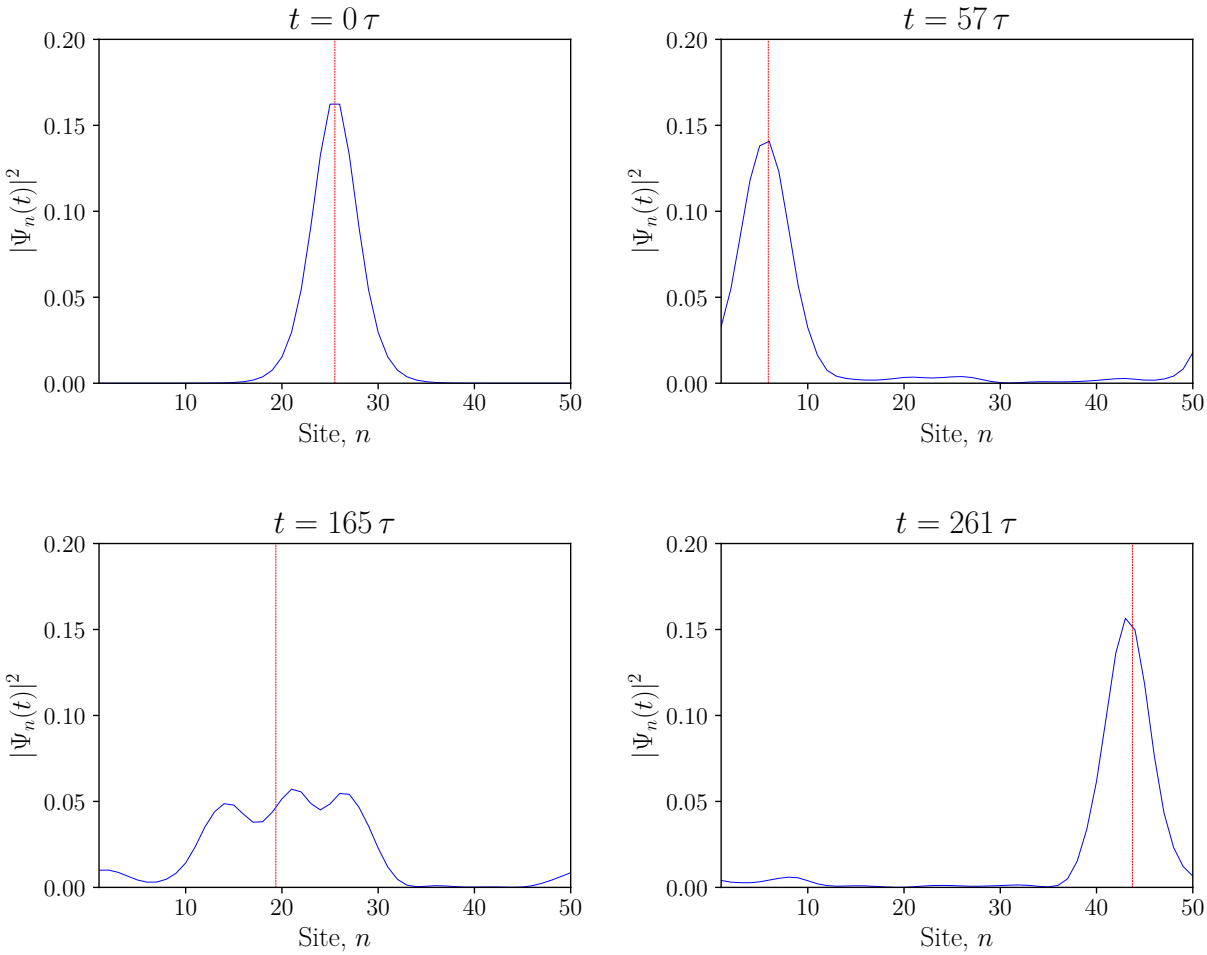


Figure 5.13: Dynamics snapshots at $T = 0.073\,T_r$ in a PBC system. τ is the monomer rotational period. The centre of mass is shown as the red vertical line.

Contrasting with the lowest temperature, quasidiabatic regime, the increased temperature (and therefore larger torsional fluctuations) leads to characteristically different type of dynamics. The evolving state, $|\Psi(t)\rangle$, is no longer confined to a highly localised, low energy state at all times. Snapshots of the dynamics shown in Fig. 5.13 illustrate that the polaron density can become more delocalised at times. The increased localisation lengths are shown in Fig. 5.14 for individual trajectories and in Fig. 5.17 for trajectory ensemble averages. The energies of the instantaneous

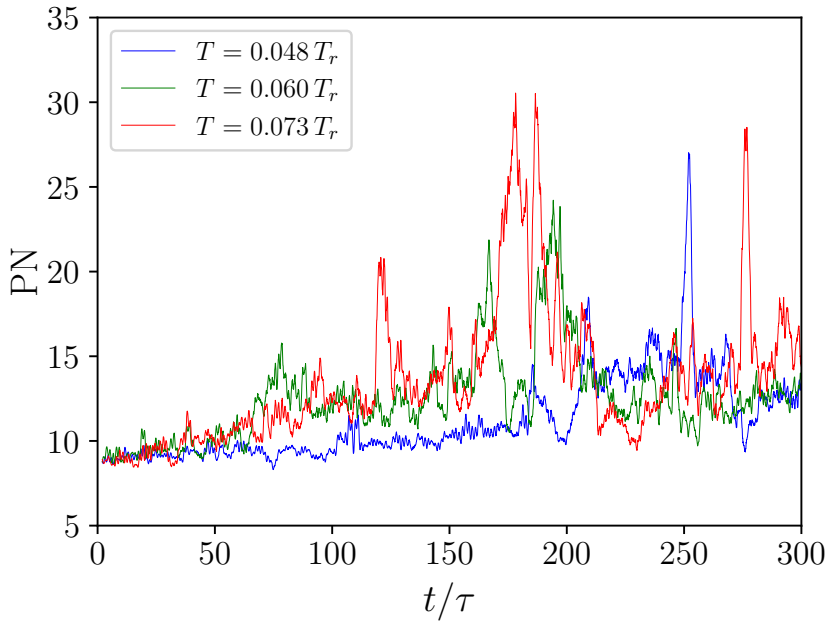


Figure 5.14: Localisation length of the evolving state, $|\Psi(t)\rangle$, as a function of time at different temperatures. Note the increase in PN when $T = 0.073\,T_r$ at $t \sim 170\,\tau$ corresponding to the Landau-Zener transition shown in Fig. 5.18. The curves are smoothed for better legibility.

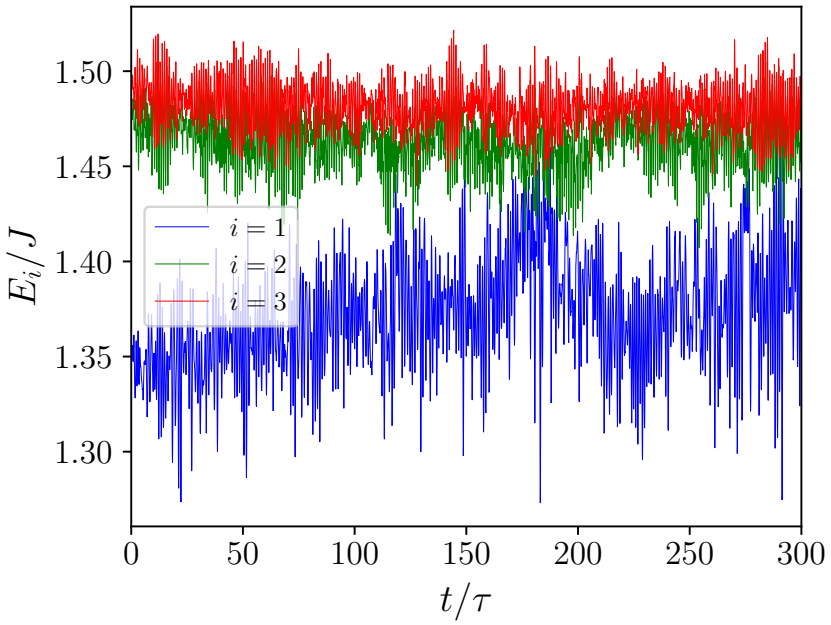


Figure 5.15: Energies of the lowest instantaneous eigenstates as a function of time at $T = 0.073\,T_r$.

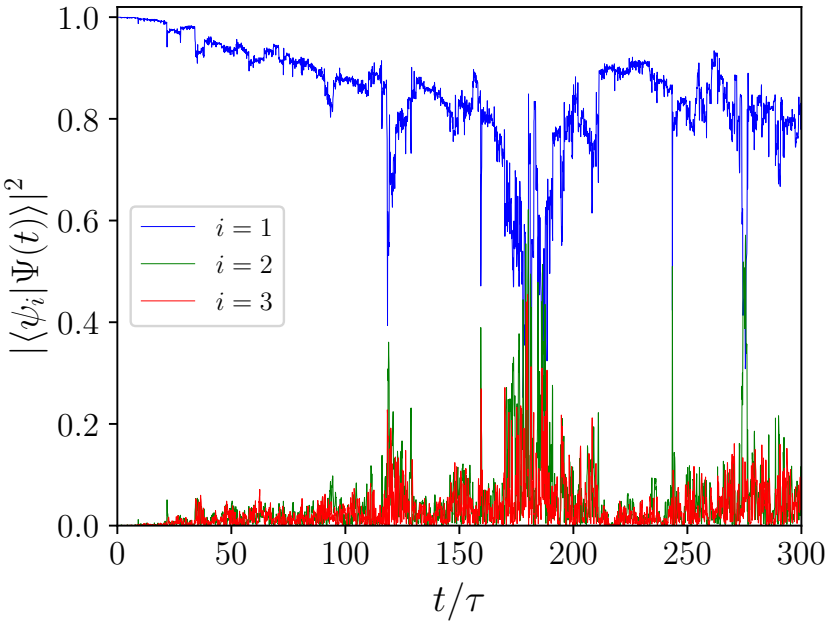


Figure 5.16: Probabilities that the evolving state, $|\Psi\rangle$, occupies an instantaneous adiabatic state, $|\psi_i\rangle$, as a function of time at $T = 0.073\,T_r$. Note that the probabilities of occupying $|\psi_1\rangle$ and $|\psi_2\rangle$ become almost equal at $t \sim 170\tau$ corresponding to the Landau-Zener transition shown in Fig. 5.18.

eigenstates are much closer together, and avoided energy level crossings can be seen in Fig. 5.15. Simultaneously, the occupation probabilities of higher-lying eigenstates increases multiple times throughout the simulations, as shown in Fig. 5.16.

Landau-Zener transitions[34, 145–148] can be observed to take place at the energetic avoided crossing. Figure 5.18 illustrates one such event, through a series of dynamics snapshots. The localisation length, energy and occupation probability plots mentioned above (Figs. 5.14 to 5.16) also contain this specific trajectory, and the transition can be seen near $t \sim 170\,\tau$. Figure 5.18 shows the transition process by overlaying three probability densities: the evolving states, $|\Psi(t)\rangle$, and the two lowest energy eigenstates, $|\psi_1\rangle$ and $|\psi_2\rangle$. $|\psi_1\rangle$ and $|\psi_2\rangle$ show considerable mixing in Fig. 5.18a, with a significantly higher contribution to the linear contribution from $|\psi_1\rangle$. The two adiabatic states are located close together at this stage, centred around

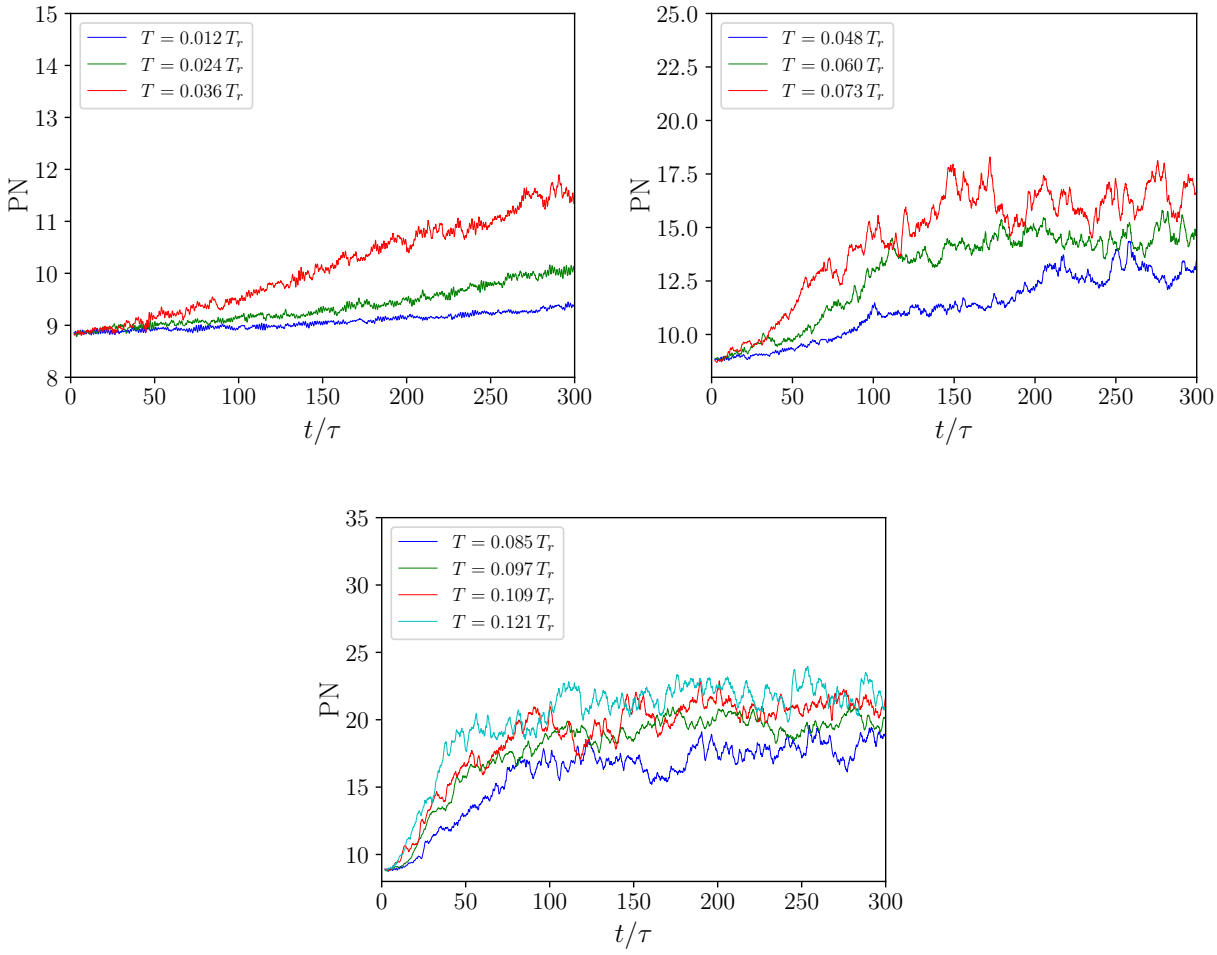


Figure 5.17: Trajectory ensemble averages of the localisation length of the evolving state, $|\Psi(t)\rangle$, as a function of time at different temperatures. The curves are smoothed for better legibility.

$n \sim 15$ and $n \sim 28$ but characteristically appear like independent quasidiabatic states. By contrast, as the transition occurs between Figs. 5.18b and 5.18c, the adiabatic states are each linear combinations of the underlying diabatic states, which is further highlighted in Fig. 5.19. This also applies to the evolving state itself. As the transition event progresses, the probability density of evolving state transfers from the left-hand diabatic state to the right-hand one. Notably, the highest occupation probability remains associated with the lowest adiabatic state, $|\psi_1\rangle$. After the transition, as shown in Fig. 5.18d, the adiabatic states $|\psi_1\rangle$ and $|\psi_2\rangle$ once

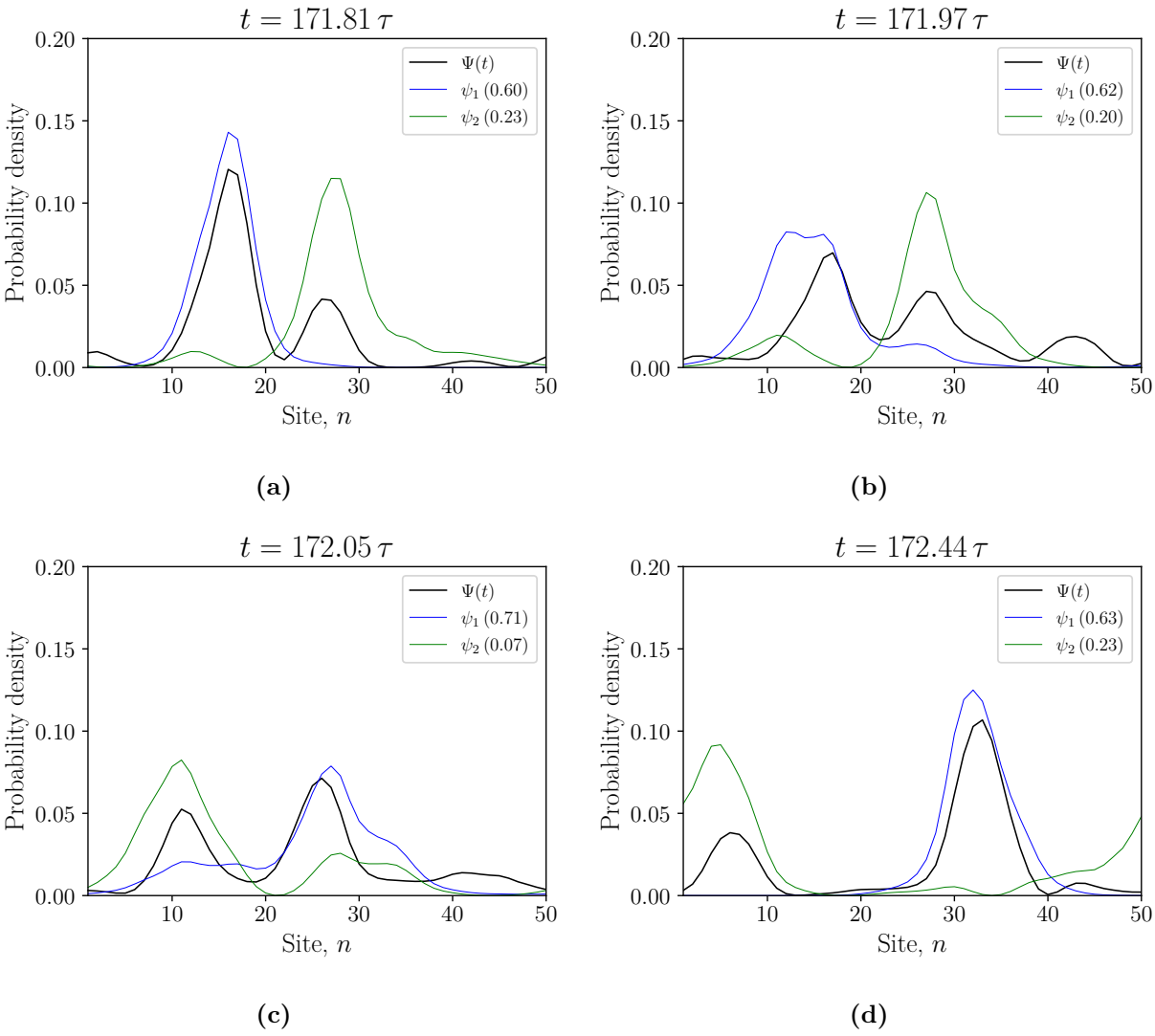


Figure 5.18: Evolution of $|\Psi\rangle$ (black) and the two lowest adiabatic states ($|\psi_1\rangle$ (blue) and $|\psi_2\rangle$ (green)) during a Landau-Zener transition when $t \sim 170\tau$ at $T = 0.073\,T_r$. The curves represent the probability densities. Note that $|\Psi_n|^2 = \rho_n \sim \Delta\tilde{\phi}_n^{\mathrm{eq}} \times (-1)^n$. The occupation probabilities of $|\psi_1\rangle$ and $|\psi_2\rangle$ are shown in the legends, showing that during the transition the system remains predominately in the lower adiabatic state. As described in the text, the transition occurs between panels (b) and (c).

again take the shape of mostly unmixed diabatic states. The overall process therefore shows a 'hopping' transition from one quasidiabatic polaron state to another.

This transition is of a Landau-Zener type, which can be clearly reasoned considering the underlying dynamics. The fluctuations of the angular displacements, $\Delta\tilde{\phi}_n$, alter the energetics of the adiabatic states, significantly destabilising the

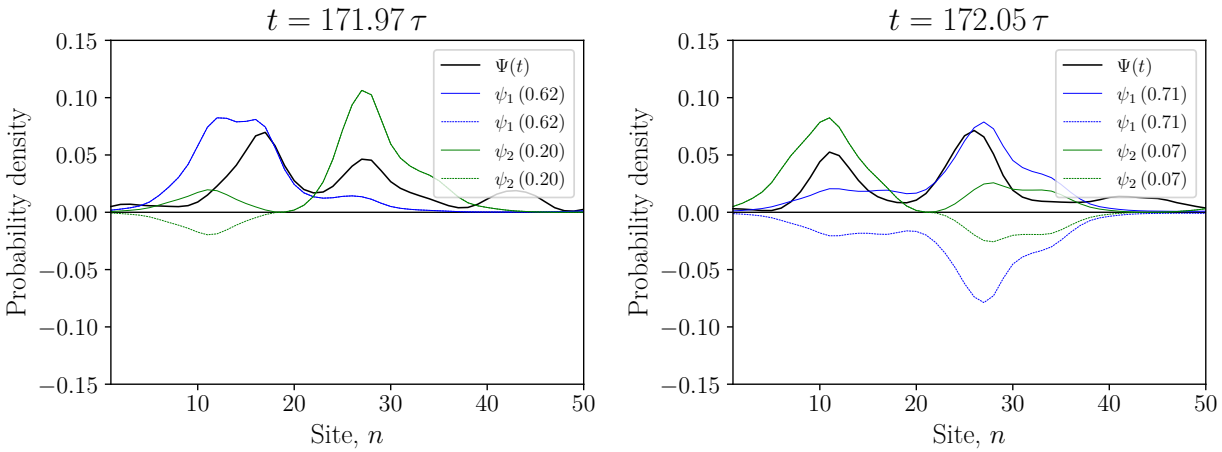


Figure 5.19: Replotted snapshots from Figs. 5.18b and 5.18c, highlighting that the adiabatic states (blue and green) are the positive and negative linear combinations of the diabatic states (black). The signed particle density, $\psi_i|\psi_i|$, of both adiabatic states is shown with dashed lines.

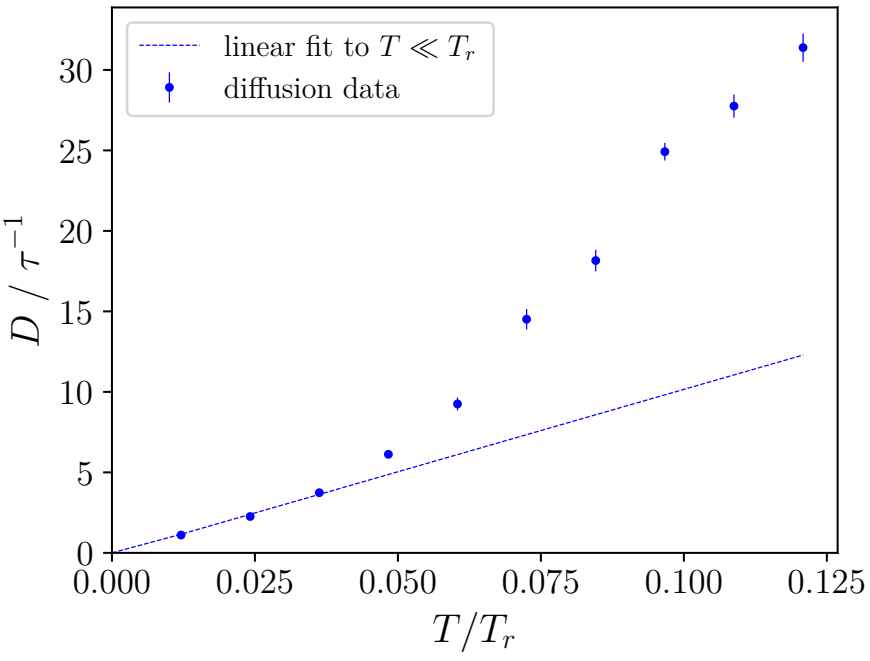


Figure 5.20: Diffusion constant, D, as a function of temperature, indicating a crossover to activated hopping processes at higher temperatures.

lowest lying state which primarily makes up the evolving state. This is evidenced by the increased energy of this state (see Fig. 5.15), as well as making it more

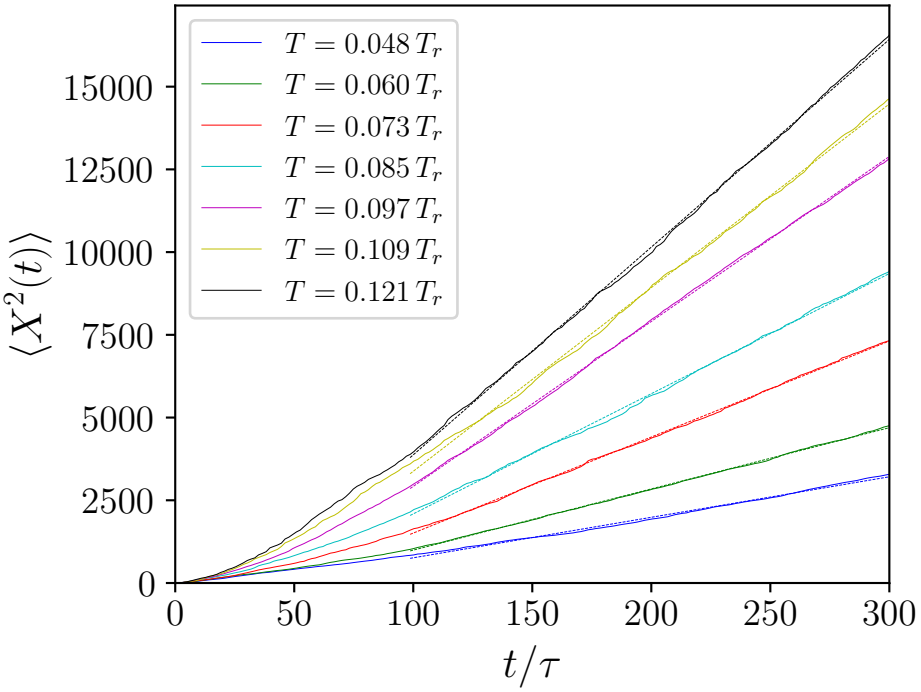


Figure 5.21: Ensemble average of polaron mean-square-displacement as a function of time in the intermediate temperature regime, $T < T_r$. The dashed lines are linear fits to the data (in solid) taken after an equilibration time of $100\,\tau$.

delocalised (see Fig. 5.18b). This change in configuration brings the energy levels of the neighbouring diabatic states close together, enabling the LZ transition. Additionally, given that the charge density, ρ_n, and the angular displacement, $\Delta\tilde{\phi}_n$ are closely linked through Eq. (5.15), Figs. 5.18b and 5.18c show that the angular displacements in the two diabatic states involved are nearly identical, therefore satisfying the matched configuration requirement of a Marcus-type transfer process.

Crucially, the type of transition highlighted above leads to population transfer between different segments of the polymer chain. This in turn results in the displacement of the polaron centre of mass on a faster timescale compared to the quasidiabatic crawling motion seen in the lowest temperature regime. The diffusion constants obtained from the $\langle X^2(t) \rangle$ plots (shown in Fig. 5.21 for the

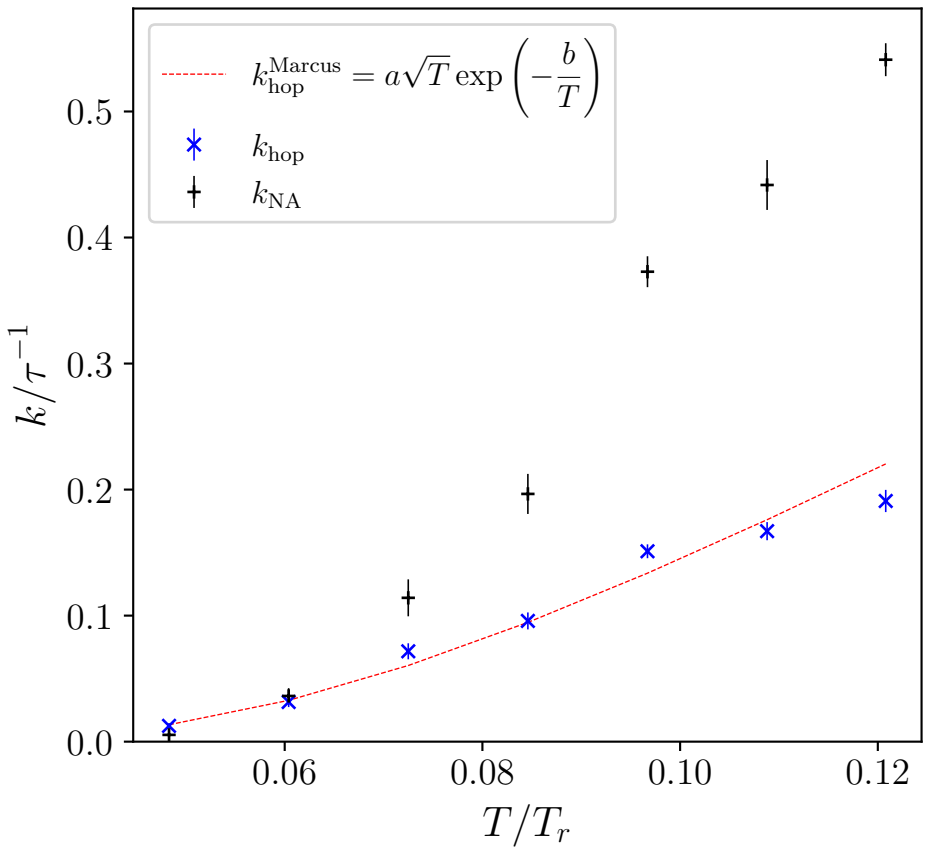


Figure 5.22: Hopping transition rates calculated via Eq. (5.25) using a mean displacement, $\langle \Delta r \rangle = 10$ sites. The rate for nonadiabatic processes, k_{NA}, is defined as the rate at which the probability of the system occupying the lowest adiabatic state $|\psi_1\rangle$ becomes less than 0.5.

intermediate temperature regime), verify this when plotted together with the diffusion constants from the low temperature regime, shown in Fig. 5.20. The linear fit to the low temperature behaviour underestimates the actual diffusion rates in the intermediate temperature regime, which is a result of the displacement through hopping transport observed in this regime.

The quantitative analysis of this additional rate of diffusion is assessed by assuming that the deviation from the linear temperature dependence is a consequence of the hopping transport mode. Assuming that each hop corresponds to a mean displacement of $\langle \Delta r \rangle = 10$, motivated by the fact that a localised polaron state has

PN $\sim$ 10, as well as from the hopping distance shown in Fig. 5.18, the rate of hopping events is

$$k_{\text{hop}} \propto \frac{D_{\text{hop}}}{\langle \Delta r \rangle^2}. \tag{5.25}$$

The resulting rates are plotted in Fig. 5.22. A fit to the Marcus theory rate expression,

$$k_{\text{hop}}^{\text{Marcus}} = a\sqrt{T} \exp\left(-\frac{b}{T}\right), \tag{5.26}$$

where a and b are constants, is also shown. In the same plot, a different definition of transition rate is also evaluated, corresponding to the nonadiabatic processes which are captured through the occupation probabilities of the adiabatic states: each time the occupation probability of the lowest adiabatic state, $|\langle \psi_1 | \Psi(t) \rangle|^2$, dips below 0.5, a nonadiabatic event is recorded, and the frequency of such events over the course of the simulation is calculated.

5.2.3 Corrections from Quantised Rotons

In the results discussed above, the mixed quantum-classical methodology describes the rotational motion and the environment classically, while treating the charge dynamics fully quantum mechanically. As discussed in Chapter 2, this Ehrenfest approach can suffer from improperly describing the energy transfer between classical and quantum subsystems, although the results presented above are in good agreement with previous work in literature, as will be discussed in more details later. Additionally, since the thermal energy of the systems considered falls well below that of $\hbar\omega$, quantum mechanical nuclear effects are expected to have a significant role in the dynamics. In order to further assess the robustness of the approach,

additional calculations were performed where the rotational motion was partially quantised. This method is in line with the work of Barford and Mannouch[109, 210] and the full derivation is presented in Appendix A.

Starting from the Hamiltonian introduced in Eq. (5.8), we can first consider the fully quantum mechanical model where the conjugate variables $\Delta\tilde{\phi}_n$ and $\tilde{L}_n$ are replaced by the quantised variables defined in terms of harmonic oscillator raising and lowering operators, $\hat{b}_n^\dagger$ and $\hat{b}_n$, respectively, as

$$\tilde{L}_n \to \hat{\tilde{L}}_n = \frac{\mathrm{i}}{\sqrt{2}}\left(\hat{b}_n^\dagger - \hat{b}_n\right), \tag{5.27}$$

and

$$\Delta\tilde{\phi}_n \to \Delta\hat{\tilde{\phi}}_n = \frac{1}{\sqrt{2}}\left(\hat{b}_n^\dagger + \hat{b}_n\right) \equiv \hat{B}_n, \tag{5.28}$$

where $\hat{B}_n$ is the dimensionless (quantum) angular displacement. Using these relations, the Hamiltonian becomes

$$\hat{H} = \sum_{n=1}^{N}\left[J_0 - \hbar\omega A(\theta_n^0)(\hat{B}_{n+1} - \hat{B}_n)\right]\hat{T}_{n,n+1} + \hbar\omega\sum_{n=1}^{N}\left(\hat{b}_n^\dagger\hat{b}_n + \frac{1}{2}\right). \tag{5.29}$$

Rather than treating the rotational degrees of freedom entirely quantum mechanically, a more efficient correction scheme is employed as follows. The assumption is that the angular displacement follows

$$\Delta\hat{\tilde{\phi}}_n = \Delta\tilde{\phi}_n^{\mathrm{eh}} + \delta\hat{\tilde{\phi}}_n, \tag{5.30}$$

where $\Delta\tilde{\phi}_n^{\mathrm{eh}}$ denotes the mean-field angular displacement, which follows the classical Ehrenfest equations of motion (Eqs. (5.18) and (5.19)), and $\delta\hat{\tilde{\phi}}_n$ corresponds to the small quantum fluctuations around this mean value. The quantum fluctuations, $\delta\hat{\tilde{\phi}}_n$, therefore come from the solution of the effective Hamiltonian, which the quantum

subsystem is subjected to during the TEBD dynamics, which we can write as:[109]

$$\begin{aligned}\hat{H}_{\text{eff}} = &\sum_{n=1}^{N}\left[J_n^0 - \hbar\omega A(\theta_n^0)\left(\Delta\tilde{\phi}_{n+1}^{\text{eh}} - \Delta\tilde{\phi}_n^{\text{eh}}\right)\right]\hat{T}_{n,n+1} \\ &- \hbar\omega\sum_{n=1}^{N} A(\theta_n^0)\left(\hat{B}'_{n+1} - \hat{B}'_n\right)\left(\hat{T}_{n,n+1} - \left\langle\hat{T}_{n,n+1}\right\rangle\right) \\ &+ \hbar\omega\sum_{n=1}^{N}\left(\hat{b}'^{\dagger}_n\hat{b}'_n + \frac{1}{2}\right) \\ &+ \frac{\hbar\omega}{2}\sum_{n=1}^{N} A(\theta_n^0)\left(\Delta\tilde{\phi}_{n+1}^{\text{eh}} - \Delta\tilde{\phi}_n^{\text{eh}}\right)\left\langle\hat{T}_{n,n+1}\right\rangle. \end{aligned} \tag{5.31}$$

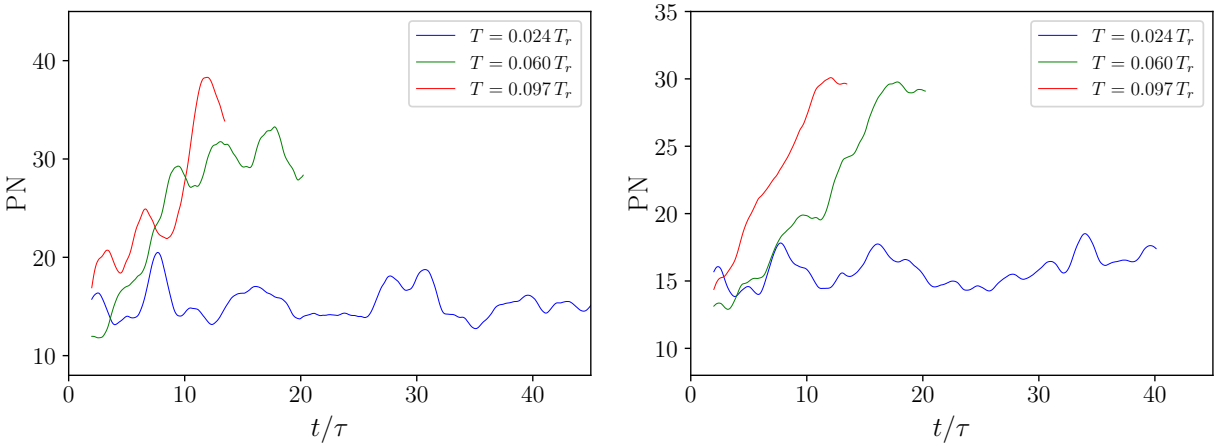


Figure 5.23: Localisation length of the evolving state, $|\Psi(t)\rangle$, as a function of time at different temperatures, showing (a) individual trajectories and (b) trajectory ensemble averages. The curves are smoothed for better legibility.

The total simulation time allowed under these conditions is significantly reduced, and further decreases at higher temperatures, as the entropy of the system increases. Regardless, the general trends observed in the results above are reproduced. Figure 5.23 shows that the localisation length remains at a low (albeit higher) near-constant level in the lowest temperature regime, while increasingly rapidly in the intermediate regime identified previously. This holds both for individual example trajectories (Fig. 5.23a), and the ensemble averages taken over a few different trajectories (Fig. 5.23b). Simultaneously, the occupation probabilities of

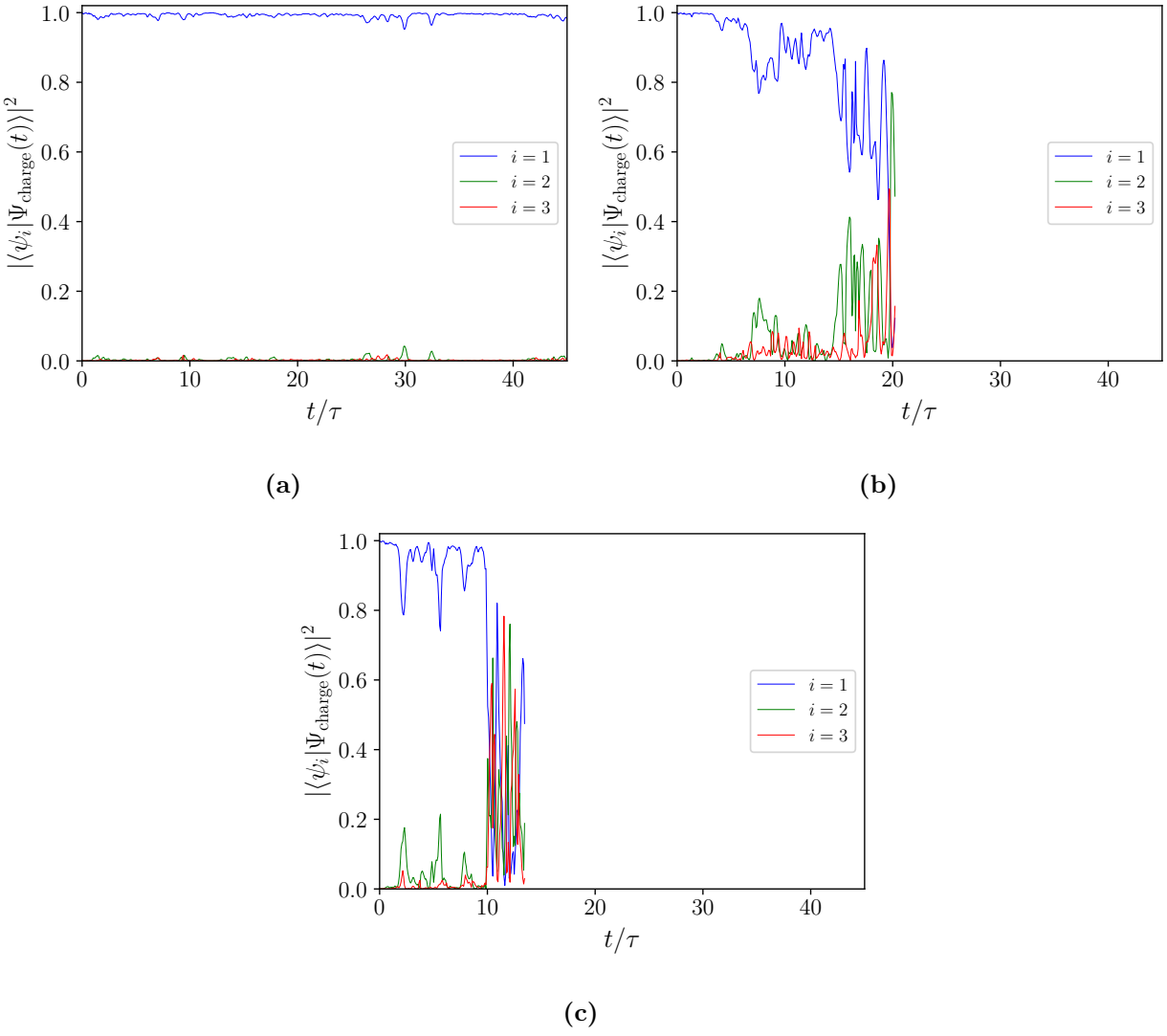


Figure 5.24: Probabilities that the charge subspace of the evolving quantum state, $|\Psi_{\text{charge}}\rangle$, occupies an instantaneous adiabatic state, $|\psi_i\rangle$, as a function of time at (a) $T = 0.024\,T_r$, (b) $T = 0.060\,T_r$, and (c) $T = 0.097\,T_r$. The trajectories are the same ones as shown in Fig. 5.23a.

the lowest adiabatic eigenstates of the charge Hamiltonian are shown in Fig. 5.24, corresponding to the individual trajectories in Fig. 5.23a. Both sets of results illustrate a qualitative agreement with the Ehrenfest method, but show that the quantised rotons lead to a quicker onset of the thermalised behaviour (i.e., increase in localisation length and mixing of states). Finally, Fig. 5.25 shows a plot of the mean-squared displacement of the charge (with corresponding Ehrenfest values also plotted

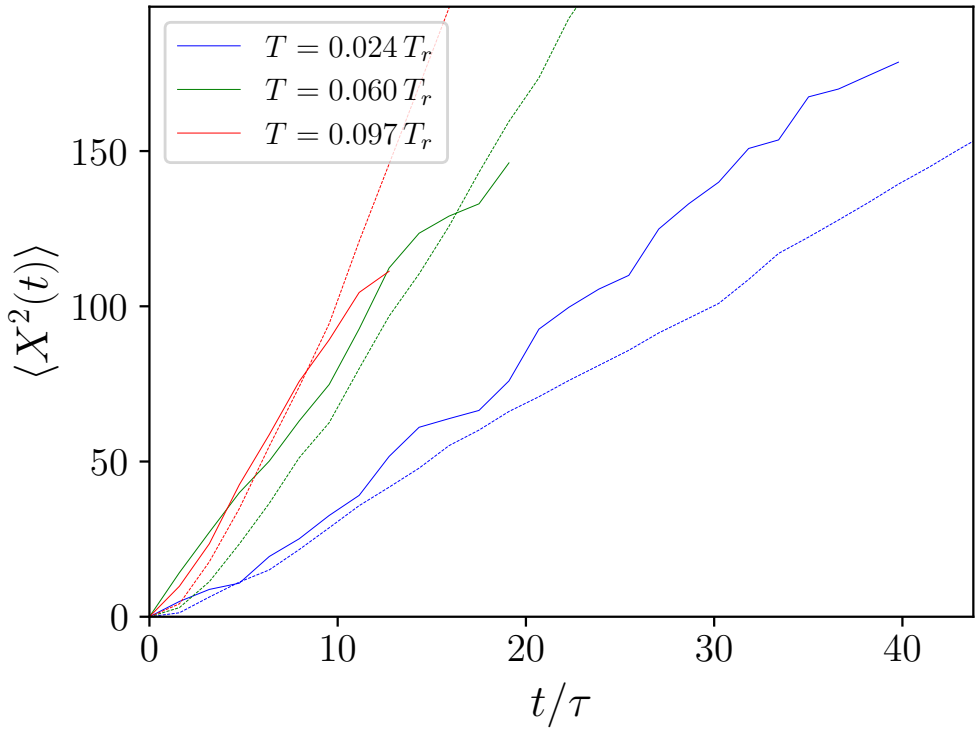


Figure 5.25: Ensemble average of polaron mean-square-displacement as a function of time for trajectories with quantised rotons (solid lines), compared to purely Ehrenfest trajectories (dashed lines), as previously shown in Fig. 5.11 at longer timescales.

alongside), which matches the temperature ordering expected, but the simulations are too short for meaningful calculation and comparison of diffusion constants.

5.3 Discussion and Conclusions

In this chapter, a mixed quantum-classical model of charge-polaron transport in conjugated polymers was presented. The main feature of the model is that the charge dynamics is being driven by torsional motion present in the system. Initially, the electronic charge coupling to the rotational degrees of freedom results in self-localisation into a Landau polaron state. The temperature-dependent fluctuations of the torsional displacements result in thermally driven polaron dynamics. Given the low-energy nature of the model, a natural choice for the model was the polaron

reorganisation energy, E_r, which defined the temperature scale as $T_r \sim 400\,\mathrm{K}$.

The simulation results identified two distinct temperature regimes, both $T < T_r$, which display different types of dynamics. At the lowest temperatures, as expected, only the lowest energy eigenstate is occupied, and the system evolves quasidiabatically. This means an activationless diffusion of the polaron along the length of the chain. This random crawling motion is consistent with previous work in the field.[102, 103, 107, 114] In this regime, the diffusion constant has a linear dependency on temperature, $D(T) \propto T$. As temperature increases, but still well below T_r, the greater thermal fluctuations result in an activated mode of transport, with transitions between diabatic states. This hopping dynamics follows Landau-Zener-type dynamics, caused by the fluctuating torsional angles of polymer units, leading to temporarily degenerate neighbouring diabatic states. This is consistent with the Marcus theory picture of charge transfer.

The majority of this work was performed within the framework of the Ehrenfest approximation, modelling the rotational degrees of freedom classically, while evolving the charge wavefunction quantum mechanically. This was necessary for the desired long simulation times to be achieved. As detailed in Chapter 2 already, this approximation assumes separation of the electronic and nuclear degrees of freedom. Crucially, with the nuclear motion being determined by the mean electronic potential, theoretical predictions drawn from the method may be incorrect.[166, 211] Additionally, due to the inaccurate description of energy transfer between quantum and classical subsystems, detailed balance is not always satisfied.[166, 170]

Despite the shortcomings of Ehrenfest dynamics, Burghardt and co-workers[112] have showed that in their small systems, the methodology is in good qualitative agreement with the quantum mechanical solution, attributing this agreement to the quasiadiabatic nature of their dynamics. As discussed above, the frequency

of transitions in the presented simulations was quantified using the evaluation of transition rates, through two different methods. The nonadiabatic transition rate, k_{NA}, was calculated from the occupation probabilities of the instantaneous adiabatic eigenstates, whereby the probability of occupying the lowest eigenstate dipping below 0.5 was defined as a nonadiabatic event. Conversely, the rate of hopping events, k_{hop}, derived from the diffusion constants of the polaron dynamics, is assumed to correspond to the quasiadiabatic transition events (Landau-Zener transitions where the system remains on the lower energy surface). As shown in Fig. 5.22, contrasting the two rates, we see that at lower temperatures, $k_{\mathrm{NA}} \approx k_{\mathrm{hop}}$, but k_{NA} grows significantly faster with temperature than k_{hop}, which indicates that the likelihood of observing the type of hopping transitions illustrated in Fig. 5.18 in a quasiadiabatic regime is very low. Figure 5.22 also shows the Marcus theory transition rate expression from Eq. (5.26) fitted to the values of k_{hop}, giving a reasonably good fit across the temperature range considered. Notably, the demonstrated Landau-Zener type hopping in this work provides a qualitative link to the 'fluctuating-bridges' mechanism of charge transfer[92, 96, 97], which was employed in the bulk mobility model presented in Chapter 4.

Given that the results presented show that the mean-square-displacement plots remain linear after the equilibration time period at all temperature values, it is not clear that the Ehrenfest approximation breaks down in this model, and that the observed transitions are due to heating. If significant heating effects were to occur, the gradients should also increase with time. The results from quantised rotons also indicate that the dynamics of the system progresses in a qualitatively similar way to the purely Ehrenfest results.

Valuable simulation results at higher temperatures would be difficult to obtain within the current model as the simulations are increasingly difficult to process

and interpret as the polaron state becomes more delocalised. Tracking centre-of-mass displacements in the periodic system relies on relatively small changes between consecutive simulation time steps, and delocalised systems can cause density fluctuations across boundary edges that become impossible to track. Qualitatively it is expected that as $T \to T_r$, the polaron becomes unbound and charge transport is expected to follow band-like behaviour. At this stage the populated states would be expected to be quasi-extended in nature.[138, 139, 212] This is also the regime where the increased thermal fluctuations can lead to transient localisation, leading to an eventual saturation and decrease in charge diffusion, as described in Chapter 1 before.[123, 124] The investigations of Troisi and Orlandi[101], as well as Wang and Beljonne's,[106] based on the similar Su-Schrieffer-Heeger model Hamiltonian[213] indeed show this band-like, $\mu \sim T^{-\alpha}$, decay of charge mobility with temperature. Within the same model, Wang and Beljonne observed trends compatible with a hopping, Marcus-like mechanism when the relative strength of electron-phonon coupling was sufficiently high.

The current model could be further improved to be able to describe low and high temperature regimes alike. Modelling the torsional motion quantum mechanically would be one of the options, but as shown above, within the current simulation framework this is prohibitively expensive. Alternatively, implementing surface hopping methods might be sufficient to improve the higher temperature behaviour by mitigating the shortcomings of Ehrenfest methods near conical intersections and avoided crossings. Such simulations have been successfully employed for organic semiconductors.[106] Such improvements would hopefully lead to capturing the different temperature regimes highlighted above within the scope of a single model.

Acknowledgement of Contributions

The TEBD-Ehrenfest simulation program used in this chapter built on the initial version created by Jonathan Mannouch, Sarah Al-Assam, and William Barford. The initial program code was rewritten to model the Langevin classical dynamics, incorporate the periodic boundary conditions (the implementation of which was based on discussions with Stephen Clark) and record the underlying eigenstate distribution by me.

6
Conclusions and Future Work

The charge dynamics and charge mobility in π-conjugated polymer model systems was investigated. Understanding the mechanism and hindrances to high mobility is crucial to the development, improvement and wider applications of devices based on these materials as semiconductors. Given that these processes are affected by contributions on vastly different length and time scales, the problem was approached using multiple, characteristically different modelling techniques.

Firstly, as presented in Chapter 4, the bulk material charge mobility was modelled based on realistic, disordered, long-chain PPV aggregate structures. This model allowed for systematic expansion and improvement of the GDM approach dominating large-scale charge mobility studies in the literature over the past decades. The off-diagonal energetic disorder has a clear link to the structural (torsional) disorder present in the polymer chains. Overall, effective disorder of $\sim 1-5\times k_BT$ (relative to 298 K) was studied, defined as the the width of the portion of the DOS corresponding to highly localised states. The novel combination of inter- and intra-chain hopping events, incorporating both low-energy localised and higher energy quasi-extended states gave insights into the competing intramolecular and intermolecular processes. Assigning positions to the donor and acceptor states within real-space structures

also added a more nuanced picture of charge displacement and migration. Charge mobility trends were observed with respect to the applied electric field bias, disorder (both diagonal and off-diagonal), temperature, and polymer chain orientation. In all examined systems, at high enough field bias, a Poole-Frenkel type, $\log \mu \propto \sqrt{F}$, decay of charge mobility was present. This general feature was attributed to the Marcus inverted regime. At lower field strength values, the observed trends were more varied. The trends were best explained by considering the relative magnitude of disorder and thermal energy. The low temperature/high disorder systems showed weakly field-assisted charge transport, while the high temperature/low disorder ones displayed mostly field-independent charge mobility until the onset of the high field decay. Importantly, when considering charge transport involving only the lowest energy localised states, the charge migration process was almost exclusively made up of intermolecular hopping events. This is easily rationalised by the poor overlap of these localised states along a given chain. Crucially, incorporating the quasi-extended states in the process showed a significantly increased level of mobility at high electric field strength, with the portion of intramolecular, as well as localised to quasi-extended state hopping events both increasing simultaneously with the applied field bias. This result highlights the importance of both higher-lying energy, extended states, as well as intramolecular mode of transport in certain scenarios. This mode of transport is a significant extension to the simple hopping mechanisms involving only localised states.

Motivated by the need for a better understanding of the intramolecular processes, whose importance was highlighted by the preceding chapter, the model presented in Chapter 5 examined charge migration along a single polymer chain induced by thermal fluctuations in the torsional structure. The dynamics of the charged particle was solved using a TEBD-Ehrenfest algorithm, which primarily meant a

quantum mechanical evolution of the electronic degrees of freedom in the MPS formalism, coupled to torsional oscillators at each polymer monomer site, obeying the classical Langevin equation. On a smaller time scale, computational resources and algorithmic stability permitting, the purely Ehrenfest results were confirmed using a model incorporating quantised corrections to the rotational motion, which showed good agreement. In each instance, periodic boundary conditions were applied to the systems to avoid boundary edge effects as the polaron reaches the end of the polymer chain during the long simulations. The dynamics of the modelled charge polaron revealed the emergence of two distinct temperature regimes, both well below the reorganisation temperature, $T_r = E_r/k_B$. In the lowest temperature regime, the localised polaron starting state displayed a 'crawling' motion along the polymer chain, while retaining its low localisation length and shape. Diffusion constants calculated from this charge migration scaled linearly with temperature, as is expected for purely diffusive motion. The system remains in the lowest quasidiabatic state throughout the length of the simulation, with no diabatic energy level crossings observed. As the temperature is raised, the involvement of higher-lying energy states increases, too. As a consequence of the increased torsional fluctuations, the evolving state is no longer localised for the entirety of the simulation, exhibiting both diabatic energy level crossings and significantly increased probabilities of occupying higher-lying adiabatic eigenstates. This is explained by Landau-Zener type transitions between the diabatic evolving states, which was confirmed by observing the underlying instantaneous eigenstates of the system Hamiltonian. These transitions occur at torsional geometries that create energetically degenerate states, aligning with the Marcus theory picture of charge transfer. While nonadiabatic events are assumed to dominate as the temperature

increases, the observed hopping events nonetheless establish a link to the Marcus theory mode of charge transport modelled in the bulk material previously.

Future Work

The current models are not without their limitations. Firstly, while the use of realistic polymer structures to describe bulk mobility is an improvement upon previously reported charge transfer simulations, structure-property studies of π-conjugated polymers based on molecular dynamics simulations are present in the literature.[144, 214–216] Obtaining fully atomistic bulk structures from MD simulations would be a natural pathway to improve the charge mobility model, though this might not be computationally feasible on the required length scales for some time to come. Additionally, given that the kinetic Monte Carlo model relies so heavily on the transition rates between donor and acceptor states, improved and more sophisticated rates could further verify the findings of the current model. Such transition rate models exist in the literature,[159] and could offer interesting insights especially in the high field strength (i.e., Marcus inverted) regime.

The limitations to the intramolecular quantum-classical model come from two main sources. Firstly, in general, once higher system temperatures lead to the population of higher-lying states, and particle density becomes more spread out over the modelled polymer chain, it becomes challenging to track physical displacements along the chain. More fundamentally, the classical evolution of the nuclear degrees of freedom in the Ehrenfest scheme leads to well documented problems in terms of long term equilibrium populations and unphysical heating. While there was no obvious breakdown of the scheme seen in the work presented, implementing a more robust quantum-classical methodology, such as the surface hopping approach present in literature for organic systems,[104] would be preferable. Resolving these outstanding

challenges, a single model describing the temperature regimes identified in this work, as well as the high temperature, band-like regime of charge transport[123] should be possible and doing so would be the goal of any future work.

Appendices

A

Quantised Rotons in TEBD-Ehrenfest Scheme

The quantum mechanical treatment of additional degrees of freedom in mixed quantum-classical dynamics schemes can improve the description of energy transfer between quantum and classical subsystems, a potential issue arising in Ehrenfest-type schemes, as highlighted in Chapters 2 and 5. The extension of the pure Ehrenfest method introduced in Chapter 5 to allow for quantum mechanical corrections in the torsional motion is presented below. The derivation closely follows the work of Mannouch and Barford.[109, 210]

The derivation of this effective Hamiltonian, already shown in Eq. (5.31), starts with considering the state of system in the form

$$|\Psi\rangle = \sum_{j} \sum_{\{p\}} C_{j,\{p\}}(t) \, |j, \{p(t)\}\rangle \, , \tag{A.1}$$

where the time-dependent probability amplitude, $C_{j,\{p\}}(t)$, is determined by the Hamiltonian. The time-dependent basis follows Ehrenfest mean-field evolution and can be expressed as

$$|j, \{p(t)\}\rangle = |\psi_j\rangle \, |p_1(t)\rangle \, |p_2(t)\rangle \ldots |p_N(t)\rangle \, , \tag{A.2}$$

where $|\psi_t\rangle$ is the solution of the charge-exciton part of the Hamiltonian (the first two terms of Eq. (5.1) or the first term of Eq. (5.29) when the uniform on-site energies are ignored). The states $|p_n(t)\rangle$ denote the p^{th} displaced excitation of the coherent state on the n^{th} site, $|\alpha_n\rangle$, written as[109]

$$|p_n(t)\rangle = \frac{\left(\hat{b}_n'^{\dagger}\right)^p}{\sqrt{p!}} |\alpha_n\rangle \,, \tag{A.3}$$

with $\hat{b}_n'^{\dagger}$ being the time-dependent displaced creation operator, linked to the creation operator without displacement, $\hat{b}_n^{\dagger}$, by

$$\hat{b}_n'^{\dagger}(t) = \hat{b}_n^{\dagger} - \alpha_n^*(t) \tag{A.4}$$

and

$$|\alpha_n\rangle = \exp\left(-\frac{|\alpha_n|^2}{2}\right) \sum_{q=0}^{\infty} \frac{(\alpha_n)^q}{\sqrt{q!}} |q_n\rangle \tag{A.5}$$

$$|q_n\rangle = \frac{\left(\hat{b}_n^{\dagger}\right)^q}{\sqrt{q!}} |0\rangle \,. \tag{A.6}$$

The state $|\alpha_n\rangle$ itself is defined by the Ehrenfest mean-field variables, such that

$$\alpha_n(t) = \frac{\Delta\tilde{\phi}_n^{\text{eh}} + \mathrm{i}\tilde{L}_n^{\text{eh}}}{\sqrt{2}}, \tag{A.7}$$

and satisfies the Ehrenfest equations of motion as defined by Eqs. (5.18) and (5.19), and therefore we have

$$\frac{\mathrm{d}\alpha_n}{\mathrm{d}t} = -\mathrm{i}\alpha_n + \mathrm{i}\frac{\lambda_n}{\sqrt{2}}, \tag{A.8}$$

where

$$\lambda_n = A_{n-1}\langle\hat{T}_{n-1,n}\rangle - A_n\langle\hat{T}_{n,n+1}\rangle \tag{A.9}$$

as introduced in Eq. (5.12). Considering that $|\Psi\rangle$ satisfies the TDSE with the Hamiltonian defined in Eq. (5.29), we have

$$\mathrm{i}\hbar\sum_j\sum_{\{p\}}\left(\dot{C}_{j,\{p\}}\,|j,\{p\}\rangle + C_{j,\{p\}}\,|j,\{\dot{p}\}\rangle\right) = \sum_j\sum_{\{p\}} C_{j,\{p\}}\hat{H}\,|j,\{p\}\rangle \,. \tag{A.10}$$

Therefore, if we have

$$|j,\{\dot{p}\}\rangle = \frac{\mathrm{d}}{\mathrm{d}t}|j,\{p\}\rangle = \frac{\mathrm{i}}{\hbar}\hat{H}'\,|j,\{p\}\rangle\,, \tag{A.11}$$

the relation in Eq. (A.10) becomes

$$\mathrm{i}\hbar\sum_j\sum_{\{p\}}\dot{C}_{j,\{p\}}\,|j,\{p\}\rangle = \sum_j\sum_{\{p\}}C_{j,\{p\}}\left(\hat{H}+\hat{H}'\right)|j,\{p\}\rangle\,, \tag{A.12}$$

or equivalently,

$$\mathrm{i}\hbar\frac{\mathrm{d}}{\mathrm{d}t}C_{j,\{p\}}\,|j,\{p\}\rangle = \sum_{j'}\sum_{\{p'\}}\langle j,\{p\}|\underbrace{\left(\hat{H}+\hat{H}'\right)}_{\hat{H}_{\mathrm{eff}}}|j',\{p'\}\rangle\,C_{j',\{p'\}}. \tag{A.13}$$

Therefore, we are looking for

$$\frac{\mathrm{d}}{\mathrm{d}t}|p_n(t)\rangle = \frac{\mathrm{d}}{\mathrm{d}t}\left[\frac{\left(\hat{b}_n'^{\dagger}\right)^p}{\sqrt{p!}}|\alpha_n\rangle\right] \tag{A.14}$$

$$= p\frac{\left(\hat{b}_n'^{\dagger}\right)^{p-1}}{\sqrt{p!}}\frac{\mathrm{d}\left(\hat{b}_n'^{\dagger}\right)}{\mathrm{d}t}|\alpha_n\rangle + \frac{\left(\hat{b}_n'^{\dagger}\right)^p}{\sqrt{p!}}\frac{\mathrm{d}}{\mathrm{d}t}|\alpha_n\rangle\,. \tag{A.15}$$

Using definitions in Eqs. (A.4), (A.5) and (A.8),

$$\begin{aligned}\frac{\mathrm{d}}{\mathrm{d}t}|p_n(t)\rangle =& -\dot{\alpha}_n^* p\frac{\left(\hat{b}_n'^{\dagger}\right)^{p-1}}{\sqrt{p!}}|\alpha_n\rangle - \frac{1}{2}\left(\dot{\alpha}_n^*\alpha_n+\alpha_n^*\dot{\alpha}_n\right)\frac{\left(\hat{b}_n'^{\dagger}\right)^p}{\sqrt{p!}}|\alpha_n\rangle \\ &+ \frac{\left(\hat{b}_n'^{\dagger}\right)^p}{\sqrt{p!}}\exp\left(-\frac{|\alpha_n|^2}{2}\right)\dot{\alpha}_n\sum_{q=0}^{\infty}q\frac{(\alpha_n)^{q-1}}{\sqrt{q!}}|q_n\rangle \qquad (A.16)\\ =& -\dot{\alpha}_n^*\underbrace{\sqrt{p}\,\frac{\left(\hat{b}_n'^{\dagger}\right)^{p-1}}{\sqrt{(p-1)!}}|\alpha_n\rangle}_{\hat{b}_n'|p_n\rangle} - \frac{1}{2}\left(\dot{\alpha}_n^*\alpha_n+\alpha_n^*\dot{\alpha}_n\right)|p_n\rangle \\ &+ \frac{\left(\hat{b}_n'^{\dagger}\right)^p}{\sqrt{p!}}\dot{\alpha}_n\underbrace{\exp\left(-\frac{|\alpha_n|^2}{2}\right)\sum_{q=0}^{\infty}\sqrt{q}\frac{(\alpha_n)^{q-1}}{\sqrt{(q-1)!}}|q_n\rangle}_{(*)} \qquad (A.17)\end{aligned}$$

Evaluating $(*)$ separately, noticing that the $q=0$ term vanishes, and using

$m = q - 1$ substitution, we get,

$$\begin{aligned}(*) &= \exp\left(-\frac{|\alpha_n|^2}{2}\right)\sum_{m=0}^{\infty}\sqrt{m+1}\frac{(\alpha_n)^m}{\sqrt{(m)!}}\left|(m+1)_n\right\rangle \\ &= \exp\left(-\frac{|\alpha_n|^2}{2}\right)\sum_{m=0}^{\infty}\frac{(\alpha_n)^m}{\sqrt{(m)!}}\underbrace{\sqrt{m+1}\left|(m+1)_n\right\rangle}_{\hat{b}_n^\dagger|m_n\rangle} \\ &= \hat{b}_n^\dagger\left|\alpha_n\right\rangle. \end{aligned} \tag{A.18}$$

Which simplifies Eq. (A.17) to

$$\frac{\mathrm{d}}{\mathrm{d}t}\left|p_n(t)\right\rangle = \left(-\dot{\alpha}_n^*\hat{b}_n' - \frac{1}{2}\left(\dot{\alpha}_n^*\alpha_n + \alpha_n^*\dot{\alpha}_n\right) + \dot{\alpha}_n\hat{b}_n^\dagger\right)\left|p_n\right\rangle. \tag{A.19}$$

Using Eqs. (A.4) and (A.8), this becomes

$$\frac{\mathrm{d}}{\mathrm{d}t}\left|p_n\right\rangle = \mathrm{i}\left\{-|\alpha_n|^2 + \frac{\lambda_n}{2}\underbrace{\frac{\alpha_n+\alpha_n^*}{\sqrt{2}}}_{=\Delta\tilde{\phi}_n^{\mathrm{eh}}\ \text{[Eq. (A.7)]}} + \lambda_n\underbrace{\frac{\hat{b}_n'^\dagger+\hat{b}_n'}{\sqrt{2}}}_{\equiv\hat{B}_n'\ \text{[c.f.Eq. (5.28)]}} + \left(\alpha_n^*\hat{b}_n' + \alpha_n\hat{b}_n'^\dagger\right)\right\}\left|p_n\right\rangle, \tag{A.20}$$

which therefore defines $\hat{H}'$ from Eq. (A.11) once the sum over all n is taken. To obtain the full effective Hamiltonian, $\hat{H}_{\mathrm{eff}}$, we need to consider Eq. (5.29) with the appropriate $\hat{b}_n \to \hat{b}_n' + \alpha_n$ (and accompanying $\hat{b}_n^\dagger \to \hat{b}_n'^\dagger + \alpha_n^*$ and $\hat{B}_n \to \hat{B}_n' + \Delta\tilde{\phi}_n^{\mathrm{eh}}$) substitution. Following this, we finally get:[109]

$$\begin{aligned}\hat{H}_{\mathrm{eff}} &= \hat{H} + \hat{H}' \\ &= \sum_{n=1}^{N}\left[J_n^0 - \hbar\omega A(\theta_n^0)\left(\Delta\tilde{\phi}_{n+1}^{\mathrm{eh}} - \Delta\tilde{\phi}_n^{\mathrm{eh}}\right)\right]\hat{T}_{n,n+1} \\ &\quad - \hbar\omega\sum_{n=1}^{N}A(\theta_n^0)\left(\hat{B}_{n+1}' - \hat{B}_n'\right)\left(\hat{T}_{n,n+1} - \left\langle\hat{T}_{n,n+1}\right\rangle\right) \\ &\quad + \hbar\omega\sum_{n=1}^{N}\left(\hat{b}_n'^\dagger\hat{b}_n' + \frac{1}{2}\right) \\ &\quad + \frac{\hbar\omega}{2}\sum_{n=1}^{N}A(\theta_n^0)\left(\Delta\tilde{\phi}_{n+1}^{\mathrm{eh}} - \Delta\tilde{\phi}_n^{\mathrm{eh}}\right)\left\langle\hat{T}_{n,n+1}\right\rangle, \end{aligned} \tag{A.21}$$

which is the overall Hamiltonian that the system is subjected to, achieving the desired quantised correction to the mean-field Ehrenfest evolution.

B

Benchmarking Periodic Boundary Conditions in TNT

Periodic boundary conditions were implemented into the Tensor Network Theory (TNT) library in order to extend its functionality by overcoming edge effects due to limited system sizes and to allow simulation of systems which would have periodicity naturally occurring in their structure, such as macrocyclic materials. The approach taken to achieve this added functionality was described in Chapter 3. A brief testing and benchmarking of the implementation is presented below. This was done in three parts. Firstly, the verification of accuracy was performed on a simple tight-binding system. Secondly, within the same tight-binding model, a larger scan of system parameters was performed to ascertain the scaling of computational cost within the model. Finally, the computational scaling of including the quantised oscillator correction, introduced in Chapter 5 and derived in Appendix A, is tested.

B.1 Tight-Binding Model

The tight-binding model that the initial tests were based on can be described by the Hamiltonian

$$\hat{H}_{\mathrm{OBC}} = \sum_{n=1}^{L} \epsilon_n \hat{c}_n^\dagger \hat{c}_n + \sum_{n=1}^{L-1} J_{n,n+1} \left(\hat{c}_{n+1}^\dagger \hat{c}_n + \hat{c}_n^\dagger \hat{c}_{n+1} \right), \tag{B.1}$$

for the the open-boundary system, and

$$\hat{H}_{\mathrm{PBC}} = \hat{H}_{\mathrm{OBC}} + \hat{H}_{\mathrm{edge}} = \hat{H}_{\mathrm{OBC}} + J_{1,L}\left(\hat{c}_1^{\dagger}\hat{c}_L + \hat{c}_L^{\dagger}\hat{c}_1\right) \tag{B.2}$$

for the periodic ones. The only difference between the two systems is the linking hopping term between the two ends of the chain. The terms denote the on-site energies, ϵ_n, the transfer integrals, $J_{n,n+1}$, and the creation/annihilation operators, $\hat{c}_n^{\dagger}/\hat{c}_n$, for a chain of length L.

B.1.1 Boundary Verification

Analytic Results

Comparing against the exact results shows that the TEBD solution follows the correct time evolution, and particle density is transferred between the end sites, as required by the periodic boundary conditions. This was performed on a system initiated fully localised on one site of the chain, and subjected to time evolution using the TEBD algorithm. Given a starting state, $|\psi_0\rangle$, expressed as a linear combination of the eigenbasis, $\{|n\rangle\}$:

$$|\psi(\tilde{t}=0)\rangle = \sum_n a_n|n\rangle, \tag{B.3}$$

where the expansion coefficient, a_n, are given as

$$a_n = \langle n|\psi(\tilde{t}=0)\rangle. \tag{B.4}$$

The state at any time, $\tilde{t} \neq 0$, will be given as:

$$|\psi(\tilde{t})\rangle = \sum_n a_n \exp\left(-\mathrm{i}E_n\tilde{t}\right)|n\rangle, \tag{B.5}$$

where E_n denotes the energy corresponding to eigenstate $|n\rangle$. This gives the analytic solution for the problem, which is compared to the TEBD solution at long timescales, as shown in Fig. B.1. The time evolution is expressed in terms of dimensionless units of time, $\tilde{t} = t * (J_0/\hbar)$, scaled to the relevant energy scale of the dynamics, the transfer integral, J_0.

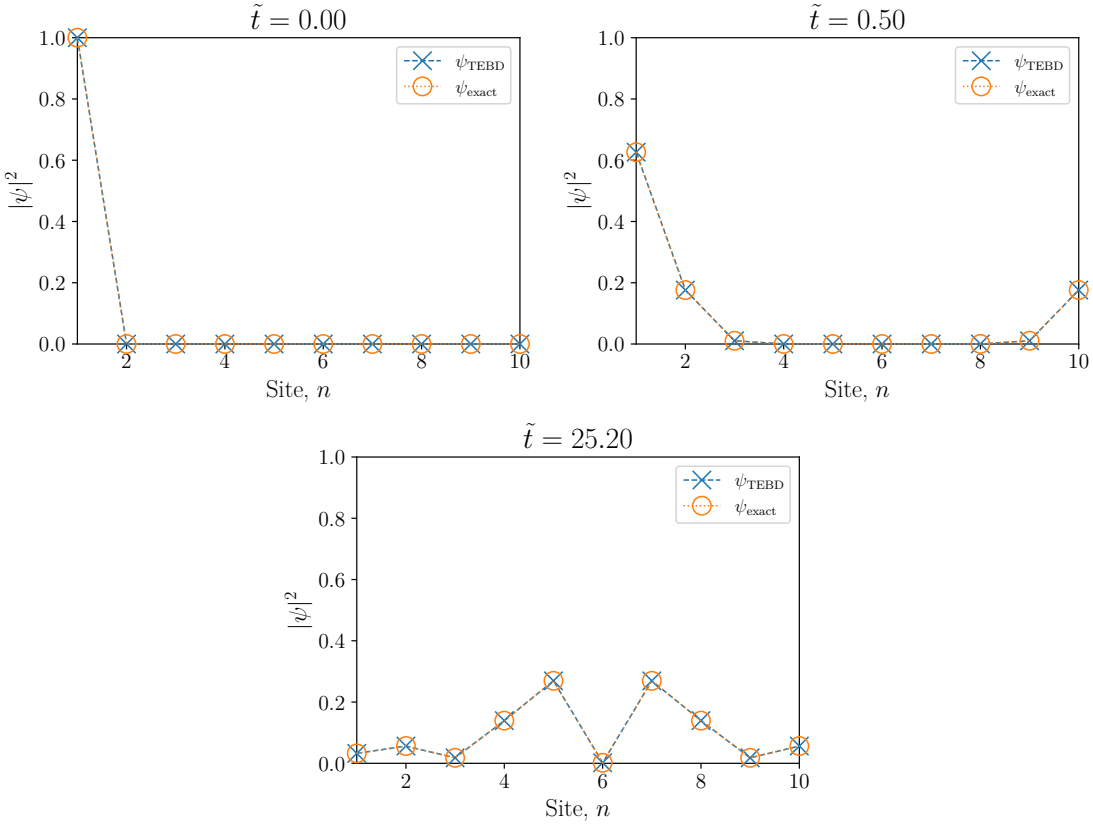


Figure B.1: Comparison time evolution snapshots of TEBD (ψ_{TEBD}) with analytic solution (ψ_{exact}).

Site Independence

The second fundamental requirement is that for appropriately implemented periodic boundary conditions, the expectation is that system exhibits a translational symmetry. This was tested by running time evolutions from fully localised starting states on different sites (1st and 3rd) of the chain, then plotting particle density with site coordinates shifted onto each other, shown in Fig. B.2.

B.1.2 Parameter Scan

With the basic functionality of the the periodic algorithms confirmed, a scan of calculation parameters was performed. The varying parameters included the length of chain, maximum internal dimension of the MPS, and time evolution step

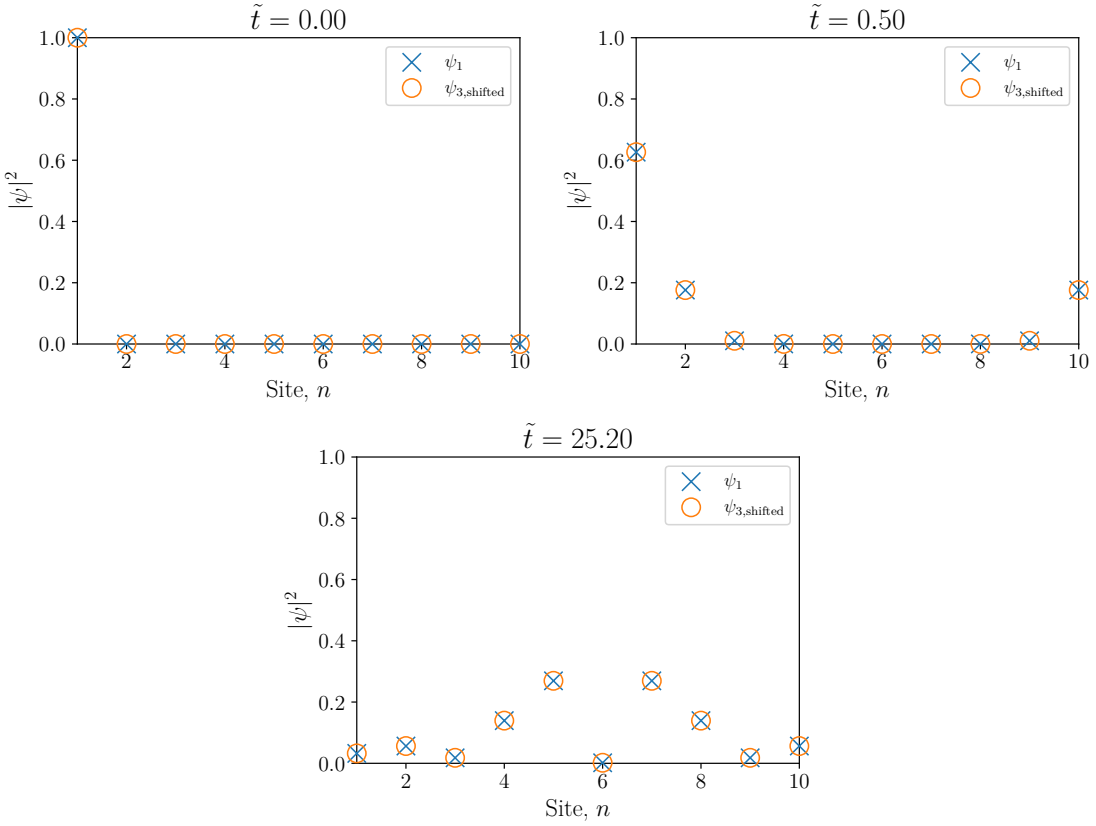


Figure B.2: Comparison of time evolution snapshots of a system started fully localised on site 1 (ψ_1), and one fully localised on site 3, but plotted along shifted site coordinates ($\psi_{3,\text{shifted}}$).

size. Open-boundary conditions were compared to the periodic implementation. Here, truncation is controlled through defining the maximum number of retained singular values, as χ_{max}. Additionally, the ratio of the smallest and largest singular values retained, S_{ratio}, in an SVD can be controlled by the TNT library's `tntSystem.rel_trunc_tol` parameter. The total number of singular values retained is the lower value of these two. The parameters were chosen to represent the relevant Hamiltonian parameters for conjugated polymer systems, i.e., they align well with the parameters presented in Chapters 4 and 5, and all simulations were run to the same total overall simulated time. The results are shown in Figs. B.3 to B.5. The observed trends can be summarised as follows:

- For a given total simulation time, the execution grows linearly with the total

number of simulation steps (or equivalently, with $1/\delta\tilde{t}$).

- The execution time grows linearly with the size of the chain, L.
- The maximum internal dimension, $\chi_{\max}$, has no significant effect on the simulation time once a critical value is reached, as is expected from the fact that the simulation code employs a truncation mechanism that reduces dimensionality, which is not affected by the maximum dimension allowed.
- Due to the additional SVD steps required, simulations with periodic boundary conditions have a $\sim 2\times$ longer execution time compared to open boundary conditions.

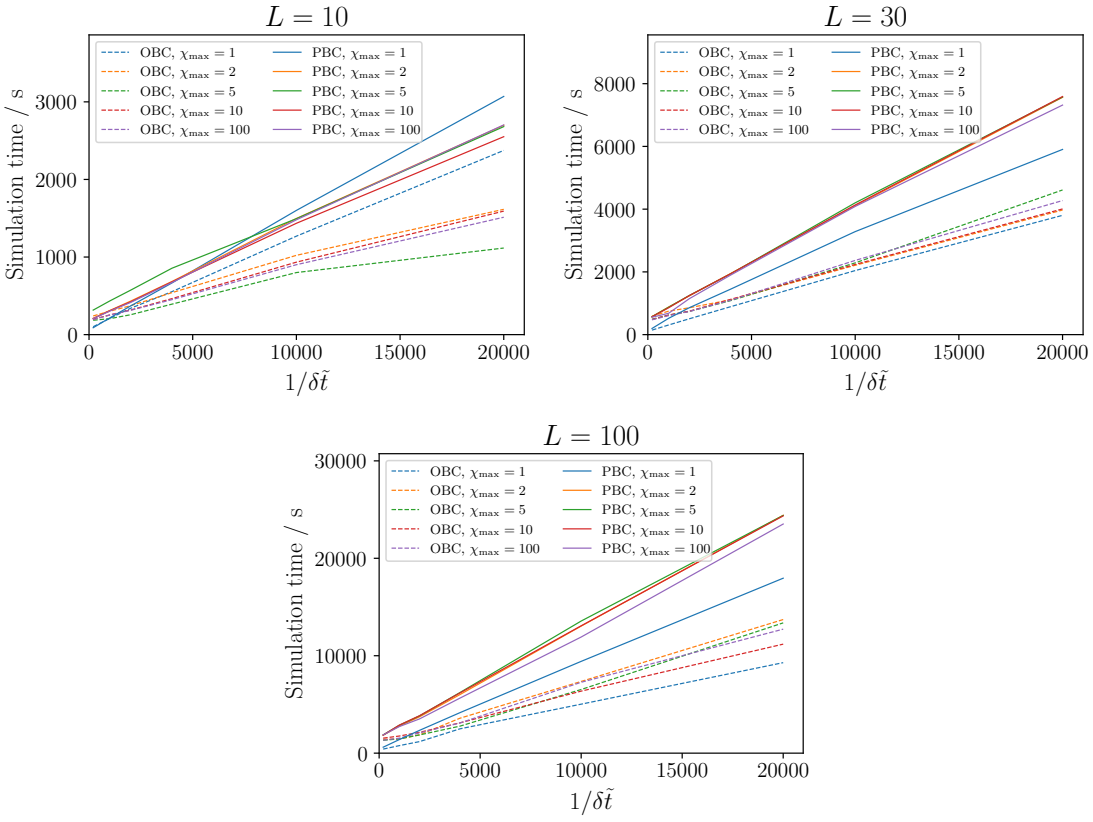


Figure B.3: Execution time as a function of $1/\delta t$, i.e. the number of total steps.

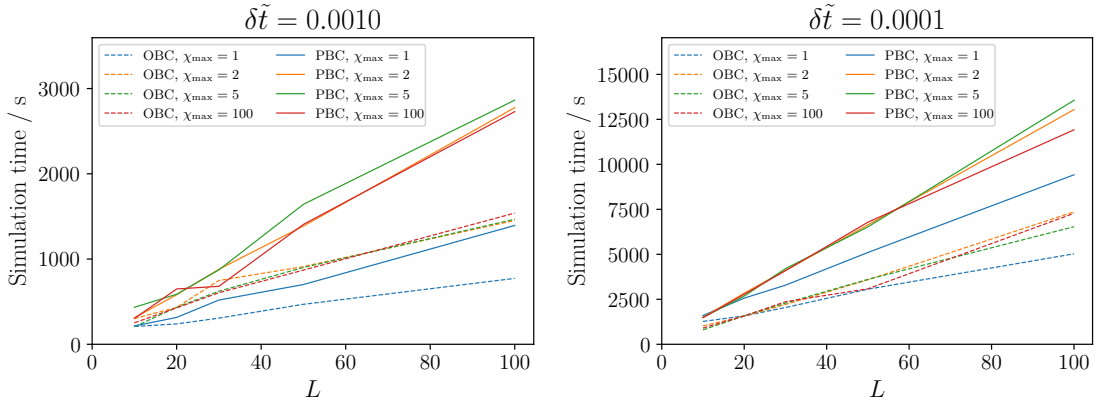


Figure B.4: Execution time as a function of the chain length, L.

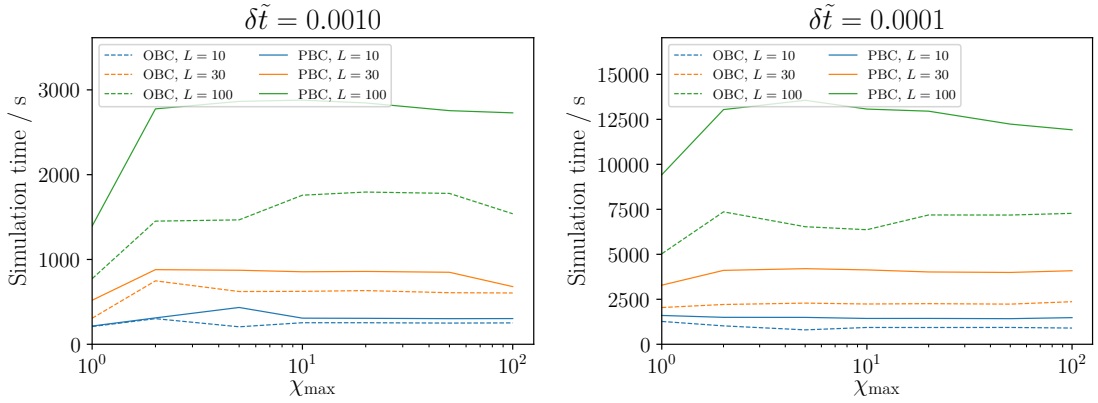


Figure B.5: Execution time as a function of the maximum internal dimension, χ.

B.2 Holstein Model

The Holstein model, as introduced in Chapter 2, describes a system with electron-phonon couplings present to normal modes on each site. As this model is employed to simulate polymeric systems, its computational performance was also briefly examined. Of particular interest was the model scaling when introducing quantised corrections to these normal modes, as introduced in Chapter 5, and further detailed in Appendix A. The introduction of quantised normal modes increases the site dimensionality from 2 to $2 * (n_{\nu_{max}} + 1)$, where $n_{\nu_{max}}$ is the number of modes included per site. This in turn increases the size of the total Hilbert space from 2^L

to $(2 * (n_{\nu_{\max}} + 1))^L$. The Hamiltonian is given in the form presented before:

$$\begin{aligned}\hat{H}_{\text{Holstein}} = &\sum_{n=1}^{N} \left[J_n^0 - \hbar\omega A(\theta_n^0) \left(\Delta\tilde{\phi}_{n+1}^{\text{eh}} - \Delta\tilde{\phi}_n^{\text{eh}} \right) \right] \hat{T}_{n,n+1} \\ &- \hbar\omega \sum_{n=1}^{N} A(\theta_n^0) \left(\hat{B}'_{n+1} - \hat{B}'_n \right) \left(\hat{T}_{n,n+1} - \left\langle \hat{T}_{n,n+1} \right\rangle \right) \\ &+ \hbar\omega \sum_{n=1}^{N} \left(\hat{b}'^{\dagger}_n \hat{b}'_n + \frac{1}{2} \right) \\ &+ \frac{\hbar\omega}{2} \sum_{n=1}^{N} A(\theta_n^0) \left(\Delta\tilde{\phi}_{n+1}^{\text{eh}} - \Delta\tilde{\phi}_n^{\text{eh}} \right) \left\langle \hat{T}_{n,n+1} \right\rangle , \end{aligned} \tag{B.6}$$

where the terms take their previously introduced meaning.

B.2.1 Effect of $\delta\tilde{t}$ on convergence

Before considering the effects of the quantised normal modes, it is worth noting that the time step of simulations, δt, should be considered carefully. Reducing the size of time step for accurate convergence may be necessary. In doing so, the time propagator, $\exp(\mathrm{i}\delta t)$, gets closer to the value of 1 for the real part, and 0 for the imaginary part, as shown in Table B.1. As a result, the relative changes to the wavefunction at each individual time step get smaller. In order for the small changes to be preserved after truncations in the SVD procedure, the ratio of smallest to largest singular value retained, S_{ratio}, has to be decreased for small time steps. This is controlled by TNT library's `tntSystem.rel_trunc_tol` parameter, as discussed previously. As a point of reference, a time step of 10^{-5} (in dimensionless time units), did not produce correct time evolution at $S_{\text{ratio}} = 10^{-5}$ – the particle density would be 'stuck' in a localised state – but did so at $S_{\text{ratio}} = 10^{-8}$, without noticeable increase in overall execution time for the low dimensionality systems.

Table B.1: Time evolution – value of $\exp(\mathrm{i}\delta t)$ for various values of δt.

Time step, δt	$\Re[\exp(\mathrm{i}\delta t)]$	$\Im[\exp(\mathrm{i}\delta t)]$
10^{-2}	$9.999500004166650 \times 10^{-1}$	$9.999833334167000 \times 10^{-3}$
10^{-3}	$9.999995000000420 \times 10^{-1}$	$9.999998333330000 \times 10^{-4}$
10^{-4}	$9.999999950000000 \times 10^{-1}$	$9.999999983300000 \times 10^{-5}$
10^{-5}	$9.999999999500000 \times 10^{-1}$	$1.000000000000000 \times 10^{-5}$
10^{-6}	$9.999999999995000 \times 10^{-1}$	$1.000000000000000 \times 10^{-6}$

B.2.2 Effect of $n_{\nu_{\max}}$

The introduction of a torsional mode ($n_{\nu_{\max}} = 1$), and therefore increasing the local dimension of the system, has significant impacts on the simulations. While execution times are still linear in the number of simulation steps taken (i.e., in $1/\delta t$ for a fixed total simulation time), the use of periodic boundary conditions once again carries a large time penalty over open boundary systems. This is demonstrated in Figs. B.6 and B.7, along with the fact that the level of truncation chosen has a crucial effect on simulation times. These observations can be explained by the increase in entanglement entropy and therefore the ability to truncate internal dimensions less while retaining accuracy. Particularly interesting is the subtle interplay between the two methods of truncation employed demonstrated in Fig. B.7, showing that at $S_{\max} = 10^{-5}$ level, this is a stronger criterium and therefore execution times are independent of the choice of $\chi_{\max}$ for all types of systems, while at $S_{\max} = 10^{-8}$, for a periodic system with a torsional mode included, $\chi_{\max}$ dictates the truncation level and therefore execution times change with this parameter. This highlights the need for even more careful considerations of system convergence and using appropriate levels of truncation to avoid simulation times becoming unfeasibly long when employing the periodic boundary condition implementation. Finally, the results highlight that the inclusion of quantised normal modes combined with

periodic boundary conditions brings very high computational costs, and can make long time dynamics unfeasible.

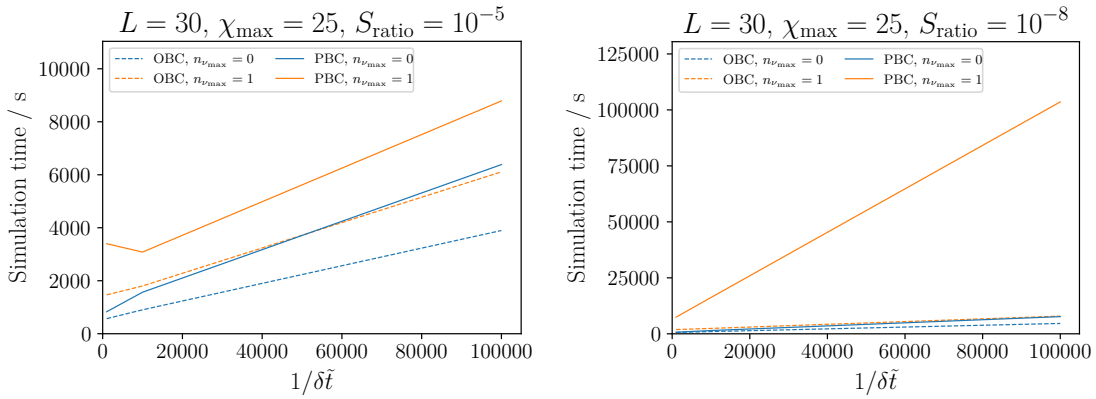


Figure B.6: Effect of $n_{\nu_{\max}}$ and boundary types on total execution time as a function of $1/\delta t$, at different truncation levels, defined by S_{ratio}.

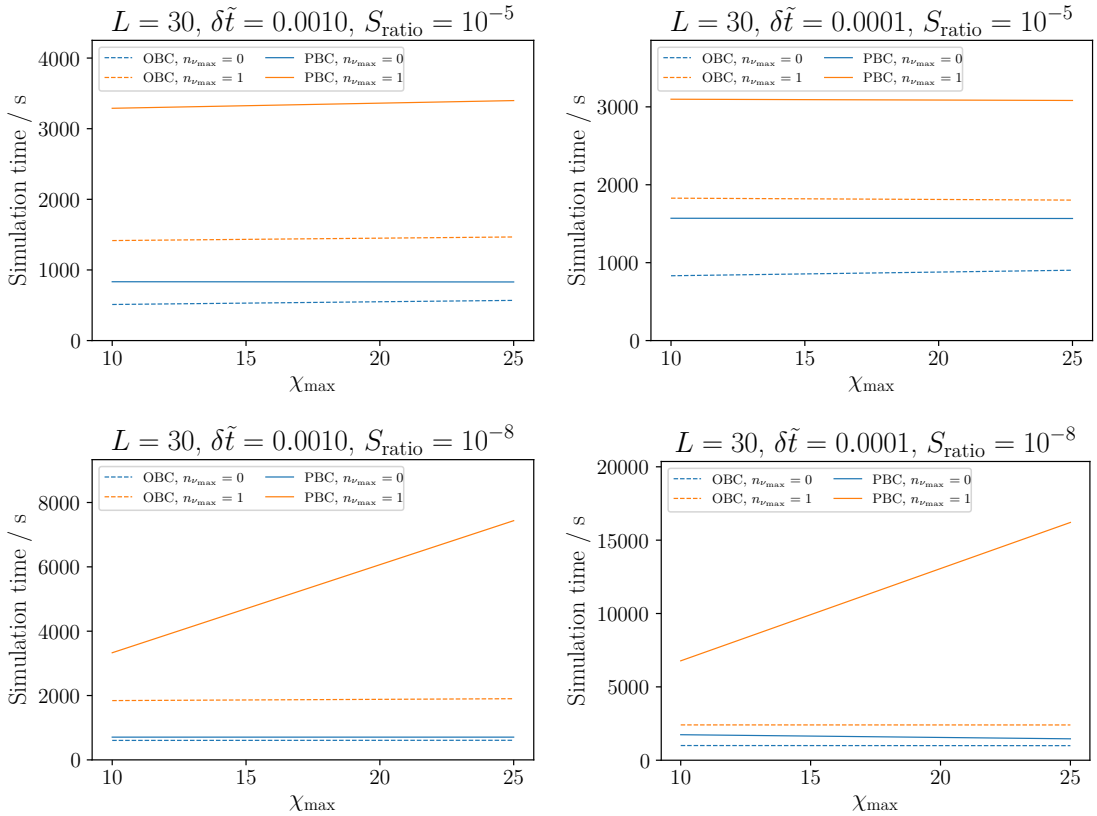


Figure B.7: Effect of $n_{\nu_{\max}}$ and boundary types on total execution time as a function of $\chi_{\max}$, at different truncation levels, defined by S_{ratio}, and time steps, δt.

References

[1] L. Berencei, A. Grout-Smith, J. E. Poole, W. Barford, "Realistic model of charge mobility in π-conjugated polymer systems", *J. Chem. Phys.* **2019**, *151*, 64120.

[2] L. Berencei, W. Barford, S. R. Clark, "Thermally driven polaron transport in conjugated polymers", *Phys. Rev. B* **2022**, *105*, 14303.

[3] S. C. Rasmussen, "The Early History of Polyaniline: Discovery and Origins", *Substantia* **2017**, *1*, 99–109.

[4] W. Barford, *Electronic and Optical Properties of Conjugated Polymers*, 1st ed., Oxford University Press, **2009**.

[5] T. Ito, H. Shirakawa, S. Ikeda, "Simultaneous polymerization and formation of polyacetylene film on the surface of concentrated soluble Ziegler-type catalyst solution", *J. Polym. Sci. Polym. Chem. Ed.* **1974**, *12*, 11–20.

[6] H. Shirakawa, E. J. Louis, A. G. MacDiarmid, C. K. Chiang, A. J. Heeger, "Synthesis of electrically conducting organic polymers: halogen derivatives of polyacetylene, $(CH)_x$", *J. Chem. Soc. Chem. Commun.* **1977**, 578–580.

[7] C. K. Chiang, C. R. Fincher, Y. W. Park, A. J. Heeger, H. Shirakawa, E. J. Louis, S. C. Gau, A. G. MacDiarmid, "Electrical Conductivity in Doped Polyacetylene", *Phys. Rev. Lett.* **1977**, *39*, 1098–1101.

[8] C. K. Chiang, M. A. Druy, S. C. Gau, A. J. Heeger, E. J. Louis, A. G. MacDiarmid, Y. W. Park, H. Shirakawa, "Synthesis of highly conducting films of derivatives of polyacetylene, $(CH)_x$", *J. Am. Chem. Soc.* **1978**, *100*, 1013–1015.

[9] C. K. Chiang, Y. W. Park, A. J. Heeger, H. Shirakawa, E. J. Louis, A. G. MacDiarmid, "Conducting polymers: Halogen doped polyacetylene", *J. Chem. Phys.* **1978**, *69*, 5098–5104.

[10] J. H. Burroughes, D. D. C. Bradley, A. R. Brown, R. N. Marks, K. Mackay, R. H. Friend, P. L. Burns, A. B. Holmes, "Light-emitting diodes based on conjugated polymers", *Nature* **1990**, *347*, 539.

[11] G. Yu, J. Gao, J. C. Hummelen, F. Wudl, A. J. Heeger, "Polymer Photovoltaic Cells: Enhanced Efficiencies via a Network of Internal Donor-Acceptor Heterojunctions", *Science (80-.).* **1995**, *270*, 1789–1791.

[12] A. J. Heeger, "Semiconducting and Metallic Polymers: The Fourth Generation of Polymeric Materials (Nobel Lecture)", *Angew. Chemie Int. Ed.* **2001**, *40*, 2591–2611.

[13] A. G. MacDiarmid, ""Synthetic Metals": A Novel Role for Organic Polymers (Nobel Lecture)", *Angew. Chemie Int. Ed.* **2001**, *40*, 2581–2590.

[14] H. Shirakawa, "The Discovery of Polyacetylene Film: The Dawning of an Era of Conducting Polymers (Nobel Lecture)", *Angew. Chemie Int. Ed.* **2001**, *40*, 2574–2580.

[15] C. W. Tang, S. A. VanSlyke, "Organic electroluminescent diodes", *Appl. Phys. Lett.* **1987**, *51*, 913–915.

[16] J. Kido, M. Kimura, K. Nagai, "Multilayer White Light-Emitting Organic Electroluminescent Device", *Science (80-.).* **1995**, *267*, 1332–1334.

[17] M. Koden, *OLED Displays and Lighting*, John Wiley & Sons, Incorporated, Chicester, United Kingdom, **2016**.

[18] R. Su, S. H. Park, X. Ouyang, S. I. Ahn, M. C. McAlpine, "3D-printed flexible organic light-emitting diode displays", *Sci. Adv.* **2022**, *8*, eabl8798.

[19] C. Sekine, Y. Tsubata, T. Yamada, M. Kitano, S. Doi, "Recent progress of high performance polymer OLED and OPV materials for organic printed electronics", *Sci. Technol. Adv. Mater.* **2014**, *15*, 34203.

[20] S.-J. Zou, Y. Shen, F.-M. Xie, J.-D. Chen, Y.-Q. Li, J.-X. Tang, "Recent advances in organic light-emitting diodes: toward smart lighting and displays", *Mater. Chem. Front.* **2020**, *4*, 788–820.

[21] G. Hong, X. Gan, C. Leonhardt, Z. Zhang, J. Seibert, J. M. Busch, S. Bräse, "A Brief History of OLEDs—Emitter Development and Industry Milestones", *Adv. Mater.* **2021**, *33*, 2005630.

[22] P. R. Berger, M. Kim, "Polymer solar cells: P3HT:PCBM and beyond", *J. Renew. Sustain. Energy* **2018**, *10*, 13508.

[23] H. Kallmann, M. Pope, "Photovoltaic Effect in Organic Crystals", *J. Chem. Phys.* **1959**, *30*, 585–586.

[24] C. W. Tang, "Two-layer organic photovoltaic cell", *Appl. Phys. Lett.* **1986**, *48*, 183–185.

[25] C. Brabec, U. Scherf, V. Dyakonov, *Organic Photovoltaics : Materials, Device Physics, and Manufacturing Technologies*, John Wiley & Sons, Incorporated, Weinheim, Germany, **2014**.

[26] M. Green, E. Dunlop, J. Hohl-Ebinger, M. Yoshita, N. Kopidakis, X. Hao, "Solar cell efficiency tables (version 57)", *Prog. Photovoltaics Res. Appl.* **2021**, *29*, 3–15.

[27] Q. Liu, Y. Jiang, K. Jin, J. Qin, J. Xu, W. Li, J. Xiong, J. Liu, Z. Xiao, K. Sun, S. Yang, X. Zhang, L. Ding, "18% Efficiency organic solar cells", *Sci. Bull.* **2020**, *65*, 272–275.

[28] J.-M. Nunzi, "Organic photovoltaic materials and devices", *Comptes Rendus Phys.* **2002**, *3*, 523–542.

[29] H. Hoppe, N. S. Sariciftci in *Photoresponsive Polym. II*, (Eds.: S. R. Marder, K.-S. Lee), Springer Berlin Heidelberg, Berlin, Heidelberg, **2008**, pp. 1–86.

[30] P. W. Atkins, J. De Paula, *Atkins' Physical Chemistry*, 8th ed, Oxford University Press, Oxford; New York, **2006**.

[31] W. Shockley, H. J. Queisser, "Detailed Balance Limit of Efficiency of p-n Junction Solar Cells", *J. Appl. Phys.* **1961**, *32*, 510–519.

[32] A. Rao, R. H. Friend, "Harnessing singlet exciton fission to break the Shockley–Queisser limit", *Nat. Rev. Mater.* **2017**, *2*, 17063.

[33] J.-L. Brédas, J. E. Norton, J. Cornil, V. Coropceanu, "Molecular Understanding of Organic Solar Cells: The Challenges", *Acc. Chem. Res.* **2009**, *42*, 1691–1699.

[34] A. Nitzan, *Chemical Dynamics in Condensed Phases: Relaxation, Transfer and Reactions in Condensed Molecular Systems*, Oxford University Press, Oxford New York, **2006**.

[35] R. G. Kepler, "Charge Carrier Production and Mobility in Anthracene Crystals", *Phys. Rev.* **1960**, *119*, 1226–1229.

[36] O. H. LeBlanc, "Hole and Electron Drift Mobilities in Anthracene", *J. Chem. Phys.* **1960**, *33*, 626.

[37] V. Coropceanu, J. Cornil, D. A. da Silva Filho, Y. Olivier, R. Silbey, J.-L. Brédas, "Charge Transport in Organic Semiconductors", *Chem. Rev.* **2007**, *107*, 926–952.

[38] P. G. Schouten, J. M. Warman, M. P. Haas, de, "Effect of accumulated radiation dose on pulse radiolysis conductivity transients in a mesomorphic octa-n-alkoxy-substituted phthalocyanine", *J. Phys. Chem.* **1993**, *97*, 9863–9870.

[39] A. Kryukov, A. Saidov, A. V. Vannikov, "Charge carrier transport in poly(phenylene vinylene) films", *Thin Solid Films* **1992**, *209*, 84–91.

[40] F. C. Grozema, L. D. A. Siebbeles, "Charge Mobilities in Conjugated Polymers Measured by Pulse Radiolysis Time-Resolved Microwave Conductivity: From Single Chains to Solids", *J. Phys. Chem. Lett.* **2011**, *2*, 2951–2958.

[41] S. Takagi, A. Toriumi, M. Iwase, H. Tango, "On the universality of inversion layer mobility in Si MOSFET's: Part I-effects of substrate impurity concentration", *IEEE Trans. Electron Devices* **1994**, *41*, 2357–2362.

[42] C. D. Dimitrakopoulos, P. R. L. Malenfant, "Organic Thin Film Transistors for Large Area Electronics", *Adv. Mater.* **2002**, *14*, 99–117.

[43] T. Dürkop, B. M. Kim, M. S. Fuhrer, "Properties and applications of high-mobility semiconducting nanotubes", *J. Phys. Condens. Matter* **2004**, *16*, R553–R580.

[44] M. Abkowitz, M. Stolka, M. Morgan, "Behavior of the drift mobility in the glass transition region of some hole-transporting amorphous organic films", *J. Appl. Phys.* **1981**, *52*, 3453–3457.

[45] L. B. Schein, A. Peled, D. Glatz, "The electric field dependence of the mobility in molecularly doped polymers", *J. Appl. Phys.* **1989**, *66*, 686–692.

[46] P. M. Borsenberger, L. Pautmeier, H. Bässler, "Charge transport in disordered molecular solids", *J. Chem. Phys.* **1991**, *94*, 5447–5454.

[47] M. Gailberger, H. Bässler, "dc and transient photoconductivity of poly(2-phenyl-1,4-phenylenevinylene)", *Phys. Rev. B* **1991**, *44*, 8643–8651.

[48] M. Novo, M. Auweraer, van der, F. C. Schryver, de, P. Borsenberger, H. Bässler, "Anomalous Field Dependence of the Hole Mobility in a Molecular Doped Polymer", *Phys. status solidi* **1993**, *177*, 223–241.

[49] H. Meyer, D. Haarer, H. Naarmann, H. H. Hörhold, "Trap distribution for charge carriers in poly(paraphenylene vinylene) (PPV) and its substituted derivative DPOP-PPV", *Phys. Rev. B* **1995**, *52*, 2587–2598.

[50] K. Pichler, C. P. Jarrett, R. H. Friend, B. Ratier, A. Moliton, "Field-effect transistors based on poly(p-phenylene vinylene) doped by ion implantation", *J. Appl. Phys.* **1995**, *77*, 3523–3527.

[51] P. W. M. Blom, M. J. M. Jong, de, J. J. M. Vleggaar, "Electron and hole transport in poly(p-phenylene vinylene) devices", *Appl. Phys. Lett.* **1996**, *68*, 3308–3310.

[52] E. Lebedev, T. Dittrich, V. Petrova-Koch, S. Karg, W. Brütting, "Charge carrier mobility in poly(p-phenylenevinylene) studied by the time-of-flight technique", *Appl. Phys. Lett.* **1997**, *71*, 2686–2688.

[53] D. Hertel, H. Bässler, U. Scherf, H. H. Hörhold, "Charge carrier transport in conjugated polymers", *J. Chem. Phys.* **1999**, *110*, 9214–9222.

[54] A. J. Mozer, N. S. Sariciftci, "Negative electric field dependence of charge carrier drift mobility in conjugated, semiconducting polymers", *Chem. Phys. Lett.* **2004**, *389*, 438–442.

[55] A. J. Mozer, P. Denk, M. C. Scharber, H. Neugebauer, N. S. Sariciftci, P. Wagner, L. Lutsen, D. Vanderzande, "Novel Regiospecific MDMO-PPV Copolymer with Improved Charge Transport for Bulk Heterojunction Solar Cells", *J. Phys. Chem. B* **2004**, *108*, 5235–5242.

[56] A. J. Mozer, N. S. Sariciftci, A. Pivrikas, R. Österbacka, G. Juška, L. Brassat, H. Bässler, "Charge carrier mobility in regioregular poly(3-hexylthiophene) probed by transient conductivity techniques: A comparative study", *Phys. Rev. B* **2005**, *71*, 35214.

[57] A. R. Tameev, S. V. Novikov, A. V. Vannikov, E. M. Nechvolodova, S. A. Arnautov in 2006 IEEE 4th World Conf. Photovolt. Energy Conf. *Vol. 1*, **2006**, pp. 244–246.

[58] C. A. Amorim, M. R. Cavallari, G. Santos, F. J. Fonseca, A. M. Andrade, S. Mergulhão, "Determination of carrier mobility in MEH-PPV thin-films by stationary and transient current techniques", *J. Non. Cryst. Solids* **2012**, *358*, 484–491.

[59] R. J. O. M. Hoofman, M. P. Haas, de, L. D. A. Siebbeles, J. M. Warman, "Highly mobile electrons and holes on isolated chains of the semiconducting polymer poly(phenylene vinylene)", *Nature* **1998**, *392*, 54.

[60] P. Prins, F. C. Grozema, J. M. Schins, S. Patil, U. Scherf, L. D. A. Siebbeles, "High Intrachain Hole Mobility on Molecular Wires of Ladder-Type Poly(*p*-Phenylenes)", *Phys. Rev. Lett.* **2006**, *96*, 146601.

[61] H. Bässler, G. Schönherr, M. Abkowitz, D. M. Pai, "Hopping transport in prototypical organic glasses", *Phys. Rev. B* **1982**, *26*, 3105–3113.

[62] J. Veres, S. D. Ogier, S. W. Leeming, D. C. Cupertino, S. Mohialdin Khaffaf, "Low-k Insulators as the Choice of Dielectrics in Organic Field-Effect Transistors", *Adv. Funct. Mater.* **2003**, *13*, 199–204.

[63] O. D. Jurchescu, J. Baas, T. T. M. Palstra, "Effect of impurities on the mobility of single crystal pentacene", *Appl. Phys. Lett.* **2004**, *84*, 3061–3063.

[64] V. Podzorov, E. Menard, A. Borissov, V. Kiryukhin, J. A. Rogers, M. E. Gershenson, "Intrinsic Charge Transport on the Surface of Organic Semiconductors", *Phys. Rev. Lett.* **2004**, *93*, 86602.

[65] V. Podzorov, E. Menard, J. A. Rogers, M. E. Gershenson, "Hall Effect in the Accumulation Layers on the Surface of Organic Semiconductors", *Phys. Rev. Lett.* **2005**, *95*, 226601.

[66] O. Ostroverkhova, D. G. Cooke, F. A. Hegmann, J. E. Anthony, V. Podzorov, M. E. Gershenson, O. D. Jurchescu, T. T. M. Palstra, "Ultrafast carrier dynamics in pentacene, functionalized pentacene, tetracene, and rubrene single crystals", *Appl. Phys. Lett.* **2006**, *88*, 162101.

[67] J. Frenkel, "On Pre-Breakdown Phenomena in Insulators and Electronic Semi-Conductors", *Phys. Rev.* **1938**, *54*, 647–648.

[68] D. M. Pai, "Transient Photoconductivity in Poly(N-vinylcarbazole)", *J. Chem. Phys.* **1970**, *52*, 2285–2291.

[69] R. M. Hill, "Poole-Frenkel conduction in amorphous solids", *Philos. Mag. A J. Theor. Exp. Appl. Phys.* **1971**, *23*, 59–86.

[70] W. D. Gill, "Drift mobilities in amorphous charge-transfer complexes of trinitrofluorenone and poly-n-vinylcarbazole", *J. Appl. Phys.* **1972**, *43*, 5033–5040.

[71] H. H. Fong, A. Papadimitratos, G. G. Malliaras, "Nondispersive hole transport in a polyfluorene copolymer with a mobility of 0.01cm2V-1s-1", *Appl. Phys. Lett.* **2006**, *89*, 172116.

[72] G. Verbeek, M. V. Auweraer, der, F. C. D. Schryver, C. Geelen, D. Terrell, S. D. Meuter, "The decrease of the hole mobility in a molecularly doped polymer at high electric fields", *Chem. Phys. Lett.* **1992**, *188*, 85–92.

[73] R. H. Young, N. G. Rule, "Electronic hopping velocities that decrease as the electric field strength increases", *Phys. Rev. Lett.* **1994**, *72*, 388–391.

[74] B. Hartenstein, H. Bässler, S. Heun, P. Borsenberger, M. V. Auweraer, der, F. C. D. Schryver, "Charge transport in molecularly doped polymers at low dopant concentrations: simulation and experiment", *Chem. Phys.* **1995**, *191*, 321–332.

[75] C. Tanase, E. J. Meijer, P. W. M. Blom, D. M. Leeuw, de, "Unification of the Hole Transport in Polymeric Field-Effect Transistors and Light-Emitting Diodes", *Phys. Rev. Lett.* **2003**, *91*, 216601.

[76] C. Tanase, P. W. M. Blom, D. M. Leeuw, de, "Origin of the enhanced space-charge-limited current in poly(*p*-phenylene vinylene)", *Phys. Rev. B* **2004**, *70*, 193202.

[77] W. F. Pasveer, J. Cottaar, C. Tanase, R. Coehoorn, P. A. Bobbert, P. W. M. Blom, D. M. Leeuw, de, M. A. J. Michels, "Unified Description of Charge-Carrier Mobilities in Disordered Semiconducting Polymers", *Phys. Rev. Lett.* **2005**, *94*, 206601.

[78] H. Bässler, "Charge Transport in Disordered Organic Photoconductors a Monte Carlo Simulation Study", *Phys. status solidi* **1993**, *175*, 15–56.

[79] Y. Gartstein, E. M. Conwell, "High-field hopping mobility in molecular systems with spatially correlated energetic disorder", *Chem. Phys. Lett.* **1995**, *245*, 351–358.

[80] D. H. Dunlap, P. E. Parris, V. M. Kenkre, "Charge-Dipole Model for the Universal Field Dependence of Mobilities in Molecularly Doped Polymers", *Phys. Rev. Lett.* **1996**, *77*, 542–545.

[81] S. V. Novikov, D. H. Dunlap, V. M. Kenkre, P. E. Parris, A. V. Vannikov, "Essential Role of Correlations in Governing Charge Transport in Disordered Organic Materials", *Phys. Rev. Lett.* **1998**, *81*, 4472–4475.

[82] M. V. Auweraer, der, F. C. D. Schryver, P. Borsenberger, "The relevance of polaronic effects to the hopping motion of charges", *Chem. Phys.* **1994**, *186*, 409–433.

[83] S. Athanasopoulos, J. Kirkpatrick, D. Martínez, J. M. Frost, C. M. Foden, A. B. Walker, J. Nelson, "Predictive Study of Charge Transport in Disordered Semiconducting Polymers", *Nano Lett.* **2007**, *7*, 1785–1788.

[84] N. Lu, L. Li, W. Banerjee, P. Sun, N. Gao, M. Liu, "Charge carrier hopping transport based on Marcus theory and variable-range hopping theory in organic semiconductors", *J. Appl. Phys.* **2015**, *118*, 45701.

[85] P. E. Parris, V. M. Kenkre, D. H. Dunlap, "Nature of Charge Carriers in Disordered Molecular Solids: Are Polarons Compatible with Observations?", *Phys. Rev. Lett.* **2001**, *87*, 126601.

[86] I. I. Fishchuk, A. Kadashchuk, S. T. Hoffmann, S. Athanasopoulos, J. Genoe, H. Bässler, A. Köhler, "Unified description for hopping transport in organic semiconductors including both energetic disorder and polaronic contributions", *Phys. Rev. B* **2013**, *88*, 125202.

[87] S. D. Baranovskii, "Theoretical description of charge transport in disordered organic semiconductors", *Phys. status solidi* **2014**, *251*, 487–525.

[88] M. Auweraer, der, F. C. De Schryver, P. M. Borsenberger, H. Bässler, "Disorder in Charge Transport in doped polymers", *Adv. Mater.* **1994**, *6*, 199–213.

[89] K. Seki, M. Tachiya, "Electric field dependence of charge mobility in energetically disordered materials: Polaron aspects", *Phys. Rev. B* **2001**, *65*, 14305.

[90] H. Cordes, S. D. Baranovskii, K. Kohary, P. Thomas, S. Yamasaki, F. Hensel, J.-H. Wendorff, "One-dimensional hopping transport in disordered organic solids. I. Analytic calculations", *Phys. Rev. B* **2001**, *63*, 94201.

[91] K. Kohary, H. Cordes, S. D. Baranovskii, P. Thomas, S. Yamasaki, F. Hensel, J.-H. Wendorff, "One-dimensional hopping transport in disordered organic solids. II. Monte Carlo simulations", *Phys. Rev. B* **2001**, *63*, 94202.

[92] R. P. Fornari, A. Troisi, "Theory of charge hopping along a disordered polymer chain", *Phys. Chem. Chem. Phys.* **2014**, *16*, 9997–10007.

[93] L. B. Schein, D. Glatz, J. C. Scott, "Observation of the transition from adiabatic to nonadiabatic small polaron hopping in a molecularly doped polymer", *Phys. Rev. Lett.* **1990**, *65*, 472–475.

[94] L. Pautmeier, J. C. Scott, L. B. Schein, "Activation energies of charge transport in doubly-doped polymers: polarons and disorder", *Chem. Phys. Lett.* **1992**, *197*, 568–572.

[95] R. P. Fornari, P. W. M. Blom, A. Troisi, "How Many Parameters Actually Affect the Mobility of Conjugated Polymers?", *Phys. Rev. Lett.* **2017**, *118*, 86601.

[96] S. S. Skourtis, "Electron transfer through time-dependent bridges: tunneling by virtual transitions that break the Born–Oppenheimer approximation", *Chem. Phys. Lett.* **2003**, *372*, 224–231.

[97] A. Troisi, A. Nitzan, M. A. Ratner, "A rate constant expression for charge transfer through fluctuating bridges", *J. Chem. Phys.* **2003**, *119*, 5782–5788.

[98] M. Jakobsson, S. Stafström, "Polaron effects and electric field dependence of the charge carrier mobility in conjugated polymers", *J. Chem. Phys.* **2011**, *135*, 134902.

[99] M. Jakobsson, M. Linares, S. Stafström, "Monte Carlo simulations of charge transport in organic systems with true off-diagonal disorder", *J. Chem. Phys.* **2012**, *137*, 114901.

[100] L. Gisslén, Å. Johansson, S. Stafström, "Charge and energy dynamics in photo-excited poly(para-phenylenevinylene) systems", *J. Chem. Phys.* **2004**, *121*, 1601–1608.

[101] A. Troisi, G. Orlandi, "Charge-Transport Regime of Crystalline Organic Semiconductors: Diffusion Limited by Thermal Off-Diagonal Electronic Disorder", *Phys. Rev. Lett.* **2006**, *96*, 86601.

[102] N. M. Albu, D. J. Yaron, "Brownian Dynamics Model of Excited-State Relaxation in Solutions of Conjugated Oligomers", *J. Phys. Chem. C* **2013**, *117*, 12299–12306.

[103] O. R. Tozer, W. Barford, "Intrachain exciton dynamics in conjugated polymer chains in solution", *J. Chem. Phys.* **2015**, *143*, 84102.

[104] L. Wang, D. Beljonne, "Flexible Surface Hopping Approach to Model the Crossover from Hopping to Band-like Transport in Organic Crystals", *J. Phys. Chem. Lett.* **2013**, *4*, 1888–1894.

[105] L. Wang, D. Beljonne, "Charge transport in organic semiconductors: Assessment of the mean field theory in the hopping regime", *J. Chem. Phys.* **2013**, *139*, 64316.

[106] L. Wang, O. V. Prezhdo, D. Beljonne, "Mixed quantum-classical dynamics for charge transport in organics", *Phys. Chem. Chem. Phys.* **2015**, *17*, 12395–12406.

[107] J. E. Poole, D. A. Damry, O. R. Tozer, W. Barford, "Charge mobility induced by Brownian fluctuations in π-conjugated polymers in solution", *Phys. Chem. Chem. Phys.* **2016**, *18*, 2574–2579.

[108] J. R. Mannouch, W. Barford, S. Al-Assam, "Ultra-fast relaxation, decoherence, and localization of photoexcited states in π-conjugated polymers", *J. Chem. Phys.* **2018**, *148*, 34901.

[109] W. Barford, J. R. Mannouch, "Torsionally induced exciton localization and decoherence in π-conjugated polymers", *J. Chem. Phys.* **2018**, *149*, 214107.

[110] R. Binder, D. Lauvergnat, I. Burghardt, "Conformational Dynamics Guides Coherent Exciton Migration in Conjugated Polymer Materials: First-Principles Quantum Dynamical Study", *Phys. Rev. Lett.* **2018**, *120*, 227401.

[111] S. Giannini, A. Carof, M. Ellis, H. Yang, O. G. Ziogos, S. Ghosh, J. Blumberger, "Quantum localization and delocalization of charge carriers in organic semiconducting crystals", *Nat. Commun.* **2019**, *10*, 3843.

[112] R. Hegger, R. Binder, I. Burghardt, "First-Principles Quantum and Quantum-Classical Simulations of Exciton Diffusion in Semiconducting Polymer Chains at Finite Temperature", *J. Chem. Theory Comput.* **2020**, *16*, 5441–5455.

[113] R. Binder, I. Burghardt, "First-principles description of intra-chain exciton migration in an oligo(para-phenylene vinylene) chain. II. ML-MCTDH simulations of exciton dynamics at a torsional defect", *J. Chem. Phys.* **2020**, *152*, 204120.

[114] R. Binder, M. Bonfanti, D. Lauvergnat, I. Burghardt, "First-principles description of intra-chain exciton migration in an oligo(para-phenylene vinylene) chain. I. Generalized Frenkel–Holstein Hamiltonian", *J. Chem. Phys.* **2020**, *152*, 204119.

[115] R. Binder, I. Burghardt, "First-principles quantum simulations of exciton diffusion on a minimal oligothiophene chain at finite temperature", *Faraday Discuss.* **2020**, *221*, 406–427.

[116] F. Di Maiolo, D. Brey, R. Binder, I. Burghardt, "Quantum dynamical simulations of intra-chain exciton diffusion in an oligo (para-phenylene vinylene) chain at finite temperature", *J. Chem. Phys.* **2020**, *153*, 184107.

[117] A. Troisi, "Charge transport in high mobility molecular semiconductors: classical models and new theories", *Chem. Soc. Rev.* **2011**, *40*, 2347–2358.

[118] H. Oberhofer, K. Reuter, J. Blumberger, "Charge Transport in Molecular Materials: An Assessment of Computational Methods", *Chem. Rev.* **2017**, *117*, 10319–10357.

[119] T. Nematiaram, A. Troisi, "Modeling charge transport in high-mobility molecular semiconductors: Balancing electronic structure and quantum dynamics methods with the help of experiments", *J. Chem. Phys.* **2020**, *152*, 190902.

[120] S. Fratini, M. Nikolka, A. Salleo, G. Schweicher, H. Sirringhaus, "Charge transport in high-mobility conjugated polymers and molecular semiconductors", *Nat. Mater.* **2020**, *19*, 491–502.

[121] O. R. Tozer, W. Barford, "Localization of large polarons in the disordered Holstein model", *Phys. Rev. B* **2014**, *89*, 155434.

[122] W. Barford, M. Marcus, O. R. Tozer, "Polarons in π-Conjugated Polymers: Anderson or Landau?", *J. Phys. Chem. A* **2016**, *120*, 615–620.

[123] S. Fratini, S. Ciuchi, "Bandlike Motion and Mobility Saturation in Organic Molecular Semiconductors", *Phys. Rev. Lett.* **2009**, *103*, 266601.

[124] S. Ciuchi, S. Fratini, D. Mayou, "Transient localization in crystalline organic semiconductors", *Phys. Rev. B* **2011**, *83*, 81202.

[125] S. Fratini, D. Mayou, S. Ciuchi, "The Transient Localization Scenario for Charge Transport in Crystalline Organic Materials", *Adv. Funct. Mater.* **2016**, *26*, 2292–2315.

[126] K. Sakai, Y. Okada, T. Uemura, J. Tsurumi, R. Häusermann, H. Matsui, T. Fukami, H. Ishii, N. Kobayashi, K. Hirose, J. Takeya, "The emergence of charge coherence in soft molecular organic semiconductors via the suppression of thermal fluctuations", *NPG Asia Mater.* **2016**, *8*, e252–e252.

[127] Z. Q. Li, V. Podzorov, N. Sai, M. C. Martin, M. E. Gershenson, M. Di Ventra, D. N. Basov, "Light Quasiparticles Dominate Electronic Transport in Molecular Crystal Field-Effect Transistors", *Phys. Rev. Lett.* **2007**, *99*, 16403.

[128] W. Barford, *Electronic and Optical Properties of Conjugated Polymers*, 2nd ed., Oxford University Press, **2013**.

[129] T. Holstein, "Studies of polaron motion: Part I. The molecular-crystal model", *Ann. Phys. (N. Y).* **1959**, *8*, 325–342.

[130] T. Holstein, "Studies of polaron motion: Part II. The "small" polaron", *Ann. Phys. (N. Y).* **1959**, *8*, 343–389.

[131] W. Barford, M. Marcus, "Theory of optical transitions in conjugated polymers. I. Ideal systems", *J. Chem. Phys.* **2014**, *141*, 164101.

[132] M. Y. Lavrentiev, W. Barford, "Electron-phonon interactions in poly(para-phenylene) oligomers", *J. Chem. Phys.* **1999**, *111*, 11177–11182.

[133] M. Born, R. Oppenheimer, "Zur Quantentheorie der Molekeln", *Ann. Phys.* **1927**, *389*, 457–484.

[134] A. Onipko, Y. Klymenko, L. Malysheva, "Effect of length and geometry on the highest occupied molecular orbital-lowest unoccupied molecular orbital gap of conjugated oligomers: An analytical Hückel model approach", *J. Chem. Phys.* **1997**, *107*, 7331–7344.

[135] E. E. Moore, W. Barford, R. J. Bursill, "Relaxation energies and excited-state structures of poly(paraphenylene)", *Phys. Rev. B* **2005**, *71*, 115107.

[136] P. W. Anderson, "Absence of Diffusion in Certain Random Lattices", *Phys. Rev.* **1958**, *109*, 1492–1505.

[137] N. F. Mott, W. D. Twose, "The theory of impurity conduction", *Adv. Phys.* **1961**, *10*, 107–163.

[138] A. V. Malyshev, V. A. Malyshev, "Statistics of low energy levels of a one-dimensional weakly localized Frenkel exciton: A numerical study", *Phys. Rev. B* **2001**, *63*, 195111.

[139] D. V. Makhov, W. Barford, "Local exciton ground states in disordered polymers", *Phys. Rev. B* **2010**, *81*, 165201.

[140] R. E. Borland, J. A. Pople, "The nature of the electronic states in disordered one-dimensional systems", *Proc. R. Soc. London. Ser. A. Math. Phys. Sci.* **1963**, *274*, 529–545.

[141] J. L. Cardy, "Electron localisation in disordered systems and classical solutions in Ginzburg-Landau field theory", *J. Phys. C Solid State Phys.* **1978**, *11*, L321.

[142] E. W. Knapp, "Lineshapes of molecular aggregates, exchange narrowing and intersite correlation", *Chem. Phys.* **1984**, *85*, 73–82.

[143] W. Barford, D. Trembath, "Exciton localization in polymers with static disorder", *Phys. Rev. B* **2009**, *80*, 165418.

[144] T. Qin, A. Troisi, "Relation between Structure and Electronic Properties of Amorphous MEH-PPV Polymers", *J. Am. Chem. Soc.* **2013**, *135*, 11247–11256.

[145] L. D. Landau, "A Theory of Energy Transfer on Collisions", *Phys. Z. Sowjet.* **1932**, *1*, 88.

[146] L. D. Landau, "A Theory of Energy Transfer on Collisions II", *Phys. Z. Sowjet.* **1932**, *2*, 46.

[147] C. Zener, R. H. Fowler, "Non-adiabatic crossing of energy levels", *Proc. R. Soc. London. Ser. A Contain. Pap. a Math. Phys. Character* **1932**, *137*, 696–702.

[148] C. Zener, R. H. Fowler, "Dissociation of excited diatomic molecules by external perturbations", *Proc. R. Soc. London. Ser. A Contain. Pap. a Math. Phys. Character* **1933**, *140*, 660–668.

[149] E. C. G. Stueckelberg, "Theorie der unelastischen Stösse zwischen Atomen", *Helv. Phys. Acta* **1932**, *5*, 369–422.

[150] R. A. Marcus, "On the Theory of Oxidation-Reduction Reactions Involving Electron Transfer. I", *J. Chem. Phys.* **1956**, *24*, 966–978.

[151] R. A. Marcus, "Chemical and Electrochemical Electron-Transfer Theory", *Annu. Rev. Phys. Chem.* **1964**, *15*, 155–196.

[152] J. Franck, E. G. Dymond, "Elementary processes of photochemical reactions", *Trans. Faraday Soc.* **1926**, *21*, 536–542.

[153] E. Condon, "A Theory of Intensity Distribution in Band Systems", *Phys. Rev.* **1926**, *28*, 1182–1201.

[154] J. R. Miller, L. T. Calcaterra, G. L. Closs, "Intramolecular long-distance electron transfer in radical anions. The effects of free energy and solvent on the reaction rates", *J. Am. Chem. Soc.* **1984**, *106*, 3047–3049.

[155] N. S. Hush, M. N. Paddon-Row, E. Cotsaris, H. Oevering, J. W. Verhoeven, M. Heppener, "Distance dependence of photoinduced electron transfer through non-conjugated bridges", *Chem. Phys. Lett.* **1985**, *117*, 8–11.

[156] I. R. Gould, D. Ege, S. L. Mattes, S. Farid, "Return electron transfer within geminate radical ion pairs. Observation of the Marcus inverted region", *J. Am. Chem. Soc.* **1987**, *109*, 3794–3796.

[157] G. L. Closs, J. R. Miller, "Intramolecular Long-Distance Electron Transfer in Organic Molecules", *Science (80-.).* **1988**, *240*, 440–447.

[158] R. A. Marcus, N. Sutin, "Electron transfers in chemistry and biology", *Biochim. Biophys. Acta - Rev. Bioenerg.* **1985**, *811*, 265–322.

[159] J. E. Lawrence, D. E. Manolopoulos, "Analytic continuation of Wolynes theory into the Marcus inverted regime", *J. Chem. Phys.* **2018**, *148*, 102313.

[160] A. D. McLachlan, "A variational solution of the time-dependent Schrodinger equation", *Mol. Phys.* **1964**, *8*, 39–44.

[161] D. A. Micha, "A self-consistent eikonal treatment of electronic transitions in molecular collisions", *J. Chem. Phys.* **1983**, *78*, 7138–7145.

[162] Z. Kirson, R. B. Gerber, A. Nitzan, M. A. Ratner, "Dynamics of metal electron excitation in atom-surface collisions: A quantum wave packet approach", *Surf. Sci.* **1984**, *137*, 527–550.

[163] S.-I. Sawada, A. Nitzan, H. Metiu, "Mean-trajectory approximation for charge- and energy-transfer processes at surfaces", *Phys. Rev. B* **1985**, *32*, 851–867.

[164] O. V. Prezhdo, P. J. Rossky, "Mean-field molecular dynamics with surface hopping", *J. Chem. Phys.* **1997**, *107*, 825–834.

[165] P. Ehrenfest, "Bemerkung über die angenäherte Gültigkeit der klassischen Mechanik innerhalb der Quantenmechanik", *Zeitschrift für Phys.* **1927**, *45*, 455–457.

[166] A. P. Horsfield, D. R. Bowler, H. Ness, C. G. Sánchez, T. N. Todorov, A. J. Fisher, "The transfer of energy between electrons and ions in solids", *Reports Prog. Phys.* **2006**, *69*, 1195–1234.

[167] P. V. Parandekar, J. C. Tully, "Detailed Balance in Ehrenfest Mixed Quantum-Classical Dynamics", *J. Chem. Theory Comput.* **2006**, *2*, 229–235.

[168] J. C. Tully, "Perspective: Nonadiabatic dynamics theory", *J. Chem. Phys.* **2012**, *137*, 22A301.

[169] A. P. Horsfield, D. R. Bowler, A. J. Fisher, T. N. Todorov, M. J. Montgomery, "Power dissipation in nanoscale conductors: classical, semi-classical and quantum dynamics", *J. Phys. Condens. Matter* **2004**, *16*, 3609–3622.

[170] P. V. Parandekar, J. C. Tully, "Mixed quantum-classical equilibrium", *J. Chem. Phys.* **2005**, *122*, 94102.

[171] J. C. Tully in *Mod. Methods Multidimens. Dyn. Comput. Chem.* World Scientific, **1998**, pp. 34–72.

[172] S. Block, H. W. Streitwolf, "Nucleation of optically excited solitons and breathers intrans-polyacetylene", *J. Phys. Condens. Matter* **1996**, *8*, 889–900.

[173] Z. An, C. Q. Wu, X. Sun, "Dynamics of Photogenerated Polarons in Conjugated Polymers", *Phys. Rev. Lett.* **2004**, *93*, 216407.

[174] A. A. Johansson, S. Stafström, "Nonadiabatic simulations of polaron dynamics", *Phys. Rev. B* **2004**, *69*, 235205.

[175] P. Langevin, "Sur la théorie du mouvement brownien", *Comptes Rendus l'Academie des Sci.* **1908**, *146*, 530–533.

[176] D. S. Lemons, A. Gythiel, "Paul Langevin's 1908 paper "On the Theory of Brownian Motion" ["Sur la théorie du mouvement brownien," C. R. Acad. Sci. (Paris) 146, 530–533 (1908)]", *Am. J. Phys.* **1997**, *65*, 1079–1081.

[177] H. B. Callen, T. A. Welton, "Irreversibility and Generalized Noise", *Phys. Rev.* **1951**, *83*, 34–40.

[178] R. Zwanzig, *Nonequilibrium statistical mechanics*, Oxford University Press, Oxford; New York, **2001**.

[179] G. Vidal, "Efficient Classical Simulation of Slightly Entangled Quantum Computations", *Phys. Rev. Lett.* **2003**, *91*, 147902.

[180] G. Vidal, "Efficient Simulation of One-Dimensional Quantum Many-Body Systems", *Phys. Rev. Lett.* **2004**, *93*, 40502.

[181] S. Al-Assam, S. R. Clark, D. Jaksch, T. D. Team, Tensor Network Theory Library, **2016**.

[182] S. Al-Assam, S. R. Clark, D. Jaksch, "The tensor network theory library", *J. Stat. Mech. Theory Exp.* **2017**, *2017*, 93102.

[183] N. Grønbech-Jensen, O. Farago, "A simple and effective Verlet-type algorithm for simulating Langevin dynamics", *Mol. Phys.* **2013**, *111*, 983–991.

[184] W. M. Young, E. W. Elcock, "Monte Carlo studies of vacancy migration in binary ordered alloys: I", *Proc. Phys. Soc.* **1966**, *89*, 735–746.

[185] M. Silver, K. S. Dy, I. L. Huang, "Monte Carlo Calculation of the Transient Photocurrent in Low-Carrier-Mobility Materials", *Phys. Rev. Lett.* **1971**, *27*, 21–23.

[186] M. Silver, L. Cohen, "Monte Carlo simulation of anomalous transit-time dispersion of amorphous solids", *Phys. Rev. B* **1977**, *15*, 3276–3278.

[187] G. Schönherr, H. Bässler, M. Silver, "Dispersive hopping transport via sites having a Gaussian distribution of energies", *Philos. Mag. B* **1981**, *44*, 47–61.

[188] A. P. J. Jansen, *An Introduction to Kinetic Monte Carlo Simulations of Surface Reactions*, Springer Berlin Heidelberg, **2012**.

[189] U. Schollwöck, "The density-matrix renormalization group in the age of matrix product states", *Ann. Phys. (N. Y).* **2011**, *326*, 96–192.

[190] U. Schollwöck in *Strongly Correl. Syst. Numer. Methods*, (Eds.: A. Avella, F. Mancini), Springer Berlin Heidelberg, Berlin, Heidelberg, **2013**, pp. 67–98.

[191] C. H. Bennett, H. J. Bernstein, S. Popescu, B. Schumacher, "Concentrating partial entanglement by local operations", *Phys. Rev. A* **1996**, *53*, 2046–2052.

[192] J. C. Bridgeman, C. T. Chubb, "Hand-waving and interpretive dance: an introductory course on tensor networks", *J. Phys. A Math. Theor.* **2017**, *50*, 223001.

[193] H. F. Trotter, "On the product of semi-groups of operators", *Proc. Am. Math. Soc.* **1959**, *10*, 545.

[194] M. Suzuki, "Generalized Trotter's formula and systematic approximants of exponential operators and inner derivations with applications to many-body problems", *Commun. Math. Phys.* **1976**, *51*, 183–190.

[195] H. De Raedt, B. De Raedt, "Applications of the generalized Trotter formula", *Phys. Rev. A* **1983**, *28*, 3575–3580.

[196] E. M. Stoudenmire, S. R. White, "Minimally entangled typical thermal state algorithms", *New J. Phys.* **2010**, *12*, 55026.

[197] A. V. Malyshev, V. A. Malyshev, F. Domínguez-Adame, "On the Low-Temperature Diffusion of Localized Frenkel Excitons in Linear Molecular Aggregates", *J. Phys. Chem. B* **2003**, *107*, 4418–4425.

[198] A. V. Malyshev, V. A. Malyshev, F. Domínguez-Adame, "Low-temperature quenching of one-dimensional localized Frenkel excitons", *Chem. Phys. Lett.* **2003**, *371*, 417–425.

[199] V. May, O. Kühn, *Charge and Energy Transfer Dynamics in Molecular Systems*, Wiley-VCH, **2011**.

[200] M. Marcus, O. R. Tozer, W. Barford, "Theory of optical transitions in conjugated polymers. II. Real systems", *J. Chem. Phys.* **2014**, *141*, 164102.

[201] R. S. Mulliken, C. A. Rieke, D. Orloff, H. Orloff, "Formulas and Numerical Tables for Overlap Integrals", *J. Chem. Phys.* **1949**, *17*, 1248–1267.

[202] M. Hultell, S. Stafström, "Impact of ring torsion on the intrachain mobility in conjugated polymers", *Phys. Rev. B* **2007**, *75*, 104304.

[203] P. Costa, da, R. G. Dandrea, E. M. Conwell, "First-principles calculation of the three-dimensional band structure of poly(phenylene vinylene)", *Phys. Rev. B* **1993**, *47*, 1800–1810.

[204] D. R. Gagnon, J. D. Capistran, F. E. Karasz, R. W. Lenz, "Conductivity anisotropy in oriented poly(p-Phenylene vinylene)", *Polym. Bull.* **1984**, *12*, 293–298.

[205] T. Granier, E. L. Thomas, D. R. Gagnon, F. E. Karasz, R. W. Lenz, "Structure investigation of poly(p-phenylene vinylene)", *J. Polym. Sci. Part B Polym. Phys.* **1986**, *24*, 2793–2804.

[206] C. De Leener, E. Hennebicq, J.-C. Sancho-Garcia, D. Beljonne, "Modeling the Dynamics of Chromophores in Conjugated Polymers: The Case of Poly(2-methoxy-5-(2'-ethylhexyl)oxy 1,4-phenylene vinylene) (MEH-PPV)", *J. Phys. Chem. B* **2009**, *113*, 1311–1322.

[207] H. C. F. Martens, P. W. M. Blom, H. F. M. Schoo, "Comparative study of hole transport in poly(p-phenylene vinylene) derivatives", *Phys. Rev. B* **2000**, *61*, 7489–7493.

[208] S. M. Gali, G. D'Avino, P. Aurel, G. Han, Y. Yi, T. A. Papadopoulos, V. Coropceanu, J.-L. Brédas, G. Hadziioannou, C. Zannoni, L. Muccioli, "Energetic fluctuations in amorphous semiconducting polymers: Impact on charge-carrier mobility", *J. Chem. Phys.* **2017**, *147*, 134904.

[209] E. I. Rashba, M. D. Sturge, *Excitons*, North-Holland Pub. Co. Sole distributors for the USA and Canada, Elsevier Science Pub. Co, Amsterdam New York New York, N.Y, **1982**.

[210] J. Mannouch, "Exciton dynamics in π-conjugated polymer systems", PhD thesis, University of Oxford, **2019**.

[211] T. R. Nelson, A. J. White, J. A. Bjorgaard, A. E. Sifain, Y. Zhang, B. Nebgen, S. Fernandez-Alberti, D. Mozyrsky, A. E. Roitberg, S. Tretiak, "Non-adiabatic Excited-State Molecular Dynamics: Theory and Applications for Modeling Photophysics in Extended Molecular Materials", *Chem. Rev.* **2020**, *120*, 2215–2287.

[212] A. V. Malyshev, V. A. Malyshev, "Level and wave function statistics of a localized 1D Frenkel exciton at the bottom of the band", *J. Lumin.* **2001**, *94-95*, 369–372.

[213] W. P. Su, J. R. Schrieffer, A. J. Heeger, "Solitons in Polyacetylene", *Phys. Rev. Lett.* **1979**, *42*, 1698–1701.

[214] K. H. DuBay, M. L. Hall, T. F. Hughes, C. Wu, D. R. Reichman, R. A. Friesner, "Accurate Force Field Development for Modeling Conjugated Polymers", *J. Chem. Theory Comput.* **2012**, *8*, 4556–4569.

[215] S. E. Root, N. E. Jackson, S. Savagatrup, G. Arya, D. J. Lipomi, "Modelling the morphology and thermomechanical behaviour of low-bandgap conjugated polymers and bulk heterojunction films", *Energy Environ. Sci.* **2017**, *10*, 558–569.

[216] A. W. Prentice, J. Wildman, I. Galbraith, M. J. Paterson, "Properties of Conjugated Materials from Quantum Chemistry Coupled to Molecular Dynamics Generated Ensembles", *J. Phys. Chem. A* **2020**, *124*, 10667–10677.